Universidade Federal do Espírito Santo

Programa de Pós-Graduação em Astrofísica, Cosmologia e Gravitação

The Redshift Drift as a new cosmological probe

Pedro Bessa

Thesis submitted as part of the requirements for the degree of
Doctor of Philosophy in Astronomy & Physics

Supervisor: Prof. Valerio Marra
PPGCosmo, Universidade Federal do Espírito Santo (Brazil)

Co-supervisor: Prof. Ruth Durrer
Centre de Physique Théorique, Université de Genève (CH)

2024

Universidade Federal do Espírito Santo
Centro de Ciências Exatas
Programa de Pós-Graduação em Astrofísica, Cosmologia e Gravitação

The Redshift Drift as a new cosmological probe

Pedro Bessa

A presente tese "*The Redshift Drift as a new cosmological probe*" foi submetida no ano de 2024 ao PPGCosmo por *Pedro Bessa* como parte dos requisitos para a obtenção do título de Doutor em Astronomia e Física.

Caso esta tese venha a ser aprovada, esta folha deverá ser substituída pela correspondente de aprovação.

Ficha catalográfica disponibilizada pelo Sistema Integrado de Bibliotecas - SIBI/UFES e elaborada pelo autor

---

Dutra, Pedro Henrique, 1996-
D978t The Redshift Drift as a new cosmological probe / Pedro Henrique Dutra. - 2024.
108 p. : il.

Orientador: Valerio Marra.
Coorientadora: Ruth Durrer.
Tese (Doutorado em Astrofísica, Cosmologia e Gravitação) - Universidade Federal do Espírito Santo, Centro de Ciências Exatas.

1. Cosmologia. 2. Redshift Drift. 3. Large Scale Structure. 4. Perturbation Theory. I. Marra, Valerio. II. Durrer, Ruth. III. Universidade Federal do Espírito Santo. Centro de Ciências Exatas. IV. Título.

CDU: 52

Universidade Federal do Espírito Santo
Centro de Ciências Exatas
PPGCosmo

The Redshift Drift as a new cosmological probe

por

Pedro Henrique Bessa Rodrigues Dutra

Tese submetida ao Programa de Pós-Graduação em Astrofísica, Cosmologia e Gravitação, da Universidade Federal do Espírito Santo, remotamente, como requisito parcial para a obtenção do título de Doutor em Astronomia e Física.

Aprovada por:

Prof. Dr. Valerio Marra (orientador, presidente da banca, UFES) gov.br Documento assinado digitalmente VALERIO MARRA Data: 19/09/2024 16:03:13-0300 Verifique em https://validar.iti.gov.br

Prof. Dr. Ruth Durrer (co-orientadora, Genebra U, Suíça)

Prof. Dr. Rodrigo Von Marttens (membro interno, UFES) gov.br Documento assinado digitalmente RODRIGO FERNANDO LUGON CORNEJO VON M/ Data: 19/09/2024 15:59:28-0300 Verifique em https://validar.iti.gov.br

Prof. Dr. Oliver Piattella (membro interno, Insubria U, Itália) gov.br Documento assinado digitalmente OLIVER FABIO PIATTELLA Data: 19/09/2024 14:11:27-0300 Verifique em https://validar.iti.gov.br

Prof. Dr. Sofie-Marie Koksbang (membro externo, Southern Denmark U, Dinamarca)

Prof. Dr. Carlos Martins (membro externo, Porto U, Portugal)

Vitória-ES, 19 de setembro de 2024.

Esta tese é dedicada a Maria Fernanda Bessa Rodrigues e Jade Michelle Mason.

Abstract

With the advent of precision cosmology and the next generation of telescopes and surveys, observations will allow the standard cosmological model to be tested in old and new regimes with unprecedented accuracy, and the data will demand accurate theoretical models of cosmological phenomena in order to be properly interpreted and processed. Theorists are reassessing old and new probes that allow the current cosmological paradigm to be tested to its limits. One promising new probe, the measurement which is one of the main objectives of the ELT ANDES spectrograph, is the cosmic redshift drift.

One of the theoretical predictions of cosmological models based on Robertson-Walker metrics is the cosmic redshift drift, which measures the real-time rate of change of the spectra of far away sources, and is a generic consequence of cosmological models where the expansion rate is non-constant. Its observation provides a model independent way to measure the time variation of the Universe's expansion and as such, an independent test of the late-time acceleration phase of the Universe and the existence of a cosmological constant.

In this thesis we study the redshift drift in realistic cosmological models containing inhomogeneities in the ΛCDM paradigm. We derive for the first time a gauge-invariant expression for the redshift drift and its power spectrum, and implement the redshift drift fluctuation power spectrum numerically through Einstein-Boltzmann codes and using n-body simulations, providing a solid theoretical foundation for future measurements and observations of the redshift drift in ΛCDM cosmology and beyond.

Resumo

Com o advento da cosmologia de precisão e da próxima geração de telescópios e levantamentos, observações permitirão que o modelo cosmológico padrão seja testado em novos e antigos regimes com uma precisão sem precedentes, e os dados exigirão modelos teóricos precisos de fenômenos cosmológicos para serem devidamente interpretados e processados. Físicos teóricos estão reavaliando sondas antigas e novas que permitem testar o paradigma cosmológico atual até seus limites. Um novo observável promissor, cuja detecção é um dos principais objetivos do espectrógrafo ANDES do Extremely Large Telescope, é a variação do desvio cósmico para o vermelho.
Uma das previsões teóricas de modelos cosmológicos baseados em métricas de Robertson-Walker é a variação do desvio cósmico para o vermelho, que mede a taxa de variação em tempo real dos espectros de fontes distantes e é uma consequência genérica de modelos cosmológicos onde a taxa de expansão não é constante. Sua observação fornece uma maneira independente de modelos de medir a variação temporal da expansão do Universo e, como tal, um teste independente da fase de aceleração tardia do Universo e da existência de uma constante cosmológica.
Nesta tese, estudamos o desvio para o vermelho em modelos cosmológicos realistas que contêm inhomogeneidades dentro do paradigma ΛCDM. Derivamos, pela primeira vez, uma expressão invariante de calibre para a variação do desvio para o vermelho e seu espectro de potência e implementamos numericamente o espectro de potência das flutuações da variação do desvio para o vermelho por meio de códigos Einstein-Boltzmann e usando simulações de n-corpos, fornecendo uma base teórica sólida para futuras medições e observações do desvio para o vermelho na cosmologia ΛCDM e além.

Acknowledgments / Agradecimentos

Tive a sorte na vida de sempre ter as melhores pessoas possíveis perto de mim, mesmo achando que não mereço tanto o amor que recebo. Não me faltaram em quantidade também, então peço perdão pelas inevitáveis omissões, que não indicam falta de gratidão. Nesses quatro duros anos de doutorado aqui sintetizados, lhes deixo meu carinho não extensivo:

Minha avó, pedra fundamental da minha vida em todos os seus aspectos, sem a qual não teria nem começado esta jornada.

Minha mãe, que em sua breve vida não hesitou em me amar incondicionalmente.

Às mulheres que me criaram desde um menino até um homem e que hoje podem contar comigo para tudo: Daniela, Julia e Marise.

Minha família: meus tios-avós, tios, avô e família que não é de sangue por puro acaso do destino: Helena e Helô.

Meu orientador Valerio Marra, que me acolheu e topou seguir essa jornada do doutorado num momento difícil, e virou um grande parceiro de trabalho e mentor.

Meus professores e mentores durante a vida acadêmica, que serviram de exemplo não apenas de excelentes cientistas, mas também de excelentes pessoas: professora Marcela, maestro Armando, professor Julio, e professor Oliver em especial, pelas discussões sobre TQC e lenteamento gravitacional que influenciaram fortemente meus interesses de pesquisa.

Meus grandes e eternos amigos, que me acompanham desde quando nem sabia que queria ser cientista: João, Jorge e Higor. Os grandes e eternos amigos e afetos que conheci depois do começo da minha jornada acadêmica e fizeram do Rio de Janeiro minha casa: Felipe, Luca, Arthur, Anselmo, Ananda, Leo, Fidelis, Karol, Daniel, Julio, Ana, Amanda, Max; e os que estão pelo resto do mundo: Karla, . Os amigos a quem sou eternamente grato por fazer de Vitória uma segunda casa e o doutorado um imenso prazer: Alex, Thalita, Tulio, Jeferson, Izadora, Renan, Ana Paula, Amanda e todo o pessoal incrível do PPGCosmo. Thais, Dinorah, Vitinho, Yanna, Grasi e sua querida esposa Patricia, Mari, Demétrio, Caio, Will e todos que fazem dessa loucura que é a vida acadêmica um prazer imenso.

Minha querida namorada Luciana, que nesse curto tempo se tornou fundamental para minha vida, e foi um raio de Sol nesse ano nebuloso de 2024.

Aos trabalhadores e funcionários de todos os estabelecimentos onde trabalhei, da limpeza, administração, copa e terceirizados. Seu trabalho é fundamental para o progresso científico e seus frutos lhes pertencem tanto quanto a nós cientistas.

E minha gata Utena, cuja natureza Buda também muito me ensina sobre o Universo e suas sutilezas.

Now I'd like to thank everyone that became an important part of my life after I spent almost a year in Geneva, and helped me feel that Switzerland was also home:

To Ruth Durrer, my amazing co-supervisor, which never failed to amaze me with both her knowledge and humanity, and helped me immensely during my stay in Geneva. I'll be eternally grateful for all the lessons you taught me.

To Dennis Stock, my amazing colleague and collaborator. Your passion for Relativity always amazed me, and our passion for Bach transcended continents.

To Jade, which I'll love forever. The short time we spent together was enough for a thousand lifetimes.

To all my friends in the Theoretical Physics department at UniGe which showed me the warmness of the Alps: Angelo, Salma, Marco, Niccolò, Ahmad, Martin, Viraj, Sveva, Zaki and everyone in the amazing cosmology group.

And to everyone that I've met in Europe and will always live in my heart: Rachael, Valeria, Helena, Tais, Elliott, Clara, Luisa, Thanakarn and Andrea.

Agradeço por fim às agências FAPES e CAPES pelas bolsas de financiamento concedidas pelos editais FAPES Nº 13/2019 - PROCAP 2020 e PDSE - Edital nº 10/2022, assim como ao centro computacional CINECA e o uso do supercomputador Santos Dumont do LNCC.

Contents

Introduction

Cosmology is serious business and in our hearts we are nothing if not cosmologists, hanging in a cold cage sifting the ruthless jewels of existence.
— Dennis Overbye

Cosmology was once described as a search for two numbers [1]: the Universe's expansion rate at present time H_0 and its deceleration rate at present time q_0. When Sandage made this claim, the value of Hubble's constant H_0 was yet to be accurately measured, and the quest for an accurate measurement was one he pursued for most of his life. 50 years later, cosmology as a science is described by more than 2 numbers and the ΛCDM paradigm provides a consistent if incomplete history of the cosmos from photon decoupling to today and at scales ranging from the observable Universe to galaxy clusters. Measuring its six parameters with growing accuracy is one of the main scientific endeavours of the 21st century and has led to paradigm changes from particle to astrophysics.

The search for accurate measurements of the cosmological parameters brought Cosmology to its so called precision era, where scientists have access to huge amounts of data from different observations and are able to measure the parameters of the standard ΛCDM without the need to rely on a single method or observable. The current challenge, then, is not only to make sense of this huge amount of data in a precise way, where measurements converge, but to discover new observable quantities that will test the standard model to its limits, allowing us to verify its most basic assumptions. With current and next-generation observations, purely theoretical assumptions in the time of Sandage will not only be tested but measured: the cosmological principle , the time variation of physical constants, the nonlinear formation of cosmic structures and General Relativity itself will be tested in the next decade using cosmological observations [2, 3, 4].

An important work in this era is both developing new cosmological observables to fully explore the new data available and build synergy with already established probes of the standard cosmological model, and exploring new observational possibilities that allow us to test previously unreachable theoretical predictions. The recent detection of a statistically significant cosmic gravitational wave background signal was made 40 years after its theoretical prediction [5], and demonstrates the importance of pursuing long term research programs to test already established theoretical predictions. As observational capabilities develop, theory must follow in modeling cosmological phenomena to ever greater accuracy.

The redshift drift, first derived in the 1960's by Sandage and McVittie [6, 7], is the theoretical prediction that in generic expanding cosmological models, one should observe a time variation of the redshift of distant sources, due to a non-constant expansion rate of the scale factor. As a quantity whose definition relies only on derivatives of the scale factor, and is measured through the

observation of the time variation of an object's spectra, it is an intrinsically geometric observable, and does not rely on prior assumptions on the Universe's energy content or matter distribution. As such, it provides an independent test of the late time acceleration of the Universe and a probe into the Universe's real-time evolution. A first measurement of the cosmic drift is one of the main objectives of the ELT ANDES spectrograph [3], and in the past decades the theoretical understanding of the redshift drift has been extended to include inhomogeneous and anisotropic cosmological models [8, 9], where it was shown to be a possible test of cosmic homogeneity and isotropy.

This thesis is an introduction to the state-of-the-art literature and research on redshift drift and gives for the first time a fully gauge-invariant treatment of the redshift drift in realistic ΛCDM cosmologies, which also allows us to derive the power spectrum of redshift drift fluctuations. This gauge-invariant formalism clarifies the main contaminating effects in measurements of the cosmic redshift drift and their scale and redshift dependencies, which allows one to accurately interpret and model future observations of the redshift drift.

To further validate and check our theoretical predictions, we derive the redshift drift fluctuations using both Einstein-Boltzmann codes and n-body simulations. The numerical implementation in Einstein-Boltzmann solvers provide a streamlined way to obtain the redshift drift fluctuation power spectrum, ready for future cosmological inference and tests when data is available; and n-body simulations provide a first glimpse at future measurements of the redshift drift from large scale surveys, giving a first estimate for the shot noise and variance in the observed spectra, as well as a first probe into how nonlinear growth should impact linear predictions of the effect, where constraining contaminating effects according to the survey's capabilities will be of utmost importance.

In chapter 2, we review the standard ΛCDM cosmological model, its predictions and the mathematical formalism of cosmological perturbation theory and the power spectra of cosmic fields.

In chapter 3 we detail both the theoretical and observational aspects of the redshift drift, the Sandage-Loeb test and its importance as a test of the late time acceleration of the Universe,the main observational programme to measure it, current plans for observations and forecasts and, at last, extend the mathematical definition of the redshift drift to general spacetimes.

In chapter 4 we derive the main results of this work: the gauge-invariant expression for the redshift drift in a perturbed FLRW cosmology and its fluctuations power spectrum. We derive the fluctuation power spectra numerically using an implementation through the Einstein-Boltzmann code CLASS, and discuss our results and its impact in the literature.

In chapter 5 we validate our results on the redshift drift fluctuation power spectrum through n-body simulations using the `gadget4` code, and compare our results to previous works using n-body simulations to model a measurement of the redshift drift.

In the final chapter 6 we summarize our results, discuss their context in the current state of the art and future lines of research.

The author and collaborators published during his PhD 5 peer-reviewed first author papers and currently has a paper in preparation containing some of the results of this thesis [10, 11, 12, 13, 14, 15].

Relativistic Cosmology and ΛCDM

In this chapter we introduce the standard model of cosmology: its theoretical basis in General Relativity, the FLRW metric and its perturbations; its main experimental tests and successes; and, at the end, a discussion on the cosmological constant.

In doing so, we develop the mathematical formalism needed to make calculations involving cosmological observables and predictions from cosmological dynamics and statistics.

We start with the Einstein Equations and the hypothesis leading up to the FLRW metric and the Friedmann equations. We then define the main physical quantities that can be observed and predicted just from the background metric and the energy content of the Universe. The pillars of the standard cosmological model which can be derived purely from the background dynamics are detailed.

Secondly, we develop perturbation theory on the FLRW metric and explain the existence of structure in the Universe from the fluctuations on the curvature and energy fields arising from these perturbations. Two of the greatest success of the inhomogeneous cosmological model, the Cosmic Microwave Background Power Spectrum and the formation of structure in the Universe, are discussed

Finally, we discuss some of the ΛCDM shortcomings and tensions, as well as future perspectives in standard cosmology.

2.1. Background Dynamics

Any general relativistic treatment of physical phenomena starts with Einstein's equations

$$R_{\mu\nu} - \frac{1}{2}Rg_{\mu\nu} = \kappa T_{\mu\nu}, \tag{2.1}$$

relating the dynamics of a spacetime, characterized by a pseudo-Riemannian manifold $(\mathcal{M}, g_{\mu\nu})$ to its stress-energy content, characterized by the stress-energy tensor field $T_{\mu\nu}$ defined on the manifold $\mathcal{M}$. κ is Einstein's gravitational constant. One can postulate a matter content in the right-hand side and obtain the corresponding manifold satisfying the equations with proper boundary conditions, or one could start with a manifold with metric $g_{\mu\nu}$ and derive the dynamics of the energy content $T_{\mu\nu}$ on this given manifold.

Solving these equations, either starting from the left side or the right is a notoriously difficult problem in generality due to their nonlinear nature, and there is a vast literature on the classification of manifolds and stress-energy tensor fields satisfying them [16]. Usually, in describing a physical system through Einstein's equations one starts with simplifying assumptions on the symmetry of the spacetime. In the case we are interested in, that of cosmology, these assumptions, based on general physical principles, are the Cosmological principle and the Weyl Postulate.

Suppose we want to describe our Universe by a spacetime and its dynamics by Einstein's equations. We start with the Cosmological principle, which states that as observers we do not occupy a special place in the Universe, and that at large enough scales, any two observers should measure the same properties of the Universe. Mathematically, this is equivalent to the statement that the metric is invariant under translations and rotations.

The second assumption, Weyl's postulate, states that the worldlines of galaxies are a bundle of geodesics, such that at each point in time, except for possibly one point, called the Big Bang, there is a space-like hypersurface intersecting each of these geodesics exactly once. Physically, this means we have an injective time coordinate for all of the observers, except possibly at the origin.

With these two assumptions, the line element of the resulting metric is [17]

$$ds^2 = -c^2 d\tau^2 + \left(\frac{a(\tau)}{1 + \frac{k}{4} x^i x_i} \right)^2 dx^i dx_i, \tag{2.2}$$

called the FLRW metric. The function $a(\tau)$ is the scale factor, measuring the expansion of the cosmological model, and the parameter k is the curvature parameter of the 3 dimensional Riemannian manifold of constant curvature, the three-dimensional space of observers. c is the speed of light.

In order to have a dynamical cosmological model with energy content, we also need a stress-energy tensor. We assume that this tensor is the one of a perfect fluid, which can be written as

$$T_{\mu\nu} = \left(\rho + \frac{p}{c} \right) u_\mu u_\nu + p g_{\mu\nu}, \tag{2.3}$$

where u_μ is the fluid's 4-velocity vector, p is the fluid's pressure, and ρ its density. The metric $g_{\mu\nu}$ in this case is the FLRW metric (2.2). We know from statistical physics the equations of state for dark and baryonic matter, modeled as dust, and radiation, modeled by a photon gas, the main energy components of the Universe. We can write them as

$$p = w\rho \quad \begin{cases} w = 0 & \text{for matter particles,} \\ w = -\frac{1}{3} & \text{for radiation .} \end{cases} \tag{2.4}$$

With both sides of (2.1) set, we can derive our cosmic dynamics through the solution of the resulting differential equations. In the case of the metric (2.2) and the stress-energy tensor (2.3), we find that the dynamical system reduces to a pair of linearly independent differential equations in time, namely the Friedmann equations

$$\left(\frac{\dot{a}}{a} \right)^2 = \frac{\kappa c^2}{3} \sum \rho_i a^{-3(1+w_i)} - \frac{K}{a^2} \tag{2.5a}$$

$$\left(\frac{\ddot{a}}{a} \right) = -\frac{\kappa c^2}{3} \sum (\rho_i a^{-3(1+w_i)} + 3p_i), \tag{2.5b}$$

where $\dot{}$ denotes derivative with respect to the cosmic time coordinate τ, the indexes $_i$ run through the energy components in (2.4), which we label ρ_r for radiation and ρ_m for matter from now on, and w_i is constant. We also have the redefined curvature parameter $K \equiv \frac{k}{4}$.

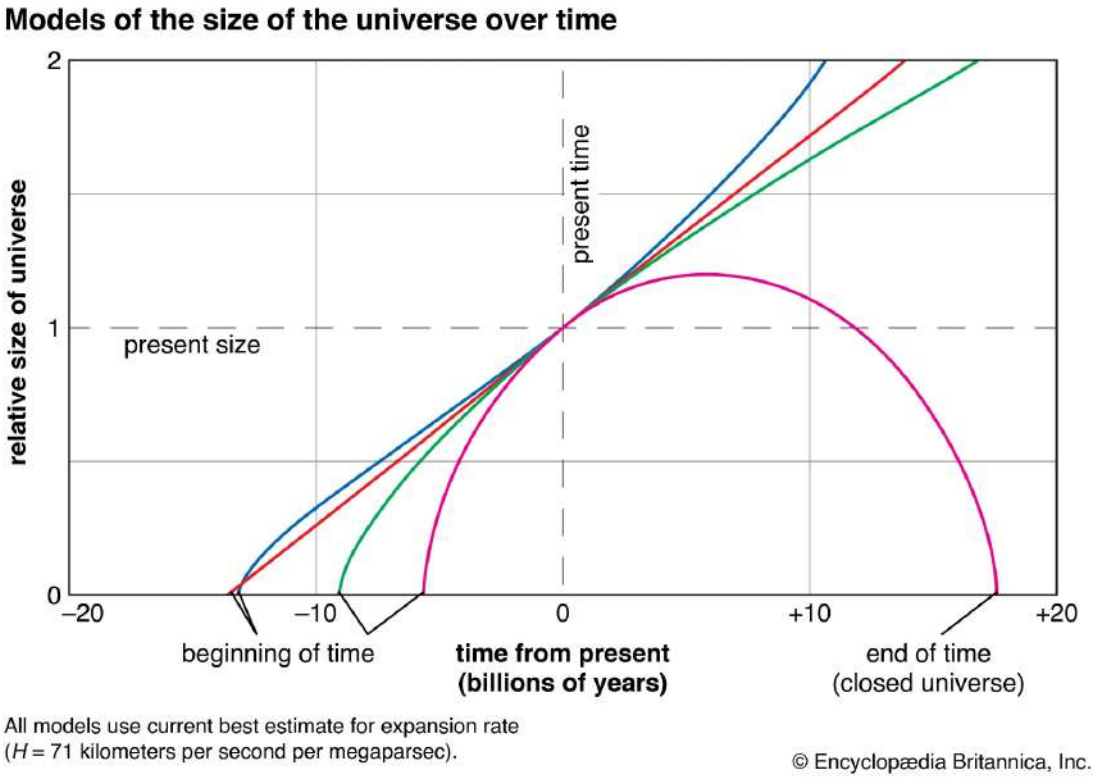

Figure 2.1.: Evolution of the scale factor as a function of time for different cosmologies. The red line shows the evolution for a perfectly flat Universe with no matter content, $K = 0$, $\rho_m = \rho_{\rm crit}$. The purple line shows a Universe that collapses (going to a Big Crunch) due to the amount of matter density $\rho_m = 6\rho_{\rm crit}$. The green curve shows the old CDM model, where the only energy component relevant at current time is matter, and the blue curve is the concordance ΛCDM model. Taken from Encyclopedia Brittanica.

The background dynamics of the Universe, meaning its dynamics at the largest scales, are fully described by equations (2.5a, 2.5b). From these equations, one can obtain the evolution of the scale factor and its rate of change, given by the Hubble parameter

$$H = \frac{\dot{a}}{a}, \tag{2.6}$$

as well as how the distribution of matter changes in the Universe given by the time dependence of $\rho_i(\tau)$. We plot the evolution of the scale factor for different cosmologies in figure 2.1, where we use dimensionful quantities and a Hubble constant value of $H_0 = 71 km/s/Mpc$.

It is useful to define the density parameters for the different energy contents of the Universe, written as fractions of the critical density, the energy density observed today at time τ_0 at which the Universe would be perfectly flat, with $K = 0$. By denoting quantities measured today with the underscore $_0$, the critical density $\rho_{\rm crit}$, we have

$$\rho_{\rm crit} = \frac{3H_0^2}{8\pi G}, \qquad \Omega_i \equiv \frac{\rho_i}{\rho_{\rm crit}}, \tag{2.7}$$

where we have written explicitly the Einstein gravitational constant, defined by

$$\kappa = \frac{8\pi G}{c^4}. \tag{2.8}$$

With these definitions, can conveniently write the first Friedmann equation as

$$H^2 = \Omega_m a^{-3} + \Omega_r a^{-4} + \Omega_K a^{-2} = \sum_{\text{param.}} \Omega_i(a), \tag{2.9}$$

where we have also defined the Curvature density parameter Ω_K, which is the ratio of the curvature term in (2.5a) by the critical density, and did not include yet the cosmological constant term.

The density parameters as a function of the scale factor $\Omega_i(a)$ are then the fraction of the total energy content for each component $_i$ at the moment $a(\tau)$.

2.1.1. Redshift and Hubble-Lemaître law

Suppose an emitter sends a signal at $\tau = \tau_0$, which is then received by an observer at $\tau = \tau_1$. Due to the evolution of the scale factor $a(\tau)$, this signal suffers a modification of its wavelength. Let λ_0 be the wavelength at the emitter and λ_1 the wavelength at the receiver. Then we have

$$\lambda_0 = c\delta\tau_0, \quad \lambda_1 = c\delta\tau_1 \implies \frac{\lambda_1}{\lambda_0} = \frac{\delta\tau_1}{\delta\tau_0} = \frac{a(\tau_0)}{a(\tau_1)}, \tag{2.10}$$

where we used the line element (2.2) of a signal in the last equality. By setting the scale factor of the observer $a(\tau_0) \equiv a_0 = 1$, we can write the change in the wavelength in terms of the redshift z

$$\frac{\lambda_0}{\lambda_1} = \frac{1}{a_0} \equiv 1 + z. \tag{2.11}$$

The redshift z is a measurable quantity, being the amount of frequency change in the spectra emitted by distant sources, and thus probes directly the evolution of the scale factor a and the Hubble parameter H. The relation between the redshift z_S of a distant source and the Hubble constant H_0 is given by the Hubble-Lemaître law. Suppose a source with peculiar velocity v_{pec} is observed at distance r and has a measured redshift z_S. Then the total velocity v at which the source is receding from the observer is

$$\begin{aligned} v &= (\dot{a_S} r) + v_{\text{pec}} = H_0 r + v_{\text{pec}} \\ \implies cz_S &= H_0 r + v_{\text{pec}} \\ \implies z_S &= H_0 \frac{r}{c} + \frac{v_{\text{pec}}}{c} \xrightarrow{v_{\text{pec}}/c \ll 1} \frac{H_0 r}{c}, \end{aligned} \tag{2.12}$$

where we have used the relation $v = cz_S$, obtained directly from the definition of the redshift, and the distance from source to observer r is given by the integral of the line element (2.2).

If the Universe is expanding, that is, $\dot{a_0} > 0$, then the Hubble-Lemaître law states that the receding velocity of distant objects is proportional to their distance to the observer and the Hubble constant. The first experimental measurement of this law was famously done by Hubble [18], and its theoretical interpretation as indicating that the Universe was modeled by the metric (2.2) with an increasing scale factor is due to Lemaître [19]. Together, these formed the basis for the current understanding of a dynamical, expanding Universe.

2.2. The ΛCDM model

The experimental observation of the Hubble-Lemaître law solidified the dynamical cosmological model of a currently expanding Universe, with dynamics governed by the Friedmann equations. To get from the first observation of an expanding Universe to the current concordance model, there was a massive technological and theoretical undertaking, where different observations and theoretical predictions converged to the simplest model able to account for all the different cosmological phenomena: the ΛCDM model.

In this section we list and comment on the fundamental observations and theoretical predictions that together form the basis of the ΛCDM model.

2.2.1. Big Bang Nucleosynthesis

After the observation of the Universe's expansion, by going back in cosmic time, the consequences were that there should be an early time where the Universe was very small, its average temperature was at the energy scale of nuclear reactions and its energy content was radiation dominated, according to (2.9). This scenario, together with the idea that the Universe came from an initial singularity at the beginning of cosmic time is called the hot Big Bang scenario [20].

At the first half of the 20th century, concurrently with the advancement of Cosmology, the development of stellar physics made possible the calculation of the nuclear chain reactions originating elements in supernovas, namely stellar nucleosynthesis, and also the abundance of elements in the Universe according to the observed galaxies and their stellar populations.

The observed abundance of the lightest elements and their isotopes, Hydrogen and Helium, however, was not compatible with the theoretically predicted amount due to stellar nucleosynthesis. In the 40s, the work of George Gamow, Ralph Alpher and Hans Bethe [21] made theoretical predictions for the observed abundance of these elements using the hot Big Bang scenario that matched the observed light element abundances in the Universe, making Big Bang Nucleosynthesis one of the first experimental verifications of the theory.

In figure 2.2 we show a plot of the theoretically predicted element abundance as a function of the matter density in the early Universe, as well as the measurement of the WMAP satellite.

2.2.2. The Cosmic Microwave Background

One of the consequences of the Hot Big Bang scenario is that, at some point in the Universe, photons decoupled from ordinary matter and were able to freely scatter, making the Universe transparent. Big Bang Nucleosynthesis calculations show that around $T \sim 4000K$ protons and electrons recombine to form neutral hydrogen, strongly decreasing the scattering of photons in atoms due to Thomson scattering, and at around $T \sim 3000K$, corresponding to a redshift of $z_{\text{dec}} \sim 1100$, the mean free path of photons becomes larger than the Hubble scale $\sim c/H(z_{\text{rec}})$ and photons freely propagate through the Universe, making it transparent [20]. One can calculate the temperature at which this primordial radiation should be observed and obtain

$$T_{\text{CMB}} \approx 2.7K, \tag{2.13}$$

corresponding to black-body thermal radiation in the Microwave wavelength of the electromagnetic spectrum.

In 1965, Penzias and Wilson published the detection of microwave radiation coming from all directions in the sky with measured temperature within the theoretical predictions for the primordial radiation [22], which was immediately interpreted by Dicke et al as the relic radiation

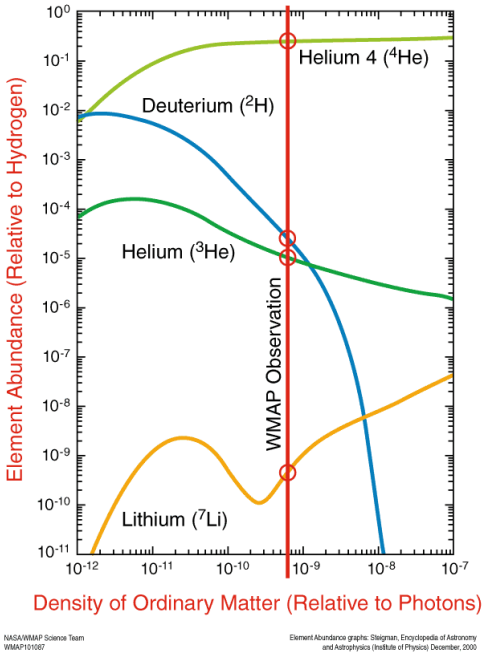

Figure 2.2.: Predicted abundance of elements in the Universe as a function of the matter density parameter. The red line indicates the measurement made by the WMAP satellite of the matter density of the Universe, which is in agreement with the observed elements distributions. Taken from the NASA WMAP website.

emitted after the Hot Big Bang, per the Big Bang Nucleosynthesis calculations [23]. The discovery earned them a Nobel prize and became another successful prediction of Cosmology and the Hot Big Bang. In figure 2.3 we show a simulated image of the CMB radiation as measured by Penzias and Wilson.

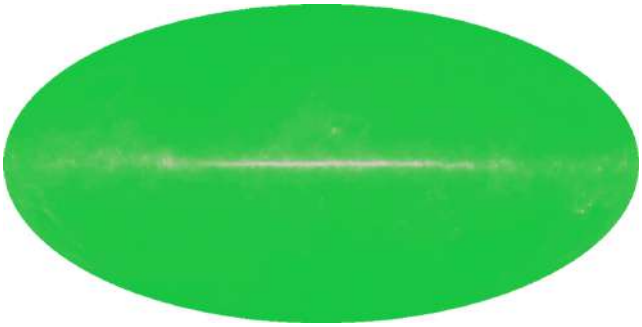

Figure 2.3.: The CMB as measured by Penzias and Wilson in 1965, with an average temperature of $3.5 \pm 1K$. Taken from the NASA WMAP website

2.2.3. Cold Dark Matter

Big Bang Nucleosynthesis predicts the abundance of light elements in the Universe, which should account for the majority of its matter content. Measuring the abundance of these elements thus constrains the Ω_m parameter. What we observe, however, is a matter content 5 times larger

than the Big Bang Nucleosynthesis prediction from cosmic structure and Cosmic Microwave Background observations.

Already in the 30's Fritz Zwicky, by applying the Virial Theorem to galaxies in the Coma cluster, suggested that the observed amount of observed matter in clusters should not be able to properly account for its gravitational potential, something that was later observationally verified in the 70's by Vera Rubin among others. During the 70's due to the observations of galaxy rotation curves and the further theoretical understanding of inhomogeneities in the Universe, the idea that baryonic matter, which interacted with the electromagnetic force is not able to account for the total matter content in the Universe became widely accepted, and the Dark Matter paradigm became established [24].

Theoretical work done by Jim Peebles [25] proposed that Dark Matter should be non-relativistic (i.e. cold), and thus have the same equation of state parameter $w_{\rm CDM}$ as ordinary matter, treated as dust. Observations of galaxy number counts and CMB temperature fluctuations favored this model, in which structure in the Universe is created hierarchically, from smaller gravitationally collapsed objects that grow into larger structures forming the observed Large Scale Structure of the Universe. [20, 24]

2.2.4. The Accelerated Expansion of the Universe

In the 1990's, with the advent of the Hubble telescope and new observational facilities, measurements of the Hubble constant vastly increased in both precision and accuracy, converging to a value of $H_0 \approx 70$km/s/Mpc. This, together with new spectroscopic and photometric capabilities, allowed the observation of distant sources and measurements of their distance to constrain the Hubble law (2.12) and its redshift dependence. Measurements of the age of the oldest stars and distant supernovae were already pointing to a tension in the age of the Universe [26, 27] as calculated from the then standard CDM model.

In 1997-98, Riess, Perlmutter and Schmidt [28, 26, 29] published a series of papers showing that the then current accepted paradigm of a decelerating Universe was not compatible with observations of supernovae at high redshifts, which used the luminosity distance relation [24]

$$\sqrt{\frac{L_S}{4\pi F_S}} = (1+z)\int_0^{z_S} \frac{dz'}{H(z')} \tag{2.14}$$

to constrain the cosmological parameters, with L_S the supernova luminosity and F_S its observed flux. The simplest model able to account for the observations of a Universe in accelerated expansion is the one obtained by adding a positive cosmological constant to Einstein's equations (2.1), resulting in Friedmann's equations (2.9) including a cosmological constant Λ density parameter, now

$$H^2 = \Omega_m(1+z)^3 + \Omega_r(1+z)^4 + \Omega_K(1+z)^2 + \Omega_\Lambda, \quad \Omega_\Lambda \equiv \frac{\Lambda}{\rho_{\rm crit}} \tag{2.15}$$

By the first decade of the new millennium, with measurements both from the Hubble Space Telescope and the WMAP satellite, the existence of a cosmological constant became widely accepted, with a standard cosmological model with a cosmological constant density of $\Omega_\Lambda \approx 0.7$. In figure 2.4 we plot the Hubble diagram obtained by the Supernova Cosmology Collaboration which resulted in the discovery of the accelerated expansion of the Universe, and the 2011 Nobel prize for its three main discoverers.

These observations form the basis of the current concordance cosmological model, namely the ΛCDM model. Relativistic Cosmology, however, has developed beyond describing only the large

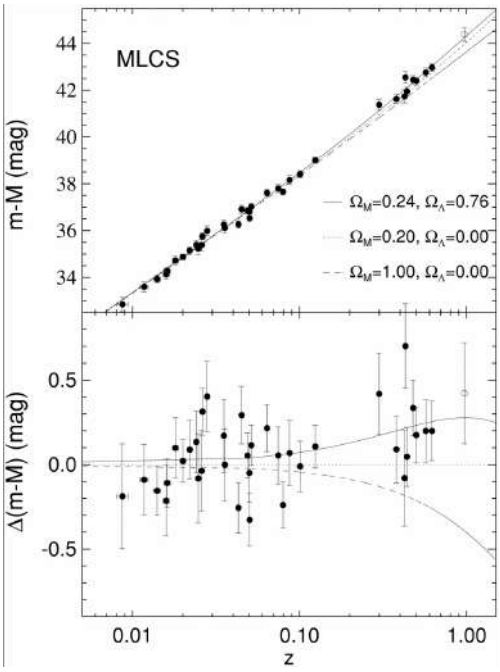

Figure 2.4.: Magnitude-redshift relation obtained from Type Ia supernovae fits to the Hubble diagram. The upper graph shows the fit to observations for different cosmological models, the best one which includes a cosmological constant; the lower graph shows the absolute magnitude variation for each observed supernovae.

scale behavior of the Universe, and the ΛCDM model also accounts for cosmological dynamics at scales where the Universe cannot be modeled as perfectly homogeneous and isotropic, and the cosmological principle becomes a statistical hypothesis on the average behavior of cosmological dynamics. In the next section we develop the needed mathematical formalism to describe the precision tests cosmology went through, from fluctuations in the Cosmic Microwave Background to the description of large scale structure dynamics.

2.3. Structures in the Universe

The Cosmological Principle dictates the large scale behavior of Cosmological dynamics, and the Friedmann equations (2.15) are valid at sufficiently large scales, where the energy content of the Universe can be taken to be very nearly constant. A characteristic scale for large scale cosmological dynamics is given by the comoving Hubble radius

$$r_{\mathrm{H}} \equiv \frac{c}{a(\tau)H(\tau)}. \tag{2.16}$$

For a sphere with Hubble radius centered around a particle, all particles outside the sphere cannot interact causally with this particle at time τ. In an ever expanding Universe, this scale sets a causal boundary, where particles separated by distances greater than the Hubble horizon cannot interact with each other for $\tau_0 > \tau$ [24].

The Hubble radius is then a characteristic scale where one can safely neglect particle interactions, and only the cosmic dynamics of (2.15) are taken into account.

Inside the Hubble radius, however, we observe gravitationally bound structures. Galaxies interact gravitationally inside galaxy clusters, clusters have their own peculiar velocities and follow the Hubble flow in a inhomogeneous distribution locally; and the CMB is not perfectly isotropic, but shows small anisotropic and inhomogeneous deviations from a black body thermal spectrum due to gravitational and electromagnetic interactions.

The mathematical tool best suited to describe all of these effects, namely small deviations from homogeneity and isotropy, is Cosmological Perturbation Theory, where one writes deviations from the FLRW metric as perturbations in the metric and stress-energy tensors, and obtain the dynamical equations for the evolution of these perturbations from the background solution.

After developing linear cosmological perturbation theory, in order to link theory with observations, we derive the CMB anisotropy and galaxy number count power spectra, two observations that are well described by linear perturbation theory on FLRW and another success of the ΛCDM model. We use fully gauge-invariant variables, which are the true physically observed quantities.

2.3.1. Perturbation Theory in FLRW space-time

We start by assuming that the metric $g_{\mu\nu}$ and the stress energy tensor $T_{\mu\nu}$ of the observable Universe are close to the Robertson-Walker $\bar{g}_{\mu\nu}$, $T_{\mu\nu}$ to first order, formally

$$\frac{|g_{\mu\nu} - \bar{g}_{\mu\nu}|}{\max_{\{\mu\nu\}} \bar{g}_{\mu\nu}} < \mathcal{O}(\epsilon), \qquad \frac{|T_{\mu\nu} - \bar{T}_{\mu\nu}|}{\max_{\{\mu\nu\}} \bar{T}_{\mu\nu}} < \mathcal{O}(\epsilon), \tag{2.17}$$

where ϵ is a smallness parameter, $\epsilon \ll 1$. The perturbations are then a map between the observed manifold with stress-energy tensor $T_{\mu\nu}$, $(\mathcal{M}, g_{\mu\nu})$. By choosing the background metric and perturbing it to first order, we are looking at a ϕ that keeps the background tensors $\bar{T}$ and $\bar{g}$ fixed to order ϵ. We can describe this infinitesimal variation in the metric $\bar{g}$ as the flow of a vector field ξ parametrized by ϕ^{ξ}. The push-forward of the metric under this diffeomorphism then must be

$$\phi_*(g_{\mu\nu}) = g_{\mu\nu} + \epsilon L_{\xi} \bar{g}_{\mu\nu} + \mathcal{O}(\epsilon^2) g_{\mu\nu}. \tag{2.18}$$

We show a depiction of this diffeomorphism in figure 2.5. By writing the perturbed metric $g_{\mu\nu}$ as

$$g_{\mu\nu} = \bar{g}_{\mu\nu} + \epsilon a^2 h_{\mu\nu}, \tag{2.19}$$

we see that the metric perturbation $h_{\mu\nu}$, using (2.18), transforms under infinitesimal diffeomorphisms of the form above as

$$h_{\mu\nu} \to h_{\mu\nu} + a^{-2} L_{\xi} \bar{g}_{\mu\nu}. \tag{2.20}$$

The transformations described by (2.20) are gauge transformations, which, due to the diffeomorphism invariance of the background quantities, describe the same metric but have different parametrizations in terms of metric dependent variables. Physically relevant variables, that is, quantities that we are able to measure, should not be gauge-dependent, since they are observer independent and coordinate-invariant.

In this work, we'll use gauge-invariant perturbations, such that there is no ambiguity in understanding which variables are physically relevant and it becomes clear the connection between certain gauges and the relevant physical quantities, such as the gravitational potentials. An important first result in this direction is the Stewart-Walker lemma [30], which claims that for a perturbation to be gauge invariant, it must be constant or vanish at the background level, meaning that it leaves the background metric invariant under its change. This can be seen directly

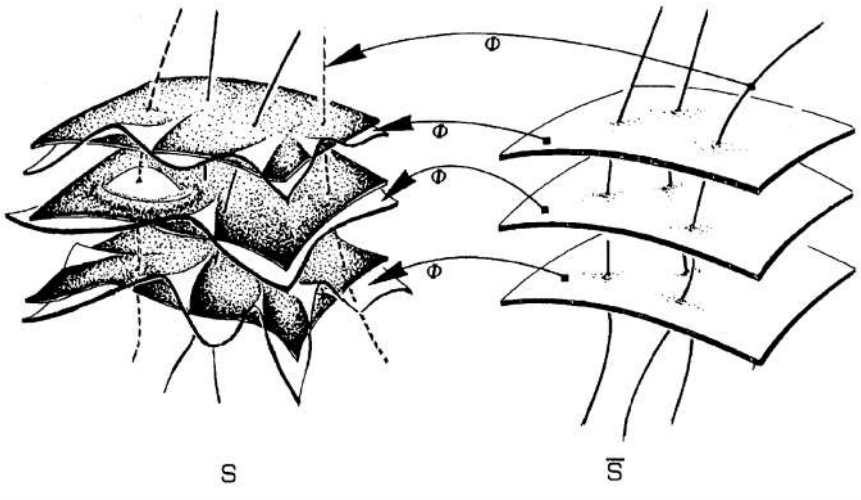

Figure 2.5.: Diffeomorphism Φ between the background, idealized FLRW manifold $\bar{S}$and the observed, perturbative FLRW manifold S. The pushforward of this diffeomorphism defines a gauge map between the background and the perturbed metric, which we choose to be the identity up to a linear term. Image taken from [31]

.

from (2.20), which shows that the term $L_\xi \bar{g}_{\mu\nu}$ should vanish in order to keep the perturbation of the metric invariant under infinitesimal transformations.

2.3.1.1. Gauge Invariant Variables

In order to obtain the gauge-invariant variables for the metric and stress-energy tensor, we start with the most general form of a perturbed FLRW metric to linear order, which can be fully described by scalar fields on the coordinates using the Scalar-Vector-Tensor decomposition, a result first obtained by Lifschitz. We will follow closely the treatment given in [20] throughout the section. A rigorous and comprehensive derivation of this metric through the SVT decomposition can be found in [32]. The metric is

$$ds^2 = a^2(t)\left[-c^2(1+2A)dt^2 - 2B_i dx^i dt + (\delta_{ij} + H_{ij})\, dx^i dx^j\right], \tag{2.21}$$

where the SVT decomposition allows us to write the tensors H_{Tij} and B_i as gradients and laplacians of scalar functions. Each of these tensors transforms independently under coordinate change according to their tensorial nature, such that perturbations modes do not couple to first order [33], meaning that we can analyze their evolution independently. From here on, when we mention perturbation theory, we mean linear perturbation theory. Nonlinear perturbations and their evolution are described succintly in [24].

The SVT decomposition allows us to write the tensor and vector perturbations as

$$\begin{aligned} &H_{ij} = H_L\delta_{ij} + H_{T\,ij} \qquad \text{with} \qquad H_{T\,ij} = \partial_i\partial_j H_T - \frac{1}{3}\delta_{ij}\Delta H_T, \\ &B_i = \partial_i B, \end{aligned} \tag{2.22}$$

where $\Delta = \sum \partial_i^2$ denotes the flat space Laplacian. Thus, scalar, linear metric perturbations are encoded in four functions: A, B with $B_i = \partial_i B$, H_L and H_T. In figure 2.6 we depict the role of these 4 functions in fixing the gauge used in the coordinate map

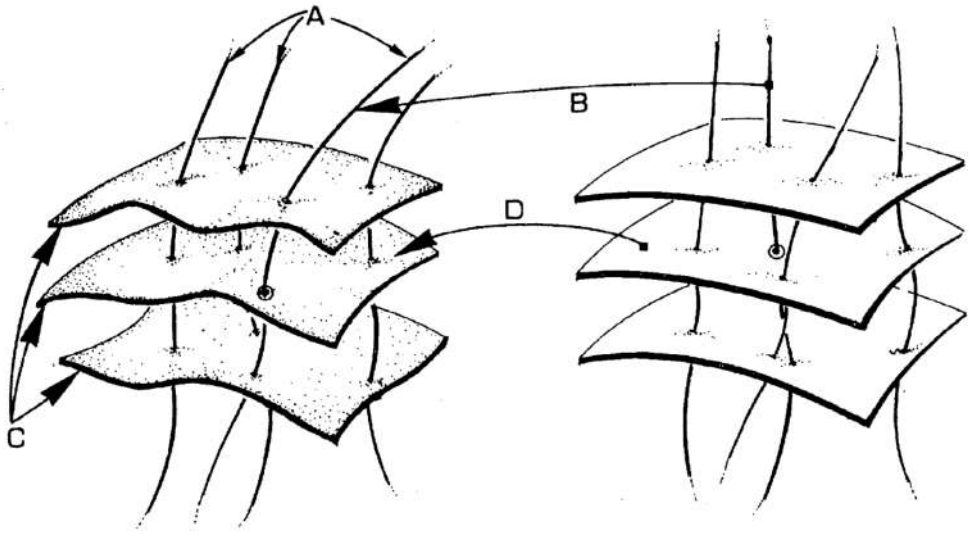

Figure 2.6.: Figure depicting the role of the 4 functions describing the perturbed metric (2.21), in the notation of [31], where the figure is taken from. The choise of A and B define the time slicing of the gauge, while $C = H_T$ and $D = H_L$ fix the chart between the spatial hypersurfaces.

Since our work focuses on post-reionization and late-time cosmology, we restrict ourselves to scalar perturbations. Furthermore, we are able to safely neglect vector and tensor perturbations. Vector perturbations decay in an FLRW background [20] and the contribution from tensor perturbations is small compared to scalar perturbations, see e.g. CMB data [34].

In order to obtain gauge-invariant variables of the metric, we should analyze their transformations under infinitesimal variations described in (2.20) and obtain linear combinations of the metric functions in (2.21) that are invariant under these transformations. This work is done extensively in [20, 33] and we refer the reader to appendix A for the full set of gauge-invariant variables and the transformation laws of the metric functions. Here we just write the metric gauge-invariant variables, given by

$$\Psi = A - \mathcal{H}\sigma_t - \dot{\sigma}_t, \tag{2.23a}$$

$$\Phi = -\mathcal{R} + \mathcal{H}\sigma_t, \qquad \text{with,} \quad \sigma_t = \dot{H}_T - B, \tag{2.23b}$$

where σ_t is the shear in a simultaneity hypersurface, and therefore not gauge-invariant, as it depends of a specific time slice, and it is useful to note that we use the conformal Hubble parameter, defined by

$$\mathcal{H} \equiv aH = \dot{a}, \tag{2.24}$$

the Hubble parameter for the comoving coordinates of the metric (2.21) $da/d\tau$.

In order to describe the full dynamics of our perturbed cosmology, we still need the stress-energy tensor perturbations and their dynamical relations with the metric potentials through the Einstein Equations.

We now write the parametrization of the full observed stress-energy tensor and its energy density ρ and 4-velocity u^μ. We define the 4-velocity of the fluid as being the time-like eigenvector

and eigenvalue of the full energy tensor,

$$T_{\mu\nu} = \bar{T}_{\mu\nu} + \theta_{\mu\nu}, \qquad T^{\mu}_{\nu} u^{\nu} = -\rho u^{\mu}, \qquad g_{\mu\nu} u^{\nu} u^{\mu} = -1, \tag{2.25}$$

$$\rho = \bar{\rho}(1+\delta), \qquad u = u^0 \partial_t + u^i \partial_i, \tag{2.26}$$

where u^0 is fixed by the normalization, and we decompose its space-like part as the partial derivative of a scalar velocity potential v, which can always be done using the Helmholtz decomposition [20]:

$$u^0 = \frac{1}{a}(1-A), \qquad u^i = \frac{1}{a} v^i = \frac{1}{a} \partial_i v. \tag{2.27}$$

We define then the projection tensor on the hypersurface orthogonal subspace of u^μ as $P^\mu_\nu \equiv u^\mu u_\nu + \delta^\mu_\nu$. By defining the stress-tensor

$$\tau^{\mu\nu} = P^\mu_\alpha P^\nu_\beta T^{\alpha\beta}, \tag{2.28}$$

we are able to write the full stress-energy energy tensor as

$$T^\mu_\nu = \rho u_\mu u_\nu + \tau^\nu_\mu, \tag{2.29a}$$

$$\tau^i_j = \bar{P}\left[(1+\pi_L)\delta^i_j + \Pi^i_j\right], \quad \Pi^i_i = 0, \tag{2.29b}$$

$$\tau^0_0 = 0, \quad \tau^j_0 = \bar{P} v^j, \quad \tau^0_j = \bar{P}(v_j - B_j). \tag{2.29c}$$

We see that in the case where perturbations vanish, τ gives the pressure contribution $\tau_{ij} = \bar{P}\delta_{ij}$. In equations (2.29) we have once again used the SVT decomposition in order to write the spatial part of the perturbed stress-energy tensor as the sum of a symmetric and a traceless component. The traceless part of the stress-energy tensor Π^{ij} is called the anisotropic stress, and accounts for the anisotropic component not present in the background stress-energy fluid. Since the anisotropic stress vanishes identically at the background level, the Stewart-Walker lemma guarantees that it is a gauge-invariant quantity.

Again, through a linear combination of the perturbative quantities of the stress-energy tensor, we find gauge-invariant variables describing its fluctuations. We refer the reader to appendix A for the full transformation laws of these quantities and the gauge-invariant variables. The other gauge-invariant variable obtained from the stress-energy tensor is $\Gamma \equiv \pi_L - \frac{c_S^2}{w}\delta$, with c_S the sound speed of the fluid.

With these quantities in hand, we are able to write the velocity and density perturbation gauge-invariant quantities:

$$V \equiv v - \dot{H}_T \tag{2.30a}$$

$$D_S \equiv \delta + 3(1+w)\mathcal{H}(\dot{H}_T - B) \tag{2.30b}$$

$$D \equiv D_S + 3(1+w)\mathcal{H} v \tag{2.30c}$$

$$D_g \equiv D_S - 3(1+w)\Phi. \tag{2.30d}$$

By using the kinematic decomposition of the coordinate-independent fluid 4-velocity u^μ, we can write gauge-invariant variables that have a physical interpretation in terms of the expansion, acceleration, shear and vorticity of the fluid. We write explicitly [20]

$$u_{\mu;\nu} = \frac{1}{3} P_{\mu\nu}\theta - a_\mu u_\nu + \sigma_{\mu\nu} + \omega_{\mu\nu}, \tag{2.31}$$

where we note that ; means the covariant derivative of the tensor field, and $P_{\mu\nu}$ the projection tensor defined in (2.28). θ is the expansion, a_μ the 4-acceleration, $\sigma_{\mu\nu}$ and $\omega_{\mu\nu}$ the vorticity. These quantities can be written as

$$\theta = \frac{3}{a}\mathcal{H}\left[1 - A + \mathcal{H}^{-1}(\dot{H}_L + v)\right] \tag{2.32a}$$

$$a^i = -\partial^i \mathcal{A}, \quad a^0 = 0, \quad \text{with} \tag{2.32b}$$

$$\mathcal{A} = \frac{1}{a^2}\left(\dot{B} - \dot{v} + A + \mathcal{H}(B - v)\right) = \frac{1}{a^2}\left(-\dot{V} - \mathcal{H}V + \Psi\right), \tag{2.32c}$$

$$\sigma_{ij} = a\left(\partial_i\partial_j - \frac{1}{3}\delta_{ij}\Delta\right)\sigma, \quad \sigma_{00} = 0 = \sigma_{0i} = \sigma_{i0}, \quad with \tag{2.32d}$$

$$\sigma = a(\dot{H}_T - v), \tag{2.32e}$$

$$\omega_{\mu\nu} = 0. \tag{2.32f}$$

It is easy to check that, with the exception of the expansion θ, all of the kinematic quantities are gauge-invariant, since we can write them as linear combinations of (2.30) and (2.23). Another way to arrive at this result is by noticing that the only quantity that does not vanish at the background is the expansion θ, which is a multiple of the Hubble parameter at the background.

2.3.1.2. Longitudinal and Synchronous Gauges

Here we briefly describe two of the most commonly used gauges in the literature: the Longitudinal or Newtonian gauge, and the Synchronous gauge. A full description and mapping between these gauges in given in [35].

In the Newtonian gauge, one uses the gauge freedom to set the scalar functions of the perturbed metric (2.21) as

$$A = \Psi + \mathcal{H}\sigma_t + \dot{\sigma}_t, \qquad B = 0\,, \tag{2.33}$$

$$H_L = -\Phi + \frac{1}{3}\Delta H_T + \mathcal{H}\sigma_t, \qquad H_T = 0\,. \tag{2.34}$$

Where Φ and Ψ are the Bardeen potentials defined in (2.23). In the Newtonian gauge, the metric functions A and H_L assume a role similar to the Newtonian gravitational potential in the weak field limit of General Relativity, and have an intrinsic physical meaning since the non-vanishing scalar functions are equal to the Bardeen potentials, which are gauge-invariant.

In the synchronous gauge, the scalar functions are defined such that observers share the same space-like t = constant hypersurfaces, and thus that the time part of the metric is unperturbed, i.e. $g_{00} = \bar{g}_{0i} = 0$. In this case, we have in equation (2.21)

$$A = 0, \quad B = 0\,. \tag{2.35}$$

Unlike in the Longitudinal gauge, the synchronous gauge does not make use of the whole gauge freedom in setting the scalar functions of the metric, and thus spurious degrees of freedom may appear in the dynamical equations for the perturbations. One of the main reasons for using this gauge is that it sets a hypersurface of constant time common to all cosmic observers.

2.3.2. Perturbed Einstein's Equations

The full derivation of Einstein's equations for the metric (2.21) and the stress-energy tensor (2.29) are long and involved, in particular using gauge-invariant quantities. For a detailed derivation of the equations, in both gauge-invariant and the synchronous and comoving gauges, the reader is referred to the papers [33, 35]. Here we list the dynamical and conservation equations and derive the evolution of the gauge-invariant density and velocity. We then obtain the Bardeen equation, which governs the time evolution of the gauge-invariant gravitational potentials (2.23), also called the Bardeen potentials. Before connecting these quantities to the observation of the CMB anisotropies and matter power spectra , we apply the equations to the important special case of a pure dust fluid.

Einstein's equations $R_{\mu\nu} - \frac{1}{2}Rg_{\mu\nu} = \kappa T_{\mu\nu}$ for the metric (2.19) and the stress-energy tensor (2.29) are given by

$$\frac{\kappa}{2}a^2\rho D = -\left(\Delta + 3K\right)\Phi \qquad (00) \qquad (2.36a)$$

$$\frac{\kappa}{2}a^2(\rho + P)V = \mathcal{H}\Psi - \dot{\Phi} \qquad (0i) \qquad (2.36b)$$

$$-\Delta(\Phi + \Psi) = \kappa a^2 P\Delta\Pi \qquad (ij)\,, i \neq j \qquad (2.36c)$$

$$\ddot{\Phi} + 2\mathcal{H}\dot{\Phi} + \mathcal{H}\dot{\Psi} + \left[2\dot{\mathcal{H}} + \mathcal{H}^2 + \frac{\Delta}{3}\right]\Psi = \frac{\kappa}{2}a^2\rho\left[\frac{1}{3}D + c_s^2 D_s = w\Gamma\right] \qquad (ij)\,, i = j, \qquad (2.36d)$$

where Δ denotes the spatial Laplacian, the speed of sound is defined by $c_s^2 = \delta P/\delta\rho$ and K is the spatial sectional curvature of the 3-metric in (2.5b). The conservation of the stress-energy tensor gives us

$$\dot{D}_g + 3(c_s^2 - w)\,\mathcal{H}D_g - (1+w)\Delta V + 3w\mathcal{H}\Gamma = 0 \qquad (2.37a)$$

$$\dot{V} + \mathcal{H}(1 - 3c_s^2)V = (\Psi - 3c_s^2\Phi) + \frac{c_s^2}{1+w}D_g + \frac{w}{1+w}\left[\Gamma + \frac{2}{3}(\Delta + 3K)\Pi\right]. \qquad (2.37b)$$

In order to close the dynamical system in time $(\Pi, \Gamma, D, V, \Psi, \Phi)$ we still need one more equation. By using the definition of the gauge invariant quantities D and D_g and the (00) and (ij) equations (2.36), the (ii) equation (2.36) leads to the Bardeen equation

$$\ddot{\Phi} + 3\mathcal{H}(1 + c_s^2)\dot{\Phi} + \left[3(c_s^2 - w)\mathcal{H}^2 - (2 + 3w + 3c_s^2 + 3c_s^2)K - c_s^2\Delta\right]\Phi$$
$$= \kappa a^2 P\Delta\left[\mathcal{H}\dot{\Pi} + [2\dot{\mathcal{H}} + 3\mathcal{H}^2(1 - c_s^2/w)]\Pi + \frac{\Pi}{3} + \frac{\Gamma}{2}\right], \qquad (2.38)$$

which closes the dynamical equations for the perturbation variables once the matter content is given by the equation of state (2.4). It is common to write the equations in terms of the velocity and density perturbations D and V, which are physically measurable, but in this work we will usually express quantities in terms of the Bardeen potentials Φ and Ψ.

As an application, we describe the evolution of an adiabatic perfect fluid, in which case the anisotropic stress vanishes, $\Pi_{ij} = 0$ and the gauge-invariant quantity Γ also vanishes identically since there is no variation of the entropy flux [20]. In this case, we have $\Phi = \Psi$ from (2.36), and (2.38) becomes

$$\ddot{\Psi} + 3\mathcal{H}(1+c_s^2)\dot{\Psi} + \left[(1+3c_s^2)(\mathcal{H}^2 - K) - (1+3w)(\mathcal{H}^2 + K) - c_s^2\Delta\right]\Phi = 0, \tag{2.39}$$

which is a damped wave equation. For flat cosmologies $K = 0$ and a constant equation of state $\delta\rho = c_s^2\delta p = w\delta p$, the equation becomes [20]

$$\ddot{\Psi} + 6\frac{1+w}{(1+3w)t}\dot{\Psi} - w\Delta\Psi = 0, \tag{2.40}$$

where we've used the background values of a and $\mathcal{H}$ for a perfect fluid cosmology, as in (2.15). By going to Fourier space

$$\Delta \longleftrightarrow -k^2, \tag{2.41}$$

we are able to find an analytical solution for the potential Ψ of the form

$$\Psi(t) = \frac{1}{a(t)}\left(Aj_\ell(\omega^{1/2}kt) + By_\ell(w^{1/2}kt)\right), \tag{2.42}$$

where j_ℓ and y_ℓ are the Spherical Bessel functions of order ℓ [36]. By analyzing the asymptotic and small behavior of the Bessel functions we find that for evolution inside the Hubble horizon $\omega^{1/2}kt \gg 1$, the growing mode A oscillates with frequency $w^{1/2}k$ and the B mode decays as $1/(ta)$. For modes outside the Hubble horizon $\omega^{1/2}kt \ll 1$, the A-mode remains constant while the B-mode decays as $1/ta^2$. The dust case is particularly interesting, since $w = 0$ and in the sub-Hubble scales the perturbations grow as

$$\Psi = A + \frac{B}{(kt)^5}, \tag{2.43}$$

meaning that, at the largest scales, CDM and standard matter perturbations are approximately constant and start to oscillate slowly when entering sub-horizon scales. This shows that in the matter-dominated age of the Universe, the gravitational potential Ψ describing the interaction of large-scale structure remains nearly constant, and taking it as constant is a good approximation to linear order [20, 24].

2.3.3. Power Spectra of Cosmological Observables

In order to constrain cosmological parameters and map observations to theoretical predictions, it is necessary to take into account that what we observe with surveys and telescopes is usually a random field X distributed across the celestial sphere, with direction given by a vector $\mathbf{n}$. In order to understand how the statistical distribution of the field on the celestial sphere implies a certain cosmology, we analyze its Power Spectrum. By expanding the field $X(\mathbf{n})$ inside the two point correlation function $\langle X(\mathbf{n}_1)X(\mathbf{n}_2)\rangle$ into spherical harmonics on the sphere $Y_{\ell m}(\mathbf{n})$, one finds the expansion coefficients $a_{\ell m}$ which contain the statistical information on the cosmological model, and can be theoretically predicted using the perturbation theory developed in this section. Thus, by decomposing the observed field into spherical harmonics and obtaining its coefficients, one can obtain constraints on the cosmological parameters by comparing the observed $a_{\ell m}^{\text{obs}}$ and the theoretically predicted $a_{\ell m}^{\text{theo}}$.

The power spectra of cosmological observables is a fundamental tool in cosmology and we use it extensively in this thesis. Here we briefly describe how to map fields obtained from surveys and simulations to the theoretical predictions from cosmological perturbation theory through the

use of the power spectrum and the angular power spectrum. Extensive definitions and the full statistical treatment of this important topic can be found in the standard texts [24, 20].

Let $X(\mathbf{n})$ be a random field defined on the celestial sphere $\mathcal{S}$, $X : \mathbf{n} \to X(\mathbf{n})$, where X is distributed according to some known statistical distribution with probability density function $p(x)$ at each point in the celestial sphere. Its 2-point correlation function is given by the correlation of the field at two points $(\mathbf{n}_1, \mathbf{n}_2)$

$$\langle X(\mathbf{n}_1)X(\mathbf{n}_2)\rangle \equiv C(\mathbf{n}_1, \mathbf{n}_2), \tag{2.44}$$

where $C(\mathbf{n}_1, \mathbf{n}_2)$ is the correlation between the two random variables $X(\mathbf{n}_1)$ and $X(\mathbf{n}_2)$ with same probability distribution p, defined in appendix B.

We can expand the field X in spherical harmonics defined on the sphere as

$$X(\mathbf{n}) = \sum_{\ell m} a_{\ell m} Y_{\ell m}, \tag{2.45}$$

and refer the reader to appendix B for the definition of the spherical harmonics on the sphere. Here $a_{\ell m}$ are complex functions.

By using the expansion above in (2.44), we obtain

$$\langle X(\mathbf{n}_1)X(\mathbf{n}_2)\rangle = \sum_{\ell m \ell' m'} \langle a^*_{\ell' m'} a_{\ell m}\rangle Y_{\ell m}(\mathbf{n}_1) Y_{\ell' m'}(\mathbf{n}_2) \tag{2.46}$$

The cosmological principle in a Universe with structure ascertains that fields in the sky are statistically homogeneous and isotropic, and thus their correlation at different points $\mathbf{n}_1$ and $\mathbf{n}_2$ should not be position or direction dependent, such that

$$\sum_{\ell m \ell' m'} \langle a^*_{\ell' m'} a_{\ell m}\rangle = \sum_{\ell m \ell' m'} \delta_{\ell \ell'} \delta_{m m'} C_\ell \tag{2.47}$$

In this case, the decomposition (2.46) becomes diagonal and is given by [20]

$$\begin{aligned}
\langle X(\mathbf{n}_1)X(\mathbf{n}_2)\rangle &= \sum_{\ell m \ell' m'} \delta_{\ell \ell'} \delta_{m m'} C_\ell Y_{\ell m}(\mathbf{n}_1) Y_{\ell' m'}(\mathbf{n}_2) \\
&= \frac{1}{4\pi} \sum_{\ell} C_\ell (\mathbf{n}_1 \cdot \mathbf{n}_2) P_\ell (\mathbf{n}_1 \cdot \mathbf{n}_2) \\
&\equiv \frac{1}{4\pi} \sum_{\ell} (2\ell + 1) C_\ell(\mu) P_\ell(\mu),
\end{aligned} \tag{2.48}$$

where P_ℓ is the Legendre polynomial of order ℓ and the orthogonality relations of the Spherical Bessel Functions were used. We also defined the angle between the two vectors $\mu \equiv \mathbf{n}_1 \cdot \mathbf{n}_2$. We once again refer the reader to the appendix B for extensive definitions. The previous result also shows that statistical isotropy and homogeneity implies in diagonal coefficients for the harmonic decomposition of a field; and thus we can test cosmological homogeneity and isotropy by constraining the $a_{\ell m}$'s.

By setting the convention for the Fourier transform in 3 dimensions as

$$\hat{f}(\mathbf{k}) \equiv \frac{1}{(2\pi)^3} \int_{\mathbb{R}^3} d^3x \, f(\mathbf{x}) \, e^{i\mathbf{k}\cdot\mathbf{x}}, \tag{2.49}$$

we find the Power Spectra $P_X(k)$ of a statistically homogeneous and isotropic field through

$$\begin{aligned}\langle X(\mathbf{k})X(\mathbf{k}')\rangle &= \int d^3x' \int d^3x C(\mathbf{x},\mathbf{x}')e^{i(\mathbf{k}\cdot\mathbf{x}-\mathbf{k}'\cdot\mathbf{x}')} \\ &= (2\pi)^3\delta(\mathbf{k}-\mathbf{k}')P_X(k).\end{aligned} \tag{2.50}$$

Thus, for a statistically homogeneous and isotropic field $X(\mathbf{n})$ on the celestial sphere, we obtain its power spectrum by the Fourier transform of its 2-point correlation function $\langle X\mathbf{n}X\mathbf{n}\rangle$

$$P_X(k) = \langle \widehat{X(\mathbf{n})X(\mathbf{n})}\rangle. \tag{2.51}$$

Cosmological observations rely on the statistics of the 2-point correlation functions of objects and fields in the sky, and as such the theoretical Power Spectra P_X is directly related to these observations.

Furthermore, by using the decomposition (2.45), we define the Angular Power Spectrum of the field X as

$$C_\ell^X = \langle |a_{\ell m}^X|^2\rangle, \quad \text{where} \quad a_{\ell m} = \int d\Omega_{\mathbf{n}} X(\mathbf{n})Y_{\ell m}^*(\mathbf{n}), \tag{2.52}$$

where $d\Omega_{\mathbf{n}}$ denotes integration over the whole sky area. For statistically homogeneous and isotropic fields, there is no dependence on m [20]. By applying (2.54) to the Fourier transform of the field and using the orthogonality of the Spherical Harmonics, we can write [20, 37]

$$a_{\ell m} = \frac{i^\ell}{2\pi^3}\int d^3k j_\ell(kn)X(\mathbf{k})Y_{\ell m}(\hat{\mathbf{k}}), \tag{2.53}$$

and obtain the angular power spectrum in terms of the power spectrum and the Kernel function F_ℓ of the field X through the use of equation (2.46)

$$C_\ell^X = \frac{2}{\pi}\int dk k^2 P_X(k)F_\ell^2(k), \tag{2.54}$$

where $n = |\mathbf{n}|$ and the Kernel for the field $X(k)$ is given by

$$F_\ell(k) \equiv j_\ell(kn). \tag{2.55}$$

We also define the dimensionless power spectrum of the field X by the relation

$$\mathcal{P}_X(k) \equiv \frac{k^3}{2\pi^2}P_X(k). \tag{2.56}$$

The dimensionless power spectrum has the same dimension as the field X squared, and relates to the correlation function $C(n_1, n_2)$ straightforwardly through equation (2.50) for statistically homogeneous and isotropic fields [20]

$$C(x,y) = \int \frac{dk}{k} j_0(kr)\mathcal{P}_X(k), \tag{2.57}$$

where $r = |x-y|$. Fields where $\mathcal{P}_X(k)$ does not depend on k are called scale-invariant fields, and in this case the correlation function (2.57) is not a function of the distance $|x-y|$. Furthermore, using the adimensional power spectrum, we are able to write (2.54) as

$$C_\ell^X = 4\pi\int \frac{dk}{k}\mathcal{P}_X(k)F_\ell^2(k). \tag{2.58}$$

With all the mathematical tools in hand, we are able to make theoretical predictions and study their matching to observations. In the next section we describe two of the most successful predictions of the ΛCDM and Big-Bang cosmology: the CMB anisotropy angular power spectrum and the matter power spectra.

2.3.4. CMB Anisotropies and Power Spectrum

When Penzias and Wilson first observed the CMB, telescopes weren't able to fully resolve the signal such that deviations from thermal spectra in the CMB could be measured. In 1967 Sachs and Wolfe, using the fully relativistic cosmological perturbation theory, predicted that the fluctuations in the matter density and gravitational potential, both at the time of the last scattering surface $t_{\rm LSS}$, and between the LSS and observation, resulted in deviations of order 1% [38] in the temperature distribution of the CMB across the sky. With good enough precision, one could detect deviations from isotropy from the measured average temperature $T_{\rm CMB}$

$$\frac{\Delta T}{T_{\rm CMB}} \sim 10^{-5}. \tag{2.59}$$

The CMB temperature is observed as statistically homogeneous and isotropic radiation covering the whole celestial sphere $T(\mathbf{n})$ [20], and as such we are able to analyze its anisotropy angular power spectra using the procedure detailed in the previous section. At the same time, we can use cosmological perturbation theory to calculate the theoretical angular power spectrum and match it to the observed spectra.

In order to precisely calculate the CMB anisotropies one can use different formalisms, mainly using the Einstein-Boltzmann equations and numerically solving them through numerical solvers such as CAMB [39] and CLASS[40, 41], which can be directly used to test state of the art data from the Planck satellite [34].

Here we briefly follow the general relativistic geometric optics treatment in the manner of Sachs, Wolfe and Ehlers. We do not perform any explicit calculations, which all can be found in the standard text [20] for all of the mentioned formalisms and goes in depth on all the physical effects relating to the CMB radiation. We also use the Newtonian gauge (2.33) for simplicity.

Photons from the CMB follow very closely geodesics of the metric (2.21). An observer $\mathcal{O}$ comoving with the cosmic fluid with 4-velocity u^α (2.27) measures the photon in the full perturbed spacetime with 4-moment k^α and energy $E_\mathcal{O} = -u^\alpha k_\alpha|_\mathcal{O}$.

One can obtain the perturbations for the photon 4-momentum by integrating the geodesic equation

$$\nabla_k k^\mu = k^\alpha \nabla_\alpha k^\mu = 0, \tag{2.60}$$

and decomposing the tangent vector k^μ into a part parallel to the observer 4-velocity and a propagation direction part e,

$$k \cdot k = 0\,, \quad e \cdot e = 1\,, \quad u \cdot e = 0 \quad \text{with} \quad k = E(u - e)\,, \quad \text{and} \tag{2.61}$$

$$k^\mu = \bar{k}^\mu + \delta k^\mu\,, \qquad \text{with} \qquad \bar{k}^\mu = \frac{1}{a^2}(1, \bar{n}^i), \tag{2.62}$$

where $\bar{n}$ is the normalized background space direction of the source measured by the observer. We then obtain, in Newtonian Gauge,

$$\delta k^0 = \frac{1}{a^2}\delta n^0 = \frac{1}{a^2}\left[-2\Psi\Big|_{\mathcal{S}}^{\mathcal{O}} - \int_s^o d\lambda\ \left(\dot{\Psi}+\dot{\Phi}\right)\right], \tag{2.63a}$$

$$\delta k^i = \frac{1}{a^2}\delta n^i = \frac{1}{a^2}\left[2\bar{n}^i\Phi\Big|_{\mathcal{S}}^{\mathcal{O}} - \int_s^o d\lambda\ \partial^i(\Psi+\Phi)\right]. \tag{2.63b}$$

The energy measured by the observer $\mathcal{O}$ is given by

$$E_{\mathcal{O}} = -k_\mu u^\mu = \frac{1}{a_{\mathcal{O}}}\left[1+\Psi+\bar{n}^i V_i\right]_{\mathcal{O}} + \frac{1}{a_{\mathcal{O}}}\int_s^o d\lambda\ \left(\dot{\Psi}+\dot{\Phi}\right), \tag{2.64}$$

where we neglect monopole terms [20].

We are not only interested in how the full perturbed CMB temperature measured by the observer $T_{\mathcal{O}}$ is distributed across the sky, but how it scales with the change in redshift. Using the Stefan-Boltzmann law and the radiation equation of state (2.4), we have the relation $\rho_r \propto T^4$, and obtain the following scaling law for for the perturbed temperatures

$$\frac{a_{\mathcal{S}}}{a_{\mathcal{O}}} = \frac{T_{\mathcal{O}}}{T_{\mathcal{S}}} = \frac{\bar{T}_{\mathcal{O}}}{\bar{T}_{\mathcal{S}}}\left(1 - \frac{\delta T_{\mathcal{O}}}{T_{\mathcal{O}}} + \frac{\delta T_{\mathcal{S}}}{T_{\mathcal{S}}}\right) = \frac{T_{\mathcal{O}}}{T_{\mathcal{S}}}\left(1 - \frac{1}{4}\delta_r\Big|_{\mathcal{S}}^{\mathcal{O}}\right), \tag{2.65}$$

where we included the subscript $_r$ to indicate that these are radiation perturbations. By naming the observer $\mathcal{O}$ the CMB sky that we measure today $_{\text{CMB}}$ and the source as the CMB at the time of decoupling $_{\text{dec}}$, we can write, through the use of (2.64),

$$\frac{E_{\text{CMB}}}{E_{\text{dec}}} = \frac{T_{\text{CMB}}}{T_{\text{dec}}}\left[1 - \left(\frac{1}{4}D_g^{(\text{r})} + V_j^{(\text{r})}n^j + \Psi + \Phi\right)\right]_{\mathcal{S}}^{\mathcal{O}} + \int_{\mathcal{S}}^{\mathcal{O}} d\lambda\ \left(\dot{\Psi}+\dot{\Phi}\right). \tag{2.66}$$

By integrating and evaluating the previous equation at the observer and source times, and by measuring the temperature fluctuations difference from two directions $\mathbf{n} = \mathbf{n}_1 - \mathbf{n}_2$, we have the temperature fluctuation field of the CMB [20]

$$\left.\frac{\Delta T(\mathbf{n})}{T}\right|_{\text{CMB}} = \left(\frac{1}{4}D_g^{(\text{r})} + V_j^{(\text{b})}n^j + \Psi + \Phi\right)(t_{\text{dec}}, \mathbf{x}_{\text{dec}}) + \int_{\mathcal{S}}^{\mathcal{O}} d\lambda\ \left(\dot{\Psi}+\dot{\Phi}\right)(t_{\text{dec}}, \mathbf{x}_{\text{dec}}), \tag{2.67}$$

where $\mathbf{x}(t) = \mathbf{x}_0 - (t_0 - t)\mathbf{n}$, $\mathbf{x}_0$ the source position. The superscripts are used to indicate which energy content we are referring to in each term. The result also excludes the observer dipole term $V_j^{(\text{b})}n^j|_{\mathcal{O}}$, which is related to the intrinsic motion of the observer (in our case, the Earth), and is not extragalactic or cosmological in nature.

The terms in parenthesis are fluctuations intrinsic to the last scattering surface: the radiation density fluctuation and the gravitational potentials, as well as the motion of the observer in relation to the LSS.

The term $V_j n^j$ is called the Doppler contribution to the CMB anisotropy, and is due to the relative motion between the observer and the LSS.

By assuming that the initial conditions for the curvature perturbations are adiabatic, detailed in [20], and supported by the Planck satellite [34], we have the relation for the Bardeen potentials

$$\Psi = \Phi. \tag{2.68}$$

One can use Einstein's equations (2.36) to obtain the density fluctuations D_g in terms of the gravitational potentials Φ and Ψ, and under these initial conditions for the initial fluctuations one has [20] the (ordinary) Sachs-Wolfe effect

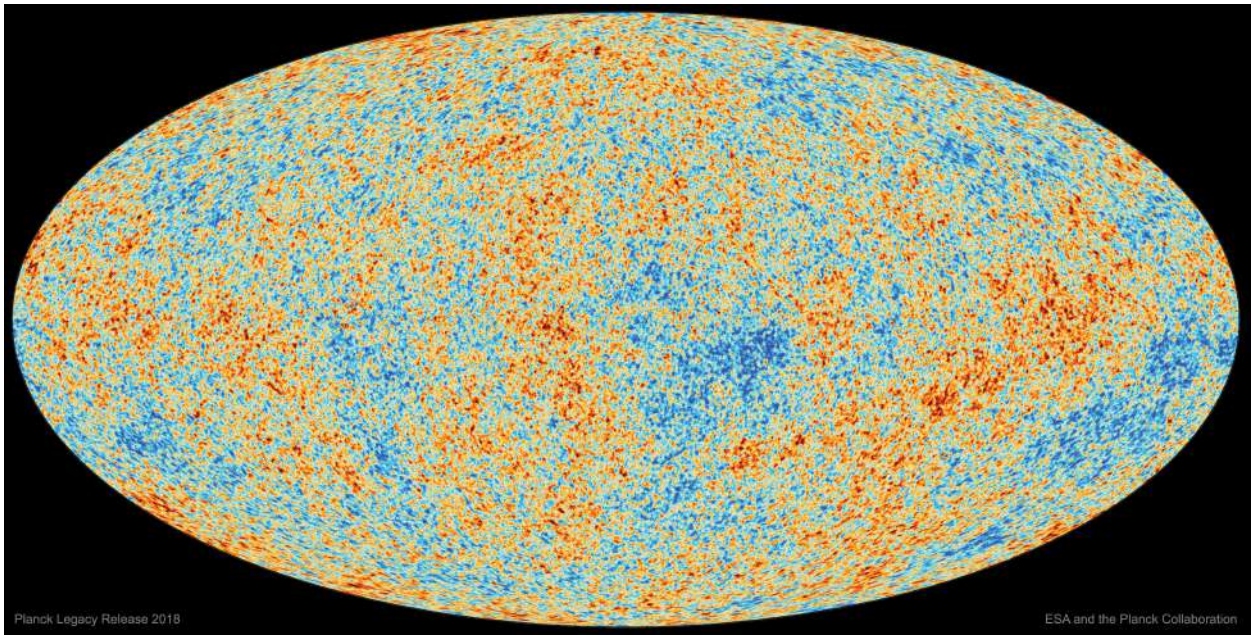

Figure 2.7.: Oberved temperature fluctuations of the Cosmic Microwave Background from the Planck satellite. In comparison to figure 2.3, one can clearly see how the improvement in detection and processing increased both precision and accuracy in detecting the fluctuations in the CMB. Taken from NASA website.

$$\left(\frac{\Delta T(\mathbf{n})}{T}\right)^{\mathrm{OSW}} = \frac{1}{3}\Psi(t_{\mathrm{dec}}, \mathbf{x}_{\mathrm{dec}}). \tag{2.69}$$

First derived in Sachs and Wolfe's paper [38], this term is related to the curvature fluctuation at the time of the last scattering surface, which is sourced by the Newtonian potentials Φ and Ψ. These are the main contributions to the fluctuations in the CMB temperature at large angular scales in the sky, and were first detected by the COBE satellite [42], a confirmation of the validity of the perturbative treatment for cosmology and its closeness to isotropy and homogeneity.

The integrated term in equation (2.67) is called the Integrated Sachs-Wolfe effect, and is the result of the integrated time variation of the gravitational potentials from the LSS to us. Its effect is seen at large angular scales, and since it is a tracer of the evolution of the gravitational potential, the best measurement of this effect is obtained through the cross-correlation of the CMB power spectrum and large scale structure fluctuations, such as described in [43].

In figure 2.7 we plot the observed temperature fluctuation field of the CMB as measured from Earth, which is in high agreement with the predictions of cosmological perturbation theory in ΛCDM.

The angular power spectrum of the CMB is obtained by using the formalism of the previous section, however one still needs two ingredients to fully describe the power spectrum: the form of the primordial power spectra, generated during the inflation-like phase of the Universe, and the transfer functions for the fields in (2.13).

We need to assume a primordial power spectrum $\mathcal{P}_\Psi$ such that the fluctuations in the fields are generated from quantum fluctuations of the curvature during the primordial Universe. It is a generic prediction of inflationary models and inflation-like models of the primordial Universe that the quantum fluctuations of the curvature are given by a spectrum of the form [44, 20]

$$k^3\langle\Psi(\mathbf{k})\Psi(\mathbf{k}')\rangle = (2\pi)^3\delta(\mathbf{k}-\mathbf{k}')\mathcal{P}_\Psi = (2\pi)^3\,\delta(\mathbf{k}-\mathbf{k}')A\left(\frac{k}{k_*}\right)^{n_s-1}, \tag{2.70}$$

where A and k_* are the characteristic amplitude and pivot scale of the spectrum, determined by observations. n_S is called the spectral index, which is determined from the primordial Universe model. Generic inflationary models predict a scale-invariant spectrum $n_S = 1$, although current observations show the spectrum to be nearly scale invariant, with a spectral index $n_s \approx 0.96$ [34].

The Bardeen potentials power spectrum P_ψ, which is the actual observed curvature power spectrum, is related to the primordial curvature fluctuations spectrum through the relations [20]

$$k^3 P_\Psi = 2\pi^2\left(\frac{3}{5}\right)^2\mathcal{P}_\Psi \tag{2.71}$$

$$A\left(\frac{k}{k_*}\right)^{n_S-1} = 2\pi^2\left(\frac{3}{5}\right)^2 A_S\left(\frac{k}{k_*}\right)^{n_S-1}, \tag{2.72}$$

where A_S is the amplitude of the scalar perturbations, the measured amplitude of the curvature power spectrum, and the factors are due to the quantum evolution of the primordial spectrum.

After the generation of the initial quantum fluctuations of curvature through inflationary dynamics, the resulting fluctuations are gaussian [44, 20], and to linear order there is a function that maps the primordial fluctuations, which are random distributions, to the matter and velocity fluctuations observed in the late Universe. These are called the transfer functions, and determine the full scale and time evolution given the initial fluctuations $\Psi(k, t_{\rm ini})$, where $t_{\rm ini}$ is the time after the inflationary dynamics. One can write

$$X(k,t) = T_X(k,t)\Psi(k,t_{\rm ini}). \tag{2.73}$$

The transfer function for a given field is determined by the physics from the post-inflation, radiation-dominated era of the Universe, and can either be found through direct integration of the Einstein-Boltzmann equations, which describes the interaction of the particle types during this era, or through an ansatz that describes the physics phenomenologically. Throughout this work, we will use the Einstein-Boltzmann solver CLASS [40, 41], a numerical, efficient Einstein-Boltzmann solver, to obtain the Transfer Functions for the late-time perturbations. For an analytical, phenomenological and accurate model of the Transfer functions for matter densities, one can check the seminal Eisenstein-Hu model in [45].

Using the perturbed Einstein equations (2.36) and the definition of the transfer function (2.73), one finds in Fourier space, for the gauge-invariant matter, velocity and potential fields [37]

$$T_\Phi = T_\Psi \quad , \tag{2.74a}$$

$$T_V = \frac{2a}{3\Omega_m}\frac{k}{\mathcal{H}_0^2}\left(\mathcal{H}T_\Psi + \dot{T}_\Psi\right) \tag{2.74b}$$

$$kT_\Psi = \dot{T}_V + \mathcal{H}T_V, \tag{2.74c}$$

$$T_D = -\frac{2a}{3\Omega_m}\left(\frac{k}{\mathcal{H}}\right)T_\Psi - 3T_\Psi - 3\frac{\mathcal{H}}{k}T_V \tag{2.74d}$$

where T_Ψ is the transfer function for the Bardeen potential, related to the primordial curvature fluctuations through (2.71).

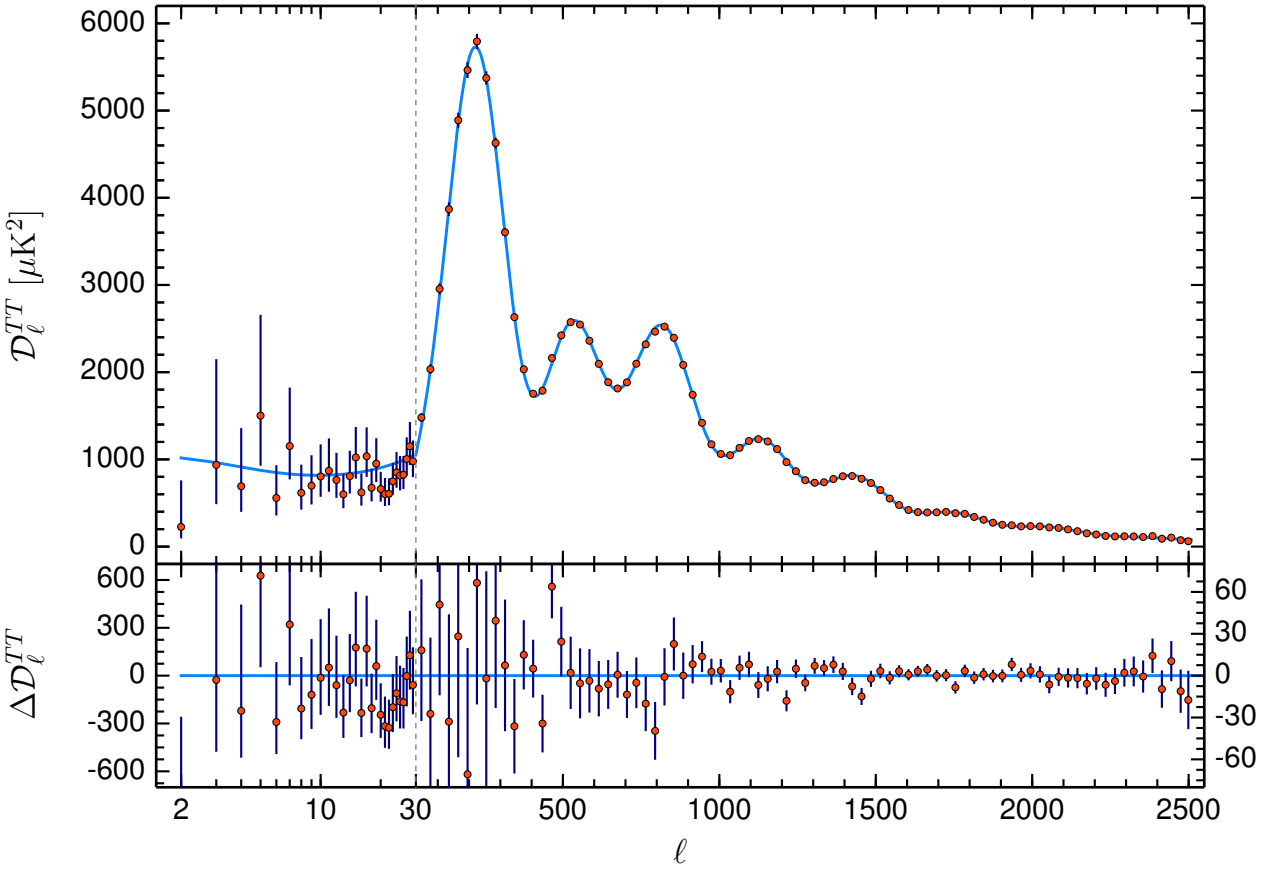

Figure 2.8.: Measured power spectrum for the CMB fluctuations, continuous line is best fit using the ΛCDM model and assuming an inflationary primordial spectrum given by (2.70).

Using equation (2.58) and substituting the terms for the initial curvature perturbations power spectra using (2.74), we finally obtain the CMB angular power spectrum

$$C_\ell^{\rm CMB} = \frac{2A}{\pi}\int \frac{dk}{k}\left(\frac{k}{k_*}\right)^{n_S-1} |F_\ell^{\Delta T/T}(k, z_s)|^2, \tag{2.75}$$

where $F_\ell^{\Delta T/T}(k)$ is the Kernel function for (2.13), which can be found in e.g. [24, 20].

In figure 2.8 we show the results from the final Planck satellite data release [34], with the data points and best theoretical fit using the ΛCDM model. The measurements of the satellite are one of the greatest successes of the ΛCDM and Big-Bang cosmology, which predict a spectrum according to the one measured by the satellite. One can find the best fits for the cosmological parameters in appendix C, which we use extensively through this thesis.

2.3.5. Cosmic Structures in the Universe and matter Power Spectrum

As mentioned previously, the observed Universe is isotropic and homogeneous only statistically. We observe structure at all scales, from galaxy super-clusters and cosmic filaments to local clusters and interacting galaxies. Like the CMB, the power spectrum of fluctuations of the distribution of galaxies and other tracers of matter in the Universe provide not only a statistical description of the observed Universe at large scales but is also able to constrain its energy content and the

underlying theory describing gravitational interactions at cosmological scales, being a probe into both our cosmological model and General Relativity itself.

In this section we provide a simple derivation of the matter power spectrum at first order, following [20] and then describe the fully relativistic theoretical galaxy number count, another successful prediction of cosmological perturbation theory, and discuss its relation to the galaxy number count power spectra. Unlike the CMB, which is always measured at redshift $z = 0$, one measures the galaxy and spectra distribution of sources at different redshifts, such that the spectra have redshift dependence. This redshift dependence is a powerful tool to understand how structures were formed and their evolution through time. We are going to use the results of this section extensively through this thesis, since our results are highly dependent on understanding of cosmic structure and how it behaves at different scales and redshifts.

Let $N(\mathbf{n}, z)$ denote the number of galaxies observed from direction $\mathbf{n}$ in the sky and at redshift z in an infinitesimal solid angle $d\Omega$. For a redshift slice $[z, z+dz]$, the average number of galaxies observed is $4\pi\bar{N}(z)f_{\text{sky}}$, where $\bar{N}$ is the average number of galaxies at this given redshift slice and f_{sky} is the fraction of the sky observed.

The galaxy number count fluctuation at redshift z is defined as the field

$$\Delta(\mathbf{n}, z) = \frac{N(\mathbf{n}, z) - \bar{N}(z)}{\bar{N}(z)}. \tag{2.76}$$

In order to map the number count fluctuations to the matter distribution in the Universe, one needs the assumption that the distribution of galaxies, or objects being counted, follows closely the distribution of CDM. It is commonly assumed that the density fluctuations in the Universe δ are related linearly to the galaxy number fluctuations Δ through the bias factor b:

$$\Delta(k, z) = b(z)\delta(k, z), \tag{2.77}$$

where we further assumed that there is no scale dependency on the bias factor b. This sympli-fying hypothesis, although prone to errors, is enough to treat the relation between dark matter and galaxies [24, 20] at first order, meaning that the uncertainties and errors are contained in the estimative for the bias factor $b(z)$. At higher orders and beyond linear perturbation theory, one cannot claim this anymore, as nonlinear, baryonic and local galactic dynamics play a major role in the bias factor, and one can find an introduction to such aspects in [24]. Since in this work we are concerned with linear perturbation theory and large scales, the hypothesis is sufficient to take into account all of the physical effects we are interested in.

Assuming the galactic bias hypothesis then, and writing the galaxy number count $N(\mathbf{n}, z)$ in terms of the density and the volume of the redshift slice V, we obtain

$$N(\mathbf{n}, z) = \bar{\rho}\bar{V}\left(1 + \delta_z + \frac{\delta V}{V}\right), \tag{2.78}$$

where δ_z is the density fluctuation at fixed redshift and δV is the volume fluctuation. The volume V of a redshift slice dz observed from a direction $-\mathbf{n}$ is given by

$$V = r^2(z)d\Omega_{\mathbf{n}}dr = r^2(z)\frac{dr}{dz}d\Omega_{\mathbf{n}}dz, \tag{2.79}$$

where $d\Omega_{\mathbf{n}}$ is the infinitesimal solid angle at direction $-\mathbf{n}$ to the source, and $r(z)$ is the comoving distance, defined by the radial integral of the line element (2.21)

By using equation (2.64) and the definition of redshift we obtain

$$(1+z)^{-1} \equiv \frac{E_{\mathcal{O}}}{E_{\mathcal{S}}} = \frac{1}{1+\bar{z}}(1-\frac{\delta z}{1+\bar{z}}) \\ = \frac{1}{1+\bar{z}}\left[(1-\Psi+\mathbf{V}\cdot\mathbf{n})\,|_{\mathcal{O}} - \int_s^o d\lambda\ \left(\dot{\Psi}+\dot{\Phi}\right)\right], \tag{2.80}$$

and by writing the derivative of the perturbed comoving distance $r = \bar{r} + \delta r$ w.r.t. the redshift z

$$\frac{dr}{dz} = \left(1-\frac{d\delta z}{d\bar{z}}\right)\frac{dr}{d\bar{z}} = \frac{1}{(1+z)\mathcal{H}}\left(1+\mathbf{V}\cdot\mathbf{n}+\frac{d(\mathbf{V}\cdot\mathbf{n})/dr}{\mathcal{H}}\right), \tag{2.81}$$

where we neglected the observer dependent monopole term $\Psi_{\mathcal{O}}$ and the small, integrated ISW-like integral in (2.64), we are able to write the volume perturbation in (2.79) as

$$\frac{\delta V}{V} = \frac{d(\mathbf{V}\cdot\mathbf{n})/dr}{\mathcal{H}}. \tag{2.82}$$

We are now finally able to write the observed galaxy number count fluctuation (2.78) in terms of the density perturbations δ

$$\Delta(\mathbf{n},z) = b(z)\delta(\mathbf{x},z) - \frac{\mathbf{n}\cdot\nabla(\mathbf{n}\cdot\mathbf{V}(\mathbf{x},z))}{\mathcal{H}}, \tag{2.83}$$

where $\mathbf{x} = -r\mathbf{n}$ is the distance from observer in the direction $\mathbf{n}$, r the comoving distance; and we used vector notation to write the spatial derivative operators $\partial_r = -\mathbf{n}\cdot\nabla$, $\mathbf{V} = \partial_i V$. The last term in the right hand side of (2.83) is called the redshift space distortion effect, a distortion in the radial redshift measurement due to the peculiar velocity of sources, which is the actual measured redshift of a source, and needs to be taken into account in surveys.

By doing a Fourier transform of (2.83) and using the continuity equation (2.37a) for the case of dust, we obtain

$$\Delta(\mathbf{k},z) = b\delta(\mathbf{k},z) - \frac{\mu^2k^2}{\mathcal{H}}V(\mathbf{k},z) = b\delta(\mathbf{k},z) - \frac{\mu^2\dot{\delta}(\mathbf{k},z)}{\mathcal{H}}. \tag{2.84}$$

This is an approximation of the number count fluctuation measured by galaxy surveys, taking into account only terms that are first order in $\mathcal{H}/k$ [20]. In this derivation we have neglected small and gauge terms, included in the full equation (2.87).

We also introduce an important function here, namely the growth function, through the definition

$$f \equiv \frac{\dot{D}}{\mathcal{H}D} = \frac{d\ln D}{d\ln a}, \tag{2.85}$$

where D is the growing mode of density perturbations obtained from equations (2.43) and (2.37). In the dust dominated era of the Universe, the growing modes D do not depend on the wavenumber k [20], such that we may write $\delta(k,z) = \delta(0,k)D(z)$, where $\delta(0,k)$ are the perturbations normalized such that $D(0) = 1$. The growth function is a measure of the Universe's growth rate, taking into account the growth per fluctuation amount.

Using (2.50) and the definition of the growth function in (2.84) we find

$$P_\Delta(k,z) = P_\delta(k,z)[b+\mu^2 f], \tag{2.86}$$

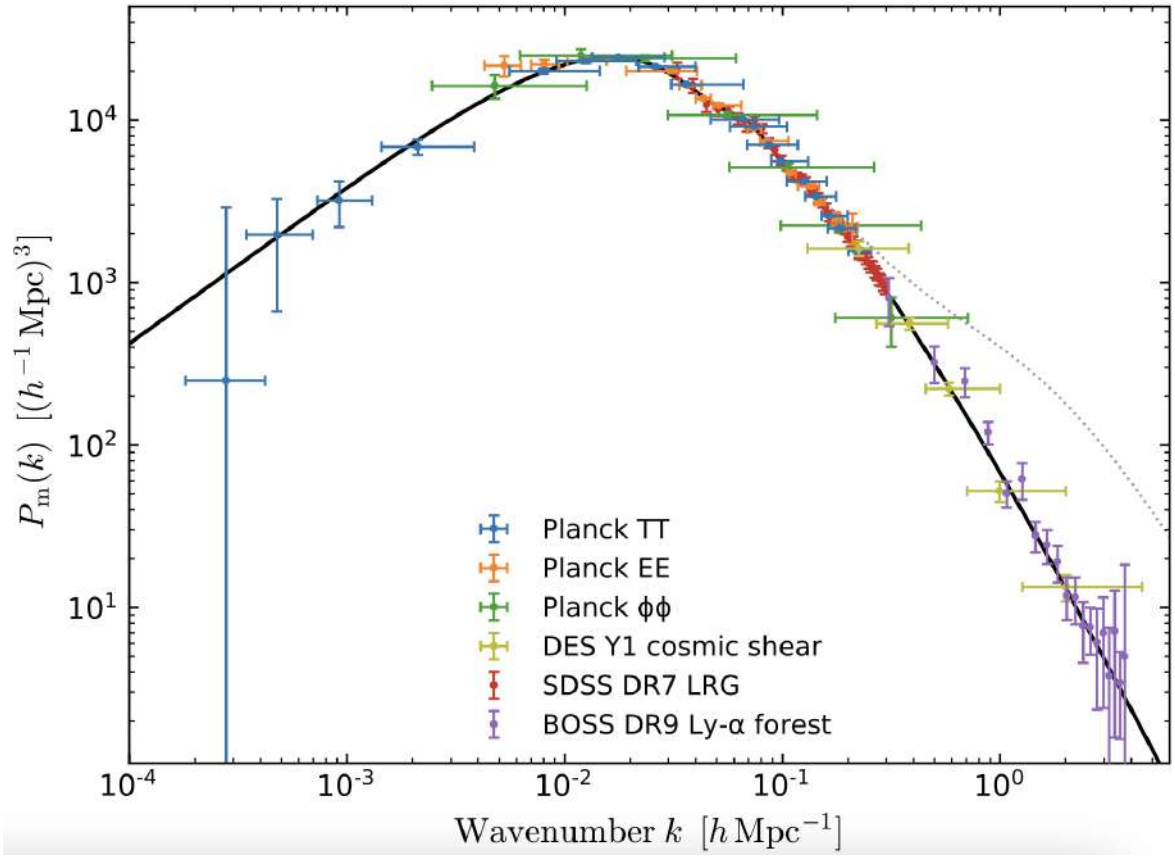

Figure 2.9.: Normalized growth function $f\sigma_8$ best fit for the ΛCDM model using data from Planck satellite and including measurements from large scale structure surveys. Taken from [48].

which directly relates the observed galaxy number count spectrum to the theoretical matter power spectrum. By observing galaxy number count fluctuations and calculating its power spectra (2.86), one is able to constrain the growth function $f(z)$ and test the cosmological model, since the growth of perturbations is dictated by the evolution equations (2.36, 2.37) and these are model dependent.

Both the growth function and the matter power spectra at different redshifts have been measured, and they are in accordance with the CMB measurements of both primordial and late-time perturbations [24, 20, 43, 34, 46, 47]. This is another success of the ΛCDM model, which is able to correctly describe cosmological physics in the redshift range $z \in [0, 1100]$. In figure 2.9 we show the best-fit for the ΛCDM model for the matter power spectrum using the Planck 2018 release data, and including measurements from other large scale structure surveys; and in figure 2.10 we show the best fit for the normalized growth function $f\sigma_8$ for ΛCDM also from [48].

Although equation (2.86) is a good approximation for the observed galaxy number count fluctuations and extensively used in the literature to model the spectra, it could be derived using strictly Newtonian perturbation theory. One can derive the fully relativistic galaxy number count using cosmological perturbation theory, taking into account all of the gauge and gravitational potential effect. This was first done in [49, 37], where its angular and linear power spectra were calculated as well. Here we write the full result, since we shall make use of it further in the thesis, without the derivation, which is quite involved.

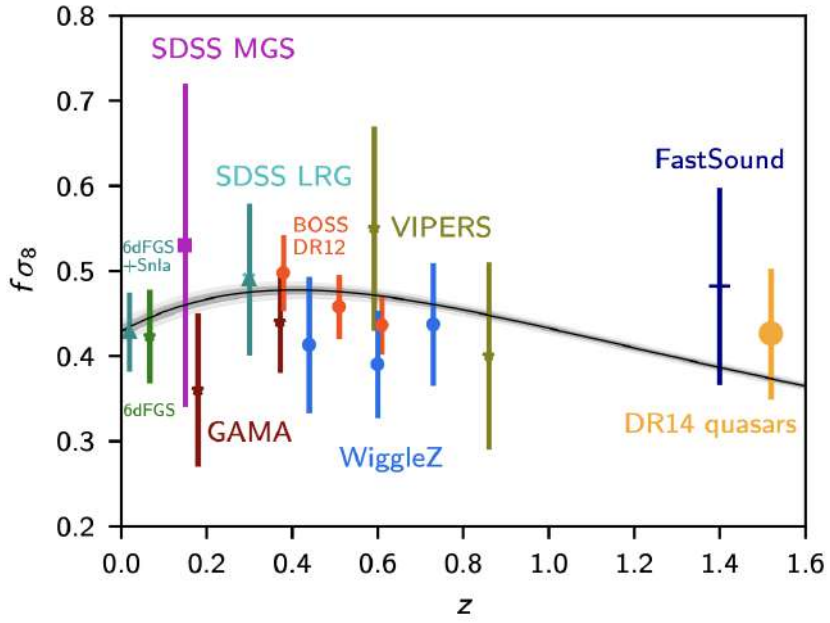

Figure 2.10.: Matter power spectrum amplitude at $z = 0$ best fit for the ΛCDM model using data from Planck satellite and including measurements from large scale structure surveys. Taken from [48].

The fully relativistic galaxy number count fluctuation is given in gauge-invariant form by

$$\Delta(\mathbf{n}, z) = D_g + \Phi + \Psi + \frac{1}{\mathcal{H}}\left[\dot{\Phi} + \partial_r(\mathbf{V}\cdot\mathbf{n})\right] + \left(\frac{\dot{\mathcal{H}}}{\mathcal{H}^2} + \frac{2}{r_{\mathcal{S}}\mathcal{H}}\right)\left(\Psi + \mathbf{V}\cdot\mathbf{n} + \int_{\mathcal{S}}^{\mathcal{O}} d\lambda\ \left(\dot{\Psi} + \dot{\Phi}\right)\right)$$
$$+ \frac{1}{r_{\mathcal{S}}}\int_{\mathcal{S}}^{\mathcal{O}} d\lambda \left(2 - \frac{r_{\mathcal{S}} - r}{r}\Delta_\Omega\right)(\Psi + \Phi)\,, \tag{2.87}$$

where Δ_Ω is the angular part of the spatial Laplacian, and $r_{\mathcal{S}}$ is the comoving distance to the source.

Its power spectrum is given by

$$C_\ell^N(z_s) = \frac{2A_S}{\pi}\int \frac{dk}{k}(kt_O)^{n-1}\left|F_\ell^N(k, z_s)\right|^2, \tag{2.88}$$

where the kernels are given by

$$F_\ell^N(k, z_s) = \ j_\ell(kr_s)\left[T_D + \left(1 + \frac{\dot{\mathcal{H}}}{\mathcal{H}^2} + \frac{2}{r_s\mathcal{H}}\right)T_\Psi + T_\Phi + \frac{1}{\mathcal{H}}\dot{T}_\Phi\right] + j'_\ell(kr_s)\left(\frac{\dot{\mathcal{H}}}{\mathcal{H}^2} + \frac{2}{r_s\mathcal{H}}\right)T_V + \frac{k}{\mathcal{H}}T_V j''_\ell(kr_s)$$
$$+ \frac{1}{r_s}\int_0^{r_s} j_\ell(k\lambda)\left(2 + \frac{r_s - \lambda}{\lambda}\ell(\ell+1)\right)(T_\Psi + T_\Phi)d\lambda + \left(\frac{\dot{\mathcal{H}}}{\mathcal{H}^2} + \frac{2}{r_s\mathcal{H}}\right)\int_0^{r_s} j_\ell(k\lambda)(\dot{T}_\Psi + \dot{T}_\Phi)d\lambda. \tag{2.89}$$

It is useful to restrict the predicted power spectra (2.50, 2.54) to a certain range of redshifts z and/or a certain range of scales k, since most surveys do not observe all of the night sky and

redshifts are sliced in discrete bins [20, 24]. In order to do so, one introduces a Window Function in the equation for the power spectra using the relation

$$\int d^3y W(\mathbf{x}-\mathbf{y})\delta(\mathbf{y}) = \int \frac{d^3k}{(2\pi)^3} e^{i\mathbf{k}\cdot\mathbf{x}} W(k)\delta(k), \tag{2.90}$$

where $W(\mathbf{x}-\mathbf{y})$ is a function that selects a given scale. The trivial example would be the Dirac delta $W = \delta(\mathbf{x}-\mathbf{x_0})$, which filters any measurement other than at the point $\mathbf{x_0}$. In galaxy surveys it is common to use the Gaussian and the top-hat window functions [20], given by a normalized Gaussian distribution around a redshift z_0:

$$W(z) = \frac{1}{\sqrt{2\pi}\sigma(z)} \exp\left(-\frac{1}{2}\left(\frac{z-z_0}{\sigma(z)}\right)^2\right), \tag{2.91}$$

where $\sigma(z)$ is the variance at redshift z.

By using a window function that filters out scales larger than a given R in (2.50) for the matter power spectrum, one finds an important relation between the matter power spectrum at redshift $z = 0$ and the amplitude of the variation of matter density fluctuations inside a region of radius R [24]

$$\langle \Delta^2 \rangle = \sigma_R^2 = \int \frac{d^3k}{(2\pi)^3} |W_R(k)|^2 P_\Delta(k), \tag{2.92}$$

where we used (2.91) in the definition of the Power Spectrum. As the amplitude of the variance of number counts, and therefore of matter perturbations, the σ^2 measures the deviation from the average density of the Universe at different scales R. For small enough scales, σ^2 grows, as one should expect, since the cosmological principle dictates homogeneity only on large enough scales. Therefore, one should expect that there is a scale where fluctuations become too large to be dealt with perturbatively, using linear perturbation theory [24]. In the literature, it is common to set $R = 8\,\mathrm{M}pc$, such that by measuring σ_8^2 one is able to measure the amplitude of matter perturbations today and compare it to the observed fluctuations at higher redshifts. The value of σ_8 obtained from the Planck collaboration results is shown in appendix C.

2.3.6. What is Λ?

As we have seen, the ΛCDM is successful in making theoretical predictions at many different scales and redshift ranges, such that the discovery of the current accelerated phase of the Universe's expansion is corroborated not only at the background level but also from the observation of cosmic structures and the CMB.

As of 2024, the ΛCDM is still the concordance model of cosmology, although some observations and measurements could point to a tension in its predicted H_0 and σ_8 values derived from the CMB and late-time observations, described and reviewed in [50, 51, 52, 53]. A more fundamental issue however, is that of the nature of the Λ term in Einstein's equations.

The hypothesis of Λ is one that relies on other assumptions of the concordance cosmological model, such as the cosmological principle and that the underlying field theory of gravitational dynamics is General Relativity. If we assume that the value of Λ is the resting energy of the vacuum from all the particle fields coupled to gravity, then this values differs from the vacuum of the Standard Model by more than 60 orders of magniude [54].

Could this discrepancy be an indication of quantum gravity effects, such that for a consistent theory, that extends the gravitational action to the ultraviolet, the couplings to the standard

model give the correct value for the vacuum energy? If we assume that the cosmological constant is actually an energy component of Einstein's equations, then how should we model it? Is it the effect of a dynamical scalar field? Why are humans able to measure the effect of the acceleration of the Universe at the present epoch? [55]

If we leave the cosmological principle behind, it could be that the measured acceleration is in fact an observer dependent effect due to the incorrect assumption that the Universe is homogeneous and isotropic but the actual metric describing cosmological dynamics is inhomogeneous and/or anisotropic [56, 57].

It could also be the case that General Relativity is not the best theory to describe gravitational dynamics at cosmological scales. There could be additional terms or interactions in the gravitational Lagrangian such that the field equations (2.1) themselves should be modified. The standard review for classical modifications of General Relativity, their phenomenology and consequences in cosmology is [58].

One of the main undertakings of modern cosmology is to test the ΛCDM model to its full extension, at ever smaller scales and higher redshifts, where General Relativity and the cosmological principle have not been tested yet. In order to do so, new cosmological probes and quantities, some predicted theoretically decades ago but only made testable in the current precision era of cosmology and state-of-art spectroscopes and satellites [59, 60].

The subject of this thesis, the cosmological redshift drift and its fluctuations, promises to be a probe into the late-time accelerated era of the Universe, able to test the ΛCDM prediction of a current accelerating Universe without assumptions on an underlying metric or energy content of the Universe, being a direct measure of the rate of change of the redshift (2.11). In the next chapter we will review the definition of the redshift in cosmology, its phenomenology and current perspectives on its observation and measurement, as wel as its most promising detection using the so called Sandage-Loeb test. In order to present the results of this work, we also develop the mathematical formalism needed to describe the redshift drift in arbitrary spacetimes.

The Redshift Drift

In 1962, Sandage and McVittie [6, 7] predicted that the redshift of a source's spectra in Robertson-Walker spacetimes (2.2) would generically exhibit time variation due to the expansion or contraction of the cosmological model.

Explicitly, using the definition of the redshift (2.11), we have, for a small cosmic time interval $\Delta\tau$

$$\frac{\Delta z}{\Delta\tau} = \frac{\Delta}{\Delta\tau}\left(\frac{a(\tau_{\mathcal{O}})}{a(\tau_{\mathcal{S}})} - 1\right) = \frac{1}{a(\tau_{\mathcal{S}})}\left(\frac{\Delta a(\tau_{\mathcal{O}})}{\Delta\tau} - \frac{a(\tau_{\mathcal{O}})}{a(\tau_{\mathcal{S}})}\frac{\Delta a(\tau_{\mathcal{S}})}{\Delta\tau}\right) = H_{\mathcal{O}}(1+z) - H_{\mathcal{S}}, \tag{3.1}$$

where we've used the definition of the Hubble parameter in the last equal sign (2.6). Assuming vacuum cosmologies dominated purely by curvature, Sandage calculated that the drift effect, at present cosmic time $\tau_{\mathcal{O}}$, would be of order 10^{-6}km/s yr for a spectra cz at redshift $z = 0.4$, where is c the speed of light and assuming $H_0^{-1} = 13 \cdot 10^9$yr, $c = 3 \cdot 10^5$km/s for either flat, de-Sitter or Anti-de Sitter cosmologies, a very accurate prediction for the time, since the H_0 value is close to the concordance one presently. McVittie extended Sandage's analysis, in an appendix to Sandage's paper, to cosmologies with a dust energy component, and obtained similar results for the magnitude of the effect.

This effect, called the redshift drift, is the main theme of this thesis. Its behavior in cosmological models beyond homogeneity and isotropy; how to extend the effect to arbitrary spacetimes; its detectability and importance as a cosmological probe will be studied and analyzed in this chapter, where we will also lay the mathematical basis for the main results of the thesis in the next chapters.

First, we describe the overall behavior of the redshift drift in Robertson Walker cosmologies with distinct energy contents, where the Friedmann equation is given by (2.15). We show how its sign is directly related to the current dominating energy content of the Universe.

After that, we introduce the Sandage test, the main observational proposal to detect the redshift drift in the next few decades, first introduced by Abraham Loeb [61]. We then review the developments and proposals in detecting the redshift in the past 3 decades, discuss its planned measurement through state of the art spectrographs and radio surveys, as well as synergy with other established cosmological tests.

In the last section, we review in detail the modern mathematical formalism that allows us to describe the redshift drift effect in general spacetimes, and apply this formalism to the LTB and Bianchi cosmologies, exact inhomogeneous and anisotropic cosmological spacetimes. This formalism forms the basis of the main result of this thesis: the description of the redshift drift in the ΛCDM model with structures, and its power spectra.

3.1. Redshift Drift in dynamical cosmologies and ΛCDM

We start with the FLRW metric (2.2) and arbitrary energy content such that the Friedmann equations are given by (2.15). From expression (3.1) one can notice that the redshift drift value is positive if and only if $H(z_2) < (1+z_2)H(z_1)$. A quick calculation using (2.15) gives us the redshift dependence of the Hubble parameter for Universes with only one energy component

$$\begin{aligned} H(z) &= H_0(1+z)^{3/2}, && \text{matter,} \\ H(z) &= H_0(1+z), && \text{curvature,} \\ H(z) &= H_0(1+z)^2, && \text{radiation,} \\ H(z) &= H_0, && \text{cosmological constant,} \end{aligned} \tag{3.2}$$

such that the Hubble parameter increases with redshift, and in a Universe dominated purely by matter or radiation one cannot have a positive value for the redshift drift. Extending this to arbitrary equations of state, and using (3.2) in (3.1), it is clear that for all cosmologies not including a cosmological constant we have for the redshift drift $\dot{z}$

$$\dot{z} = H_0(1+z) - H(z) \leq H_0(1+z) - H_0(1+z) = 0, \qquad \Omega_\Lambda = 0, \tag{3.3}$$

such that one cannot have a positive value for $\dot{z}$ unless $\Omega_\Lambda > 0$ or any kind of energy component violating the weak energy condition, i.e. $w < -1/3$. In the case of a flat Universe, or at late times, the only component satisfying such constraint is a dark energy-like component

We are lead to the conclusion that a positive measurement of the redshift drift in ΛCDM can only be due to a cosmological constant component Ω_Λ. In fact, the measurement of a positive value for the redshift drift in a flat or nearly flat Robertson-Walker cosmology is a model-independent way to test the existence of a cosmological constant or dark energy component in the Universe [1]. We plot this behavior in figure 3.1 for different values of the density parameters, where one can clearly see the relation between a positive value of $\dot{z}$ and the density parameter Ω_Λ. Since we observe from the CMB a flat or very close to flat Universe [34], we can safely neglect both the curvature and radiation components at late times.

Thus measuring the value of the redshift drift at the redshift ranges where we predict a dominance of the dark energy component of the Universe Ω_Λ from other cosmological probes is a test of the Λ hypothesis. In fact, as we shall see later, recent work points to the redshift drift being a metric independent probe of Dark Energy and violations of the Strong Energy condition [9].

In fact, one can use the redshift drift to test the acceleration of the Universe without assuming any hypothesis on its energy content or Einstein's equations. We can use cosmography, a parametrization of the Taylor expansion of the expression for the redshift around $z = 0$ [62], and truncate to 4-th order to obtain

$$a(t) = \left[1 + H_0(t-t_0) - \frac{1}{2}q_0H_0^2(t-t_0)^2 + \frac{1}{3!}j_0H_0^3(t-t_0)^3 + \mathcal{O}(t-t_0)^4\right], \tag{3.4}$$

$$q(t) = -\frac{\ddot{a}(t)}{a(t)}\left(\frac{\dot{a}(t)}{a(t)}\right)^{-2}, \quad j(t) = \frac{\dddot{a}(t)}{a(t)}\left(\frac{\dot{a}(t)}{a(t)}\right)^{-3}, \tag{3.5}$$

[1] We shall refer to any extension or modification of General Relativity and ΛCDM cosmology that modifies or makes the Ω_Λ equation of state dynamical as Dark Energy.

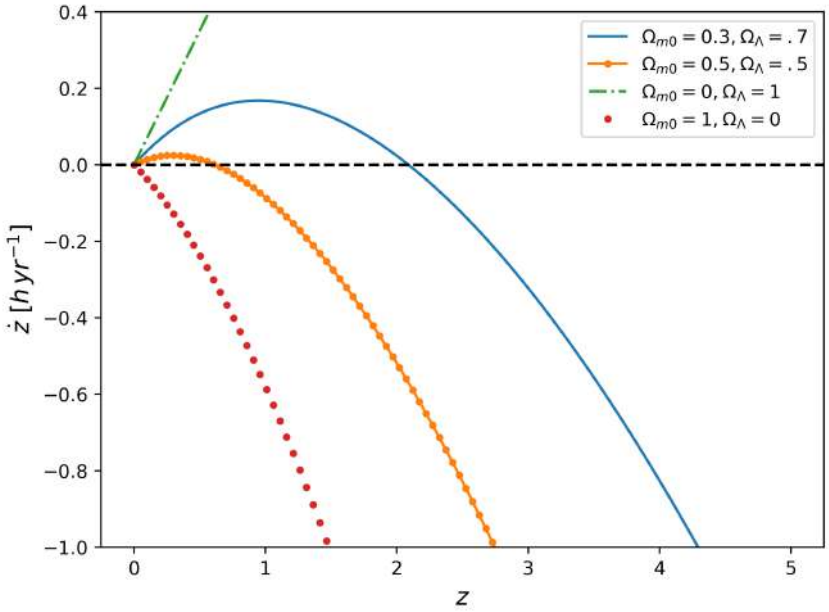

Figure 3.1.: The redshift drift $\dot{z}$ as a function of the redshift z for different cosmologies. The drift is given in units of Hubble parameter per year.

where $q(t)$ and $j(t)$ are the deceleration and jerk parameters, measuring the adimensional second and third derivatives of the Universe's expansion, and the underscore $_0$ indicates a value at $z = 0$. This parametrization has been used extensively as a way to test the cosmological expansion history without relying on assumptions on its energy content, and the negative sign before q_0 is a historical convention. In the 1998 paper by Riess [28] a negative value for the deceleration parameter was observed, indicating a Universe that is accelerating. To this day, the main method of obtaining a model-independent value for the Hubble parameter H_0 is through the distance ladder method, which relies only on geometry, meaning the scale factor $a(t)$, and the physical distance to distant sources through parallax. A review and discussion of this method can be found in [50].

The distance ladder is not a direct measurement of cosmic deceleration, as it relies on distance measurements. A direct measurement could be made through the observation of a source's redshift drift, as per equation (3.1) one can see that the drift is directly related to the Hubble parameter difference at different redshifts, and thus of its rate of change, giving us the second derivative in the cosmographic expansion, the q_0 parameter [63].

Using that $1 + z = 1/a(t)$ and $\dot{z} = -\dot{a}/a^2$ in (3.4) and truncating at second order, we obtain the relation for small redshifts at first order

$$\dot{z} = H_0^2 q_0 (t - t_0) = -H_0 q_0 z. \tag{3.6}$$

From the above equation we see that once we have a local measurement of the Hubble constant H_0, measuring the redshift drift means directly measuring the deceleration parameter, which in our notation is defined negatively, and since $t < t_0$, a positive sign for the redshift drift directly implies a positive acceleration for the expansion history $a(t)$ of the Universe at low redshifts, without any assumption on its energy content.

After the detection of the accelerated expansion of the Universe described in the second section

of chapter 2, Loeb [61] noted that by measuring the direct spectroscopic rate of change of the velocity of a source, given by

$$\delta v_{\mathcal{S}} = c\frac{\delta z}{1+z_{\mathcal{S}}}, \tag{3.7}$$

one could obtain an independent measurement of H_0 and q_0, without relying on distance measurements, which have to be calibrated and involves numerous systematics [50, 61], or the CMB, which relies on a cosmological model (in our case ΛCDM) in order to constrain the value of local cosmological parameters. In the context of current cosmological tensions, independent measurements the Hubble constant could both alleviate such tensions or provide convergence on a certain value, potentially contributing to the discovery of new physics [50, 53, 51]. Nonetheless, one could use the positivity of the signal as a null hypothesis test for the late-time acceleration of the Universe.

Since the velocity direction of sources is randomly distributed in the sky [61, 10], by averaging over sources one could in principle obtain the value for the redshift drift, which, being of cosmic origin, should be isotropically distributed [61].

Loeb's work [61] is the basis of the current observational programme to measure the redshift drift for the first time, and also the first work to note the fact that one can use the redshift drift to measure the acceleration of the Universe's expansion in an independent way. In the next section we shall describe in detail the Sandage-Loeb[2] and other observational proposals to measure the redshift drift, as well as discuss the possible facilities and instruments that could measure the drift in the near future.

3.2. Redshift Drift Detection and Observation

The possibility of using the redshift drift to constrain cosmological parameters and its observational merits were first investigated in a short paper by Lake [64], and the first full observational proposal to detect the effect was introduced by Loeb [61]. Loeb's proposal, also called the Sandage-Loeb test, is the basis for the current observational programme to first measure the redshift drift at high and low redshifts, using next-generation spectrographs already in construction, such as the one in the SKAO survey and the ANDES spectrograph at the ELT [65, 66, 67]. We detail this proposal and the current literature in such a direction, strongly influenced by the seminal paper by Liske et al [68].

3.2.1. The Sandage-Loeb test

A direct measurement of the redshift drift of a source given by (3.1) needs that one measures its spectroscopic velocity variation Δv in a cosmic time interval $\Delta\tau$. By writing the expression for the velocity variation explicitly, using in (3.7) the definition of the redshift drift and the Hubble parameter (3.2), one obtains

$$\Delta v = (cH_0\Delta\tau)\left(1-\frac{H(z)}{H_0(1+z)}\right), \tag{3.8}$$

[2] In the literature it is common to call the measurement of the redshift drift through extensive observation of sources on a given timescale the Sandage test[3], whereas the Sandage-Loeb test is used in relation to observations of the Lyman-α forest. We shall focus majorly on the Sandage-Loeb test, such that we won't make such distinction in this thesis.

and we are able to estimate the expected value of the velocity fluctuation of a source's spectra at a given redshift $z_{\mathcal{S}}$, given the cosmological densities of matter, Λ and the Hubble constant H_0. Using an H_0 value of 70km/s/Mpc, the effect is of order 10^{-3}km/s yr, 3 orders of magnitude smaller than the spectroscopic velocities due to the Hubble flow of distant objects.

A naive estimate for contaminating effects due to the local gravitational potential ϕ of sources and their peculiar accelerations and velocities a_{pec} and δv, done by Loeb using (3.8), shows that peculiar velocities contribute to a small $\delta v/c$ correction to the redshift drift, quite smaller than the cosmological term $H_0 c$; for peculiar accelerations, which are related to the potential via $a_{\text{pec}} \sim \psi/L$, with L a characteristic scale of the galaxy or cluster, only virialized, very dense localized environments, of order $\delta \sim 10^4$ of the average density can contribute to the effect, due to the observed average density of virialized structures [61]. These estimates can be made precise using cosmological perturbation theory, one of the main results of this work [10].

The Sandage-Loeb test, devised in [61], consists of observing the spectroscopic velocity variation (3.8) of a certain set of bright or well-resolved sources over a significant amount of observational time $\Delta\tau \gtrsim 10^2$yrs. Loeb used the then state of the art HIRES spectroscograph at the Keck telescope [69] (not to be confused with the currently under construction HIRES spectrograph at the ELT) and the above estimates of contaminating effects on the signal to study the feasability of observing the drift using three kinds of astrophysical sources

- The Lyman-α absorption line of the continuum flux of QSOs, which have a narrow width and are abundant up to very high redshifts. At the time, $\sim 10^2$ quasars with observable Ly-α forests could be observed from ground telescopes, and using the HIRES pixel resolution of 2km/s per pixel and a 10% flux fluctuation per pixel of the Lyα flux, Loeb estimated that one could detect the drift signal within 1σ in the timespan of a century $\Delta\tau = 10^3$yr by observing tens of quasars, and of a decade by observing $\sim 10^2$ quasars.

- Galaxies, which are much more abundant than quasars, and have a very stable cumulative spectra. Since galaxies are on average two orders of magnitude fainter than quasars, one would need a greater experiment time $\Delta\tau \sim 10^4$yr in order to compensate for the harder to resolve spectrum. Although unpractical on human timescales, the spectra of galaxies lensed by clusters have a time-delay of the order of $\Delta\tau \sim 10^2 - 10^3 yr$, such that one could, in principle, compare the spectra of the observed lensed images in order to constrain Δv.

- Absorption lines with sharp spectral features, such that one doesn't need as much resolution in observing the spectra as in the Lyα case, such as the HI lines, further investigated by Liske et al [68].

In the context of spectroscopy, systematics related to redshift precision are also involved, namely redshift binning and sensitivity, such that advancements in spectroscope technology and redshift surveys can drastically improve both the timescale and the number of objects needed in order to detect the drift.

From the first estimates obtained by Loeb, Liske et al [68] expanded on prospective candidates for sources, listing five characteristics that ideal candidates for the Sandage-Loeb test should possess:

1. **Trace the Hubble flow.**

   Candidate sources should follow the Hubble flow as closely as possible, such that peculiar motions are small compared to the cosmological contribution to the spectroscopic velocity. The orientation of peculiar motion should vanish when observing a significant range of sources, though the effect could still contaminate the observation.

2. **Have the sharpest possible spectral features.** A spectrum with sharp features, as mentioned before, makes it easier to determine the redshift of the source, which is already difficult due to systematic effects.

3. **A target should have as many spectral features as possible.**

   By extracting the maximum amount of spectral information from a single source, one needs less observational time in order to constrain the drift.

4. **Targets should be as bright as possible.**

   Bright targets are easier to resolve and need less observation time for detection of spectral features.

5. **Sources should be distributed over a wide range of redshifts.**

   From figure 3.1 one sees that in ΛCDM the drift effect has a magnitude that increases with redshift. Thus higher redshifts could provide greater detectability, and observing the effect in the $z \in [0, 2]$ range could clearly demonstrate a change of signal in the effect, characteristic of an accelerated phase.

It is impossible for an object to fulfill every criteria as, for instance, 1. and 3. are in conflict since sharp spectral features are most commonly present in high density environments, delving into nonlinear structures [24, 68] that do not follow the Hubble flow closely. The authors, however, arrived, as Loeb, at the conclusion the Lyα absorpotion line of distant quasars are the best possible candidates, since they do not fit only one of the criteria, although their spectral lines are not particularly sharp, being of order 10^3km/s, something also noted in Loeb's work [61, 68]. Quasars closely follow the Hubble flow and their Lyα absorpotion line, due to intergalactic HI, are not connected to the local environment of the quasar. This means that our source is virialized, its spectra has sharp features; it follows the Hubble flow; it has abundant sharp features in its spectra, such as metal and molecular absorption lines; and they have been observed up to $z \sim 7.6$, with a wide range of $z \in [2, 7.6]$.

In order to obtain first estimates for the peculiar motion contaminating effects, the authors derived peculiar velocity and acceleration distributions from Gadget-2 hydrodynamical simulations [70] through random line of sight at different redshifts. The authors then obtained an error due to peculiar motions of order 10^{-3}cm/s, 4 orders of magnitude smaller than the drift signal, assuming a decade-long experiment with 1cm/s accuracy and $\sim 10^2$ absorption lines [68]. We plot the results in figure 3.2 for the peculiar motion, which provided a first numerical estimate of contaminating effects for the Sandage-Loeb test. One of the results of this thesis is obtaining these estimates from first principles, as done in [10].

To model a future measurement of the drift, Loeb et al simulated the spectral lines of Lyα observers through MC random sampling of a normalized spectrum distribution, detailed in section 4 of the paper [61]. To generate the simulated drift, the authors redshifted the obtained lines using $z = 3$, assuming an experiment time of time $\Delta\tau_0 = 10$yrs and using formula (3.1) in the ΛCDM case, with cosmological parameters $H_0 = 70$km/s/Mpc, $\Omega_\Lambda = 0.7$ and $\Omega_m = 0.3$. The result is the subtraction of the two spectras. We plot the resulting drift for a single simulated Lyα forest in figure 3.3, as shown in the original paper.

It is clearly seen that the drift is highly sensitive to Ω_m, and in the corcondance model of $\Omega_m = 0.3$, $\Omega_\Lambda = 0.7$ one finds a smaller absolute value for the drift. This can be also seen purely from the theoretical equation for the drift, as one can check the absolute values for the drift in different cosmologies in figure 3.3.

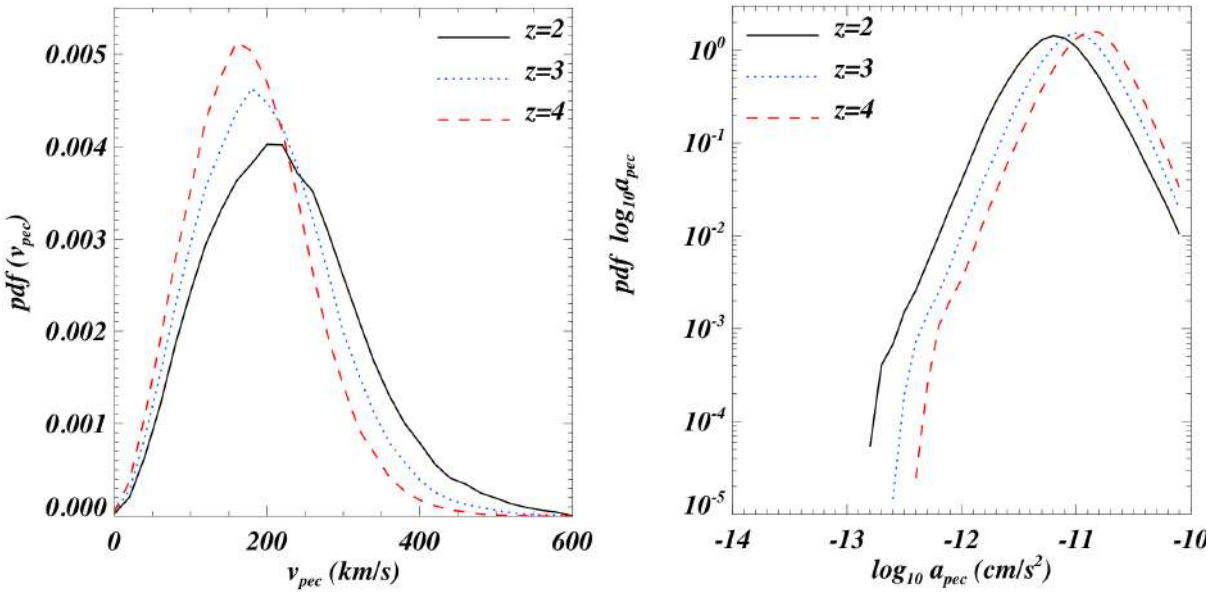

Figure 3.2.: Peculiar velocity and acceleration probability distribution function of the absorbing intergalactic gas for different redshifts using the hydrodynamical simulation described in [68]. The contaminating effects increase with redshift, with increasing peaks, but become more concentrated around a single value.

An important result obtained from the simulated spectra and drift in [68] is a phenomenological estimate on the uncertainty σ_v in the spectrosopic velocity drift for the Sandage-Loeb test, given the QSO's redshift $z_{\rm QSO}$, number of observed objects $N_{\rm QSO}$, and the experiment signal to noise ratio S/N, given by

$$\sigma_v = 2\left(\frac{S/N}{2370}\right)^{-1}\left(\frac{N_{\rm QSO}}{30}\right)^{-1/2}\left(\frac{(1+z_{\rm QSO})}{5}\right)^{-1.7}. \tag{3.9}$$

The details of the derivation can be found in the original paper and we shall omit them here. This uncertainty has been used to model baseline estimates on current experiments [65, 59, 71, 72, 73] and has been expanded upon in [71]. We plot the resulting curve and the results from both simulated and real spectra in figure 3.4, taken from [68].

The work done by Liske et al established the feasibility of detecting the redshift (or velocity) drift with then next-gen facilities, in particular the Extremely Large Telsecope, which, as of 2024, is under construction and slated for first light in 2028. It also provided a basis for future observational proposals in spectroscopy to detect the redshift drift. In this section we focus on the ELT, which has as one of its main objectives a first detection of the drift through spectroscopy [74], and SKAO, which can provide a detection of the redshift drift at a different redshift range, providing synergy with the ELT measurements [67, 65]. For the interested reader, extensions of the fundamental analysis done in [68] to other spectroscropic probes and experiments, such as 21cm lines and the CHIME survey, can be found in [71, 75, 66, 76, 77] and references therein.

While the ELT is expected to observe the drift at higher redshifts $z \gtrsim 2$, the SKA radio survey will observe the Universe at smaller redshifts $z \lesssim 1$. The SKA is a next-gen radio survey currently under construction expected to take radio astronomy and cosmology to new precision standards [78, 79], observing structure formation and astrophysical phenomena at high redshift and smaller scales.

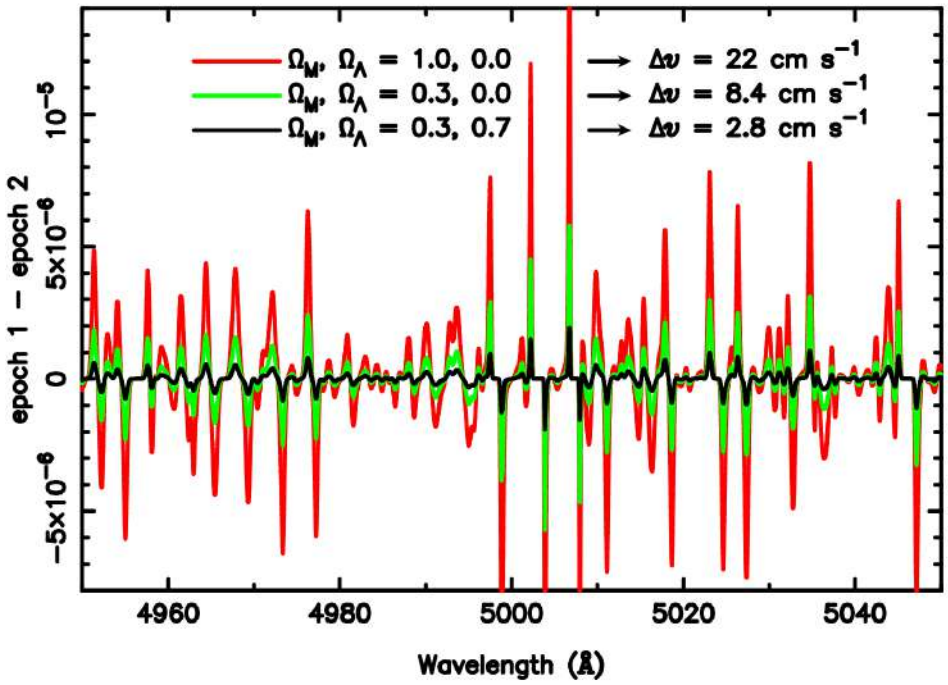

Figure 3.3.: Velocity drift (3.8) obtained through a simulated Lyα spectrum and its drift variation according to (3.7). Taken from [68].

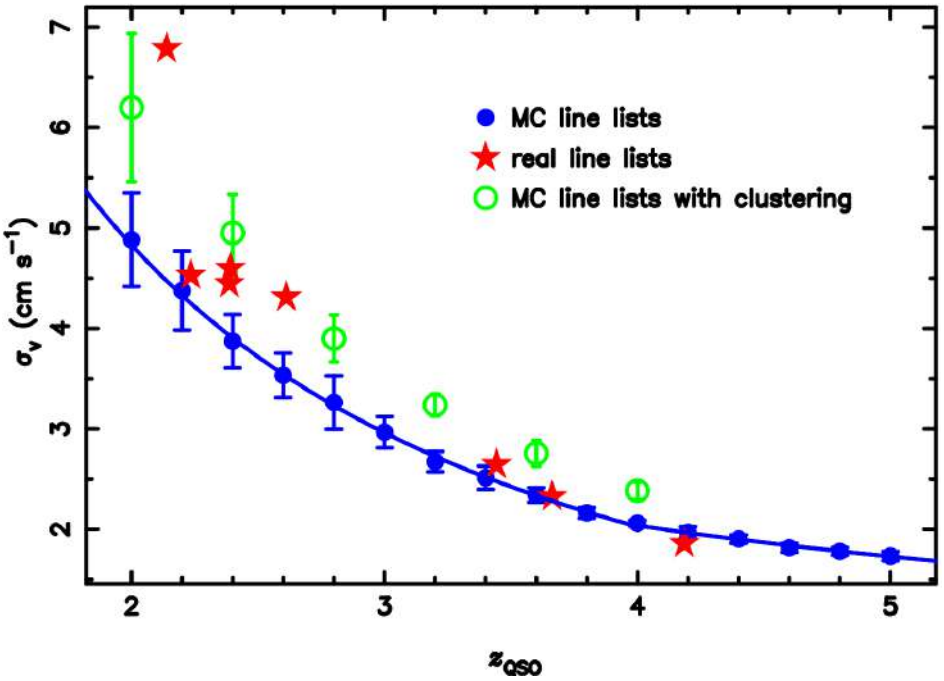

Figure 3.4.: Velocity drift uncertainty σ_v fit from (3.9). Stars are spectroscopic velocity uncertainties obtained from observed Lyα forests, while the blue and green circles are simulated spectras. Taken from [68].

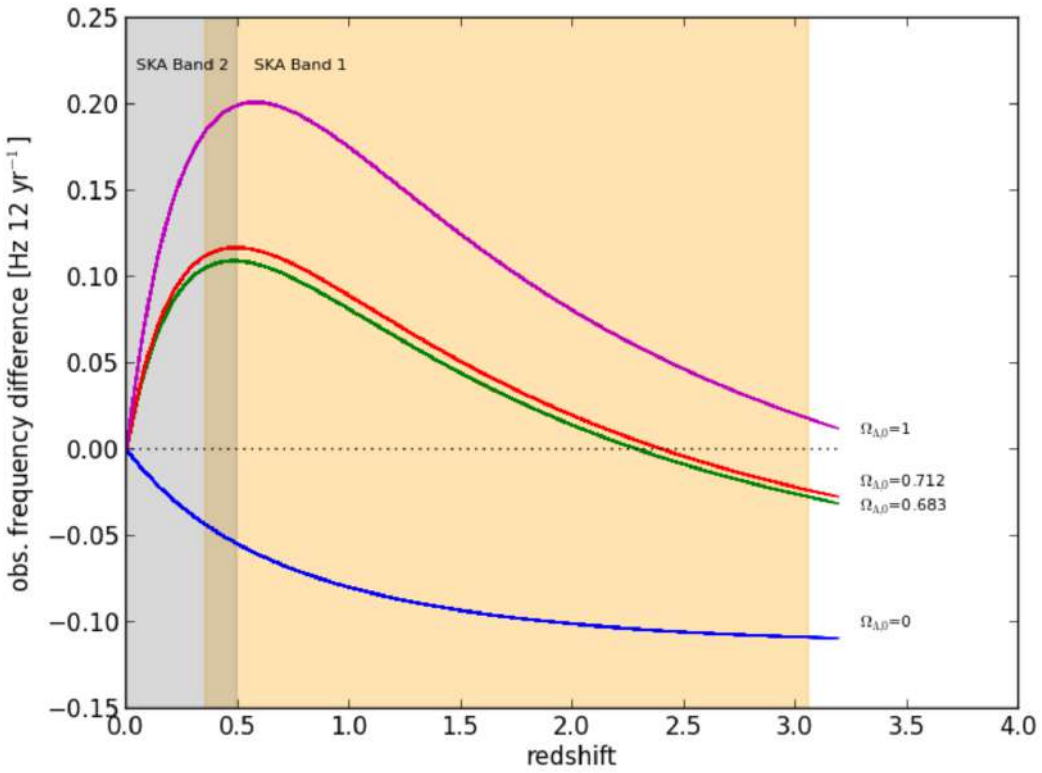

Figure 3.5.: Frequency drift measurement using the SKAO survey, given in $Hz/12$yrs. The dark and yellow lights are the redshift range coverage of the SKA bands, respectively; and the curves are based on different ΛCDM dark energy density parameters Ω_Λ. Taken from [80].

Redshift drift detection by the SKAO survey was first explored extensively in [80], and will rely on measurements the frequency drift of HI neutral hydrogen emission lines which, lying in the L band of the spectrum, are not affected by atmospheric or ionosphere emissions and are especially well-suited to trace sources at redshifts $z \lesssim 1$. As first mentioned by Loeb and established in Liske et al, detecting the drift at the highest possible redshift range is fundamental to significantly constrain the cosmological parameters, and thus synergy between experiments surveying different redshift ranges should be a goal for redshift drift cosmology. To achieve a detection of the drift within 5% accuracy, [80] proposed an all-sky survey using both phases of the SKAO experiment, with a 12yrs experiment time, observing sources to redshift up to $z = 1$. In figure 3.5 we show the frequency drift measurement in the redshift range covered by the SKAO survey and using the 12yrs experiment time proposed by [80]. An analysis of synergy between SKA, ELT and the CHIME experiments can be found in [59, 65].

We also note that the difference in the redshift ranges between experiments is intrinsically related to their instrument capabilities and focus on different ranges of the electromagnetic spectrum; SKA in particular will perform stacking of millions of sources at different redshifts [78, 79], which is only possible to redshifts up to z 1, whereas the ELT ANDES spectrograph will perform the Sandage-Loeb test of Lyman-α line observations, which are detectable

3.2.2. Forecasts

With the advent and construction of next-gen telescopes, forecasts and predictions for realistic measurements of the redshift drift using these new facilities has been a focus of research in the area in the past decade [66, 65, 81, 71, 82, 73], streamlining the data and statistical analysis needed for cosmology when facilities enter operation and start gathering spectroscopic data.

Proof of concept measurements of the drift, illustrating possible systematics and experimental challenges in future measurements, both in the Sandage-Loeb test and using HI spectral lines, were performed in [75] and [83], both in the optical and radio lines. Such measurements bound the intrinsic cosmic acceleration of the measured spectroscopic velocity to be of order $\dot{v}_{\rm spec} \leq 10^{-2}$km/s yr accompanying the Lyman-α forest of 4 different quasars at z 2.5; and of 10^{-3}km/s yr through observation of HI absorption lines at z 0.5. Both measurements have low confidence $< 3\sigma$ and are at least 3 orders of magnitude greater than the predicted drift for objects at the observed redshifts, such that they serve as a first example in methodologies to measure the effect.

Here we show some of the up-to-date forecasts on the spectroscopic velocity and redshift drift, as well realistic constraints on cosmology from redshift drift physics. We focus on papers performing forecasts for the aforementioned experiments SKAO and ELT, and also the synergy between them. Among them, we focus on the works [73, 65, 81] and references provided therein.

In forecasting future measurements and constraints on cosmology from redshift drift physics, it is common to adopt the CPL parametrization, which captures the dynamics of interacting and modified gravity models by adding another model parameter to the Dark Energy equation of state [84]

$$w_{\rm DE} = w_0 + w_a \frac{z}{(1+z)}, \tag{3.10}$$

where w_0 is the dark energy equation of state at $z = 0$. This parametrization is extensively used to describe the background dynamics of extensions of the ΛCDM model without the need of model specific dynamical equations [85]. A redshift drift measurement can constrain both w_0 and w_a in a model independent way, and thus distinguish between ΛCDM and extended models.

In [81] the authors provided first forecasts on constraining dark energy models using the CPL parametrization by emulating measurements of the drift for both the SKA and ELT facilities, in addition to the CHIME hydrogen intensity mapping experiment [77]. The authors performed a Fisher matrix analysis [24, 20] by modeling the drift uncertainty through (3.9) for the ELT, using the extended analysis of [77] for CHIME and the SKA proposal in [80].

By defining the adimensional observed redshift and velocity drift, S_z and S_v respectively, as

$$S_z \equiv \frac{1}{H_{100}} \frac{\Delta z}{\Delta t} = h\,(1 + z + H(z)/H_0) \tag{3.11}$$

$$S_v \equiv \Delta v = c H_{100} \Delta\tau \left(1 - \frac{H(z)}{H_0(1+z)}\right), \tag{3.12}$$

where $H_{100} = 100$km/s/Mpc. One can find the sensitivity of the observed drifts S to the cosmological parameters in the CPL parametrization h, Ω_m, w_0 and w_a from its partial derivatives in relation to the parameters $\partial S/\partial_w$. The sensitivities are a function of redshift, and thus allow one to determine the best redshift range for constraining cosmology from observations of the drift. In figure 3.6 we show the redshift dependence of the sensitivities for each parameter in the CPL parametrization, first derived in [81]. It is interesting to notice that both sensitivities S_v and S_z in relation to all parameter except Ω_m are higher at redshifts $z < 2$, which, as previously

discussed, is the range which the SKAO survey will cover, making it particularly well-suited for using the drift to constrain these parameters.

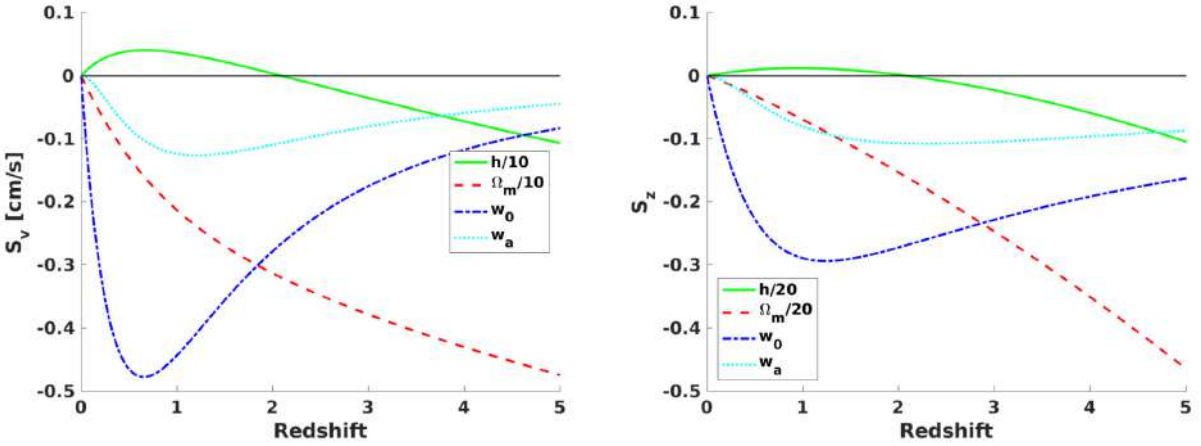

Figure 3.6.: Spectroscopic velocity and redshift drifts for cosmological parameters in the CPL parametrization $\partial S/\partial w_i$. Taken from [81]. Notice how the dependency on h changes sign, as this tracks the cosmological dynamics.

From the sensitivities, the authors performed a Fisher matrix analysis [24, 20, 59] to obtain constraints on the cosmological parameters based on each experiment observation time and uncertainty. For the ELT, the authors modeled the uncertainty on the velocity drift through equation (3.9) and assumed four drift measurements at $z = 2.0, 2.5, 3.0, 3.5, 4.5$ and an experiment time of $\Delta\tau = 20$yrs; for SKA the authors assumed measurements at redshifts $z = 0.1, 0.2, 0.3, 0.4, 0.5$ with uncertainty $\sigma_v(z) = 2z/10$ and an observation time of $\Delta\tau = 0.5$yrs per redshift; and for the CHIMES experiment, the authors assumed measurements at redshift bins centered at $z = 1.0, 1.4, 1.9, 2.3$, uncertainties given $\sigma_v = 0.8, 0.9, 1.3, 1.4$cm/s, with an experiment time of $\Delta\tau = 10$yrs.

To perform the full Fisher matrix analysis the authors also derive the Figure of Merit FoM of the CPL parameters for the predicted measurements. One can find the definition of the Figure of Merit FoM of two parameters X, Y, a quantity related to the certainty on their measurement, in appendix B.

In table 3.1 we show the results for ΛCDM, and in figure 3.7 we show the 1σ contour curves for certain parameters in the CPL parametrization, both taken from [81]. Forecasts including cosmological priors from the Planck experiments are also included in the results of the confidence contours.

It is clear that the figure of merit and uncertainty dramatically improve when all measurements are combined. Figure 3.7 also shows the improvement when combining the measurements. Although the contours are not better than constraints from CMB and LSS [81], by including priors from these cosmological tracers, such as results from the Planck and Euclid missions, these are dramatically improved. A detailed discussion on the impact of these priors is found in the above reference.

In the papers [65, 73] the authors expanded the forecasts for the SKA and ELT experiments to derive constraints on the cosmographic parameters (3.4) and the second time derivative of the redshift $\ddot{z}$, performing a full cosmographic analysis from redshift drift physics. Although in principle it should be possible to constrain cosmology up to the second derivative of the scale factor $a(t)$ through observations of the redshift drift, this is also very dependent on the observation

Parameter	ELT	SKA	CHIME	All
$C(h, \Omega_m)$	-0.930	0.993	0.721	0.902
$FoM(h, \Omega_m)$	86	903	85	3505
$\sigma(\Omega_m)$	0.047	0.042	0.028	0.011
$\sigma(h)$	0.293	0.096	0.265	0.027

Table 3.1.: Results of the Fisher Matrix analysis done in [81] for the ΛCDM model. The first line shows the correlation coefficient C for the two parameters, the next one the Figure of Merit FoM, and the last two the one-sigma marginalized uncertainties for the two parameters. The All case corresponds to the combination ELT+SKA+CHIME. Taken from the same reference.

time and synergy of future facilities.

We conclude this section by emphasizing that although there are a handful of works on forecasts for the experiments currently under construction that will have the capability of measuring the drift, there is still work to be done in modeling uncertainties and systematics in the future observations of the drift. Much of this work will only be possible once the full specifications of the instruments built are available [81, 59] and actual research plans are set. Thus, much of the work on this topic is a baseline for future experiments and observations. Beyond the ELT, SKA and CHIME surveys, one can also find proposals for new "accelerometers" and forecasts on these experiments in the references [75, 74, 82].

3.3. The Redshift Drift in General Spacetimes

The discussion in the previous section establishes that the redshift drift unambiguously distinguishes an accelerating cosmological expansion without relying on any assumptions on the energy content of the Universe. Our discussion, however, has relied on the background FLRW metric (2.2) as the metric that describes large scale cosmological behavior, a fundamental assumption of the ΛCDM model. We concluded using this assumption that the detection of a positive signal of the redshift drift at redshifts where the Λ term dominates is an independent evidence for dark energy.

The (statistical) cosmological principle and the existence of a dark energy component in the energy content of the Universe discussed in chapter 2, although paradigms of the concordance model, are theoretical hypothesis that can not only be tested by cosmological observations that do not rely on their assumptions, but avoided altogether in alternative cosmological models. Theoretical proposals such as backreaction and inhomogeneous cosmological models [86, 87, 88] and previously mentioned modified gravity theories [58] propose an alternative cosmology where Dark Energy could be explained by the effects of a different underlying metric or geometry of the Universe.

With the possibility of testing cosmological scenarios beyond the cosmological principle and the ΛCDM paradigm, it is important to understand the definition and behavior of redshift drift observations in these alternative scenarios, such that one can properly make sense of a measurement that doesn't rely on these assumptions. Theoretical developments in this direction have led to the proposal of using the redshift drift as a probe of the Copernican principle when combined with cosmological distance data [89], able to constrain deviations from homogeneous spherical symmetry, such as in the LTB case [90, 91, 89, 92].

Furthermore, although there has been work in modeling the impact of contaminating effects

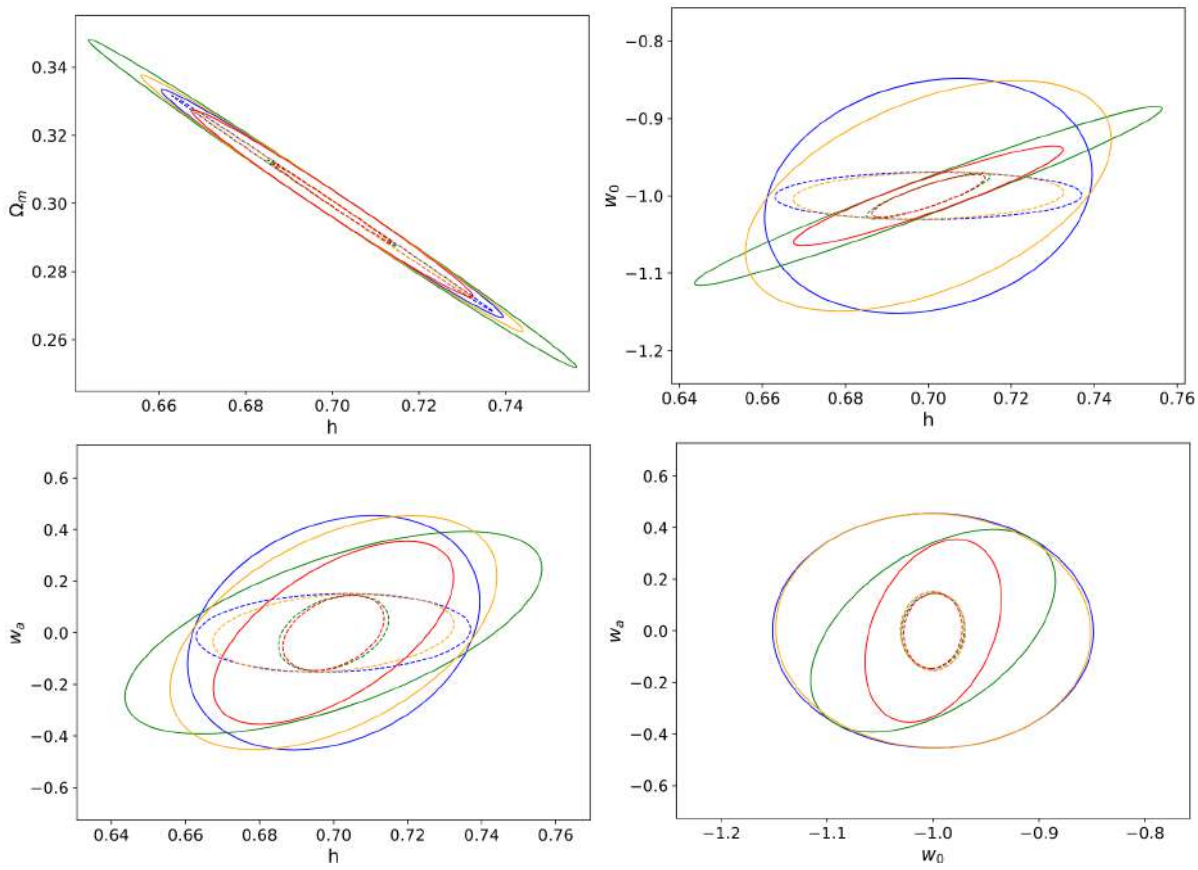

Figure 3.7.: Contour plots for 1σ constraints on a set of cosmological parameters in the CPL parametrization. The solid blue, green and yellow lines are the results obtained from the ELT, SKA and CHIME experiments, respectively. The solid red line is the combination of all three results. Dashed lines include priors from Planck and Euclid-like missions. Taken from [73]

and local cosmological behavior on redshift drift measurements [93], a full theoretical treatment for the perturbative effects arising from inhomogeneities due perturbations in the metric (2.21) has been lacking, though a first approach was laid out in [93, 94]. One of the main results of this thesis is a first treatment of such kind from first principles, relying on the formulation of the redshift drift in cosmological space-times beyond the background FLRW metric.

In order to fully model the redshift drift and understand its behavior in full generality, one needs to extend the definition (3.1) to arbitrary space-times. In this section we develop the redshift drift formalism in general space-times, following the recent work in the area by Heinesen and Koksbang [8, 9, 95, 91], which builds a generalized redshift drift multipole expansion in terms of kinematic quantities, allowing one to build a model-independent cosmography. We'll show how this formalism reduces to the usual drift equation (3.1) in the FLRW case, and apply it to two important cases: the LTB and Bianchi I metrics. We'll also show that, with some assumptions, violations of the weak energy condition correspond to positive values of the redshift drift, an important result first derived in [9].

As a quantity defined on null geodesics intersecting an observer's worldline, the tool used to describe the redshift drift and its dynamics in arbitrary spacetimes is the mathematical formalism

of null geodesics in pseudo-Riemannian manifolds, the main object of study of gravitational lensing theory. Here we will define the redshift drift through this formalism and proceed to use the multipole cosmographical expansion described in [96] to study its behavior. The mathematical theory of gravitational lensing can be found in the important references [97, 98, 99].

3.3.1. Redshift Drift definition and expansion

Let $\mathcal{O}$ and $\mathcal{S}$ be arbitrary observer and source, respectively, with worldlines $\gamma_{\mathcal{O}}$ and $\gamma_{\mathcal{S}}$, parametrized by proper times $\tau_{\mathcal{O}}$ and $\tau_{\mathcal{S}}$, and having 4-velocities $u^{\mu}_{\mathcal{O}}$ and $u^{\mu}_{\mathcal{S}}$. The source $\mathcal{S}$ emits a signal observed by $\mathcal{O}$, which is in turn parametrized by a null-geodesic congruence tangent 4-vector k^{μ}. We illustrate the geometrical setting of the events in spacetime in figure 3.8. We assume that the null geodesics in the congruence are free of caustics, such that the induced map between the observer and source proper times $\tau_{\mathcal{S}} \mapsto \tau_{\mathcal{S}}(\tau_{\mathcal{O}})$ is bijective. Then we can define the redshift z measured by the observer $\mathcal{O}$ at proper time τ_0

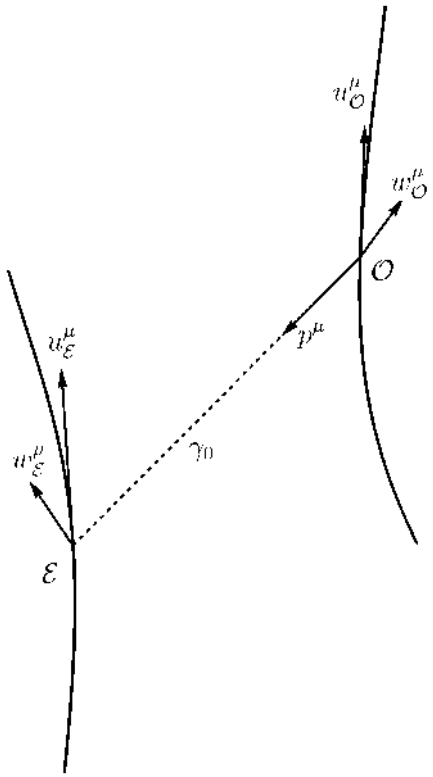

Figure 3.8.: Observer and source worldlines connected by a null geodesic defining the light signal emitted from the source. Here $\mathcal{E}$ is the source (or emitter) and w^{μ} is their 4-acceleration. p^{μ} is the null geodesic parametrizing tangent 4-vector, and γ_0 the null geodesic. Taken from [97].

$$z(\tau_0) \equiv \frac{u_{\mathcal{S}\mu}(\tau_{\mathcal{S}}(\tau_0))k^{\mu}}{u_{\mathcal{O}\mu}(\tau_0)k^{\mu}} - 1 = \frac{E_{\mathcal{S}}(\tau_{\mathcal{S}}(\tau_0))}{E_{\mathcal{O}}(\tau_0)} - 1, \tag{3.13}$$

where we implicitly defined the energy at the source and observer in a similar way to definition (2.64). By taking the derivative in relation to the observer's proper time $\tau_{\mathcal{O}}$ we obtain

$$\left.\frac{dz(\tau_0)}{d\tau_{\mathcal{O}}}\right|_{\mathcal{O}} = \frac{E_{\mathcal{O}} dE_{\mathcal{S}}/d\tau_{\mathcal{O}} - E_{\mathcal{S}} dE_{\mathcal{O}}/d\tau_{\mathcal{O}}}{E_{\mathcal{O}}^2} = \frac{dE_{\mathcal{S}}/d\tau_{\mathcal{O}}}{E_{\mathcal{O}}} - (1+z)\frac{dE_{\mathcal{O}}/d\tau_{\mathcal{O}}}{E_{\mathcal{O}}}$$
$$= \frac{u^\mu_{\mathcal{O}} \nabla_\mu E_{\mathcal{S}}}{E_{\mathcal{O}}} - (1+z)\frac{u^\mu_{\mathcal{O}} \nabla_\mu E_{\mathcal{O}}}{E_{\mathcal{O}}}, \tag{3.14}$$

where we used the fact that the observer and source 4-velocities are tangent to their worldlines, and the chain rule

$$\frac{d}{d\tau_i} = u^\mu_i \nabla_\mu.$$

It is easy to see that (3.14) reduces to (3.1) in the case of a comoving observer in the Robertson-Walker metric. This definition is general and independent of space-time and the congruence of either observer or source.

We extend the definition of the kinematic quantities in (2.31, 2.32) to general spacetimes writing

$$\theta \equiv \nabla_\mu u^\mu\,, \quad \sigma_{\mu\nu} \equiv P^\alpha_\mu P^\beta_\nu \nabla_\alpha u_\beta - \frac{1}{3} P^\alpha_\gamma P^{\beta\gamma} \nabla_\alpha u_\beta\,, \tag{3.15}$$

$$\omega_{\mu\nu} \equiv P^\alpha_\mu P^\beta_\nu \nabla_{[\alpha} u_{\beta]}\,, \quad a^\mu \equiv u^\mu \nabla_\mu u_\nu, \tag{3.16}$$

where $P^\alpha_\beta = g^\alpha_\beta + u^\alpha u_\beta$ is the projection tensor onto the space-like hypersurfaces parametrized by the 4-velocity u^μ. We call θ, σ, ω and a the expansion, shear, vorticity and acceleration of the space-like congruence.

By assuming that both observer and source follow the same global spacetime congruence defined by a 4-velocity u^μ, which in the FLRW case reduces to events comoving with the Hubble flow, we can decompose the signal tangent 4-vector k^μ into normalized spatial propagation e^μ and spacetime propagation u^μ vectors as [20, 97]

$$k^\mu = E(u^\mu - e^\mu)\,, \quad e^\mu e_\mu = 1, \tag{3.17}$$

where we dropped the subcripts. Note, however, that the velocity and energy are still dependent on observer and source, since the events have their own proper time. The 4-vector $-e^\mu$, in this case, is interpreted as the spatial propagation vector of the light signal directed at the observer.

Using the kinematic quantities above and the decomposition of the photon tangent 4-vector, one can define a measure of the spacetime expansion along a geodesic 4-vector k^μ, which in the FLRW case reduces to the Hubble parameter (2.6), as

$$\mathfrak{H} \equiv -\frac{k^\mu \nabla_\mu E}{E^2} = \frac{\theta}{3} - e^\mu a_\mu + e^\mu e^\mu \sigma_{\mu\nu}, \tag{3.18}$$

where once again we dropped the subscripts since the kinematic quantities are globally defined by the 4-velocity congruence. The equality can be easily derived by a quick calculation and the use of the parallel propagation of the null tangent vector k^μ. We'll call $\mathfrak{H}$ the generalized Hubble parameter.

Using this generalized Hubble parameter in definition (3.14), we can write the general redshift drift in a form that closely resembles (3.1)

$$\left.\frac{dz}{d\tau}\right|_{\mathcal{O}} = \mathfrak{H}_{\mathcal{O}} - (1+z)\mathfrak{H}_{\mathcal{S}} + \mathfrak{s}_{\mathcal{S}\to\mathcal{O}}, \tag{3.19}$$

where the term $\mathfrak{s}_{\mathcal{S}\to\mathcal{O}}$ is the variation of the spatial propagation vector e^μ along the path from source to observer, also called the direction drift,

$$\mathfrak{s}_{\mathcal{S}\to\mathcal{O}} = \left.\frac{e^\mu \nabla_\mu E}{E}\right|_{\mathcal{O}} - (1+z)\left.\frac{e^\mu \nabla_\mu E}{E}\right|_{\mathcal{S}}. \tag{3.20}$$

In the FLRW case, we have $\mathfrak{H} = H$ and $\mathfrak{s}_{\mathcal{S}\to\mathcal{O}} = 0$, such that equation (3.19) reduces to (3.1). Equation (3.19) is fully general and conditional only on the existence of a global 4-velocity field defining a time-like congruence for events.

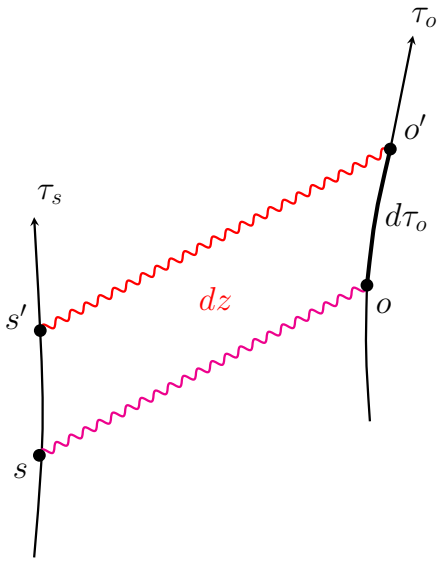

Figure 3.9.: The redshift fluctuation as the difference between two measurements by the observer $\mathcal{O}$ of a light signal emitted by source $\mathcal{S}$ at different proper times, as described in equation (3.14). Taken from [10].

3.3.1.1. Multipole Expansion and violations of the Strong Energy Condition

The direction drift (3.20) can be written as an integral on the photon geodesic with tangent 4-vector k^μ as

$$\mathfrak{s}_{\mathcal{S}\to\mathcal{O}} = E_{\mathcal{S}} \int_{\lambda_{\mathcal{O}}}^{\lambda_{\mathcal{S}}} d\lambda \mathcal{I}\,, \quad \mathcal{I} \equiv -k^\alpha \nabla_\alpha \left(\frac{k^\mu \nabla_\mu E}{E^2}\right), \tag{3.21}$$

where the parameter λ satisfies the curve-length parametrization property $\nabla_\mu k^\mu \lambda = 1$. The integrand $\mathcal{I}$, a measure of the instantaneous variation of the rate of change of the photon's energy in the photon's propagation direction, can be further expanded into a multipole series on the photon's spatial propagation vector e^μ by rewriting it as [96]

$$\mathcal{I} = e^\mu \nabla_\mu \mathfrak{H} + e^\mu a_\mu \mathfrak{H} - \frac{1}{E^2} p^\mu_\nu \mathcal{L}_{k^\alpha}(e^\nu) \nabla_\mu E, \tag{3.22a}$$

$$\mathcal{L}_{k^\mu}(e^\mu) = p^\mu_\nu \mathcal{L}_{k^\alpha}(e^\nu) + k^\mu e^\nu a_\nu + 2e^{[\mu} u^{\nu]} \nabla_\nu E, \tag{3.22b}$$

where $p^{\mu\nu} = P^{\mu\nu} - e^\mu e^\nu = g^{\mu\nu} + u^\mu u^\nu - e^\mu e^\nu$ is the projection onto the subspace generated by the hyperplane perpendicular to the 4-vectors k^μ and u^μ, also called the Screen or Sachs Screen, and $\mathcal{L}_{k^\alpha}(e^\nu) = [k^\alpha, e^\nu] = k^\alpha \nabla_\alpha e^\nu - e^\alpha \nabla_\alpha k^\nu$ is the Lie derivative of e^μ in the flow direction of k^μ.

We can further expand expression (3.22a) and write it using the kinematic variables (3.15) to obtain the final multipole expansion

$$\mathcal{I} = \mathcal{I}^0 + e^\mu \mathcal{I}^e_\mu + d^\mu \mathcal{I}^d_\mu + e^\mu e^\nu \mathcal{I}^{ee}_{\mu\nu} + e^\mu d^\nu \mathcal{I}^{ed}_{\mu\nu} + e^\mu e^\nu e^\rho \mathcal{I}^{eee}_{\mu\nu\rho}, \tag{3.23}$$

where the multipole expansion coefficients are given by

$$\begin{aligned}
\mathcal{I}^0 &\equiv -\frac{1}{3}(4\omega^{\mu\nu}\omega_{\mu\nu} + D_\mu a^\mu + a^\mu a_\mu) - h_{\mu\nu} d^\mu d^\nu \,, \\
\mathcal{I}^d_\mu &\equiv \frac{1}{3}(D_\mu \theta + \theta a_\mu) + \frac{3}{5} P^{\nu\rho}\big(D_{(\rho}\sigma_{\mu\nu)} + a_{(\rho}\sigma_{\mu\nu)}\big) - 2a^\nu \omega_{\mu\nu} \,, \\
\mathcal{I}^d_\mu &\equiv -2a_\mu \,, \\
\mathcal{I}^{ee}_{\mu\nu} &\equiv -\left(4\omega_{\alpha\mu}\sigma^\alpha_{\ \nu} + 4\omega_{\alpha\langle\mu}\omega^\alpha_{\ \nu\rangle} + D_{\langle\nu}a_{\mu\rangle} + a_{\langle\mu}a_{\nu\rangle}\right) \,, \\
\mathcal{I}^{ed}_{\mu\nu} &\equiv 4(\sigma_{\mu\nu} - \omega_{\mu\nu}) \,, \\
\mathcal{I}^{eee}_{\mu\nu\rho} &\equiv D_{\langle\rho}\sigma_{\mu\nu\rangle} + a_{\langle\rho}\sigma_{\mu\nu\rangle} \,,
\end{aligned} \tag{3.24}$$

and we defined the projection of the spatial propagation vector covariant derivative on the Sachs Screen $d^\nu \equiv p^\nu_\mu e^\alpha \nabla_\alpha e^\mu$, denoting the covariant derivative projected along the space-like congruence by $D_\mu \equiv P^\nu_\mu \nabla_\nu$, and $_{\langle ij\rangle}$ denotes the trace-free symmetric part of the spatial projection of the tensor, defined by

$$T_{\langle\mu\nu\rangle} = T_{(\mu\nu)} - \frac{1}{3} P_{\mu\nu} g^{\alpha\beta} T_{\alpha\beta}, \tag{3.25}$$

where $_{()}$ denotes symmetrization of the tensor.

The derivation of the multipole expansion can be followed through in the original paper [96].

Expression (3.23) was first derived in [96] and fully characterizes the direction drift through the kinematic variables. The expression includes all the terms for the multipole expansion, such that truncation is exact and includes all the non-vanishing terms.

In the case of a perturbed FLRW metric, with kinematic variables given by (2.32), the perturbations are averaged out for a large number of observations, such that the average redshift drift satisfies

$$\begin{aligned}
\left\langle \left.\frac{dz}{dt}\right|_{\mathcal{O}} \right\rangle &= \langle \mathfrak{H}_{\mathcal{O}} \rangle + (1 + z_{\mathcal{S}}) \langle \mathfrak{H}_{\mathcal{S}} \rangle + E_{\mathcal{S}} \left\langle \int_{\lambda_{\mathcal{O}}}^{\lambda_{\mathcal{S}}} d\lambda \mathcal{I} \right\rangle \\
&= H_0 - (1 + z_{\mathcal{S}}) H(z) + E_{\mathcal{S}} \int_{\lambda_{\mathcal{O}}}^{\lambda_{\mathcal{S}}} d\lambda \langle \mathcal{I} \rangle \\
&= H_0 - (1 + z_{\mathcal{S}}) H(z),
\end{aligned} \tag{3.26}$$

where we used that the only non-vanishing contribution from the kinematic quantities comes from the expansion θ. This result is expected: fluctuations shouldn't contribute to the average signal of the drift. It also makes precise the idea that cosmic structures shouldn't affect the sign of the redshift drift, and a positive signal could not be detected due to fluctuations from homogeneity in the Universe. In the general case, even with the hypothesis of average homogeneity and

isotropy, one cannot guarantee that the contributions to the multipole terms (3.24) will cancel out on average, such that deviations from homogeneity and isotropy could change the drift signal entirely [96].

One can extend the multipole expansion for the direction drift (3.23) to write the general redshift drift (3.14) as a multipole expansion over the spatial propagation vector. By writing the time part of the right hand side of (3.14) as an integral

$$\mathfrak{H}_{\mathcal{O}} - (1+z)\mathfrak{H}_{\mathcal{S}} = \int_{\lambda_{\mathcal{S}}}^{\lambda_{\mathcal{O}}} d\lambda \mathcal{A}\,, \quad \mathcal{A} \equiv k^{\nu}\nabla_{\nu}\left(\frac{\mathfrak{H}}{E}\right), \tag{3.27}$$

we can write

$$\left.\frac{dz}{d\tau}\right|_{\mathcal{O}} = \int_{\lambda_{\mathcal{S}}}^{\lambda_{\mathcal{O}}} d\lambda \Pi\,, \quad \Pi = \mathcal{I} + \mathcal{A}, \tag{3.28}$$

and the $\mathcal{A}$ can be expanded as

$$\mathcal{A} = \mathcal{A}^{0} + e^{\mu}\mathcal{A}^{e}_{\mu} + e^{\mu}e^{\nu}\mathcal{A}^{ee}_{\mu\nu} + e^{\mu}e^{\nu}e^{\rho}\mathcal{A}^{eee}_{\mu\nu\rho} + e^{\mu}e^{\nu}e^{\rho}e^{\kappa}\mathcal{A}^{eeee}_{\mu\nu\rho\kappa}, \tag{3.29}$$

where the coefficients are given by

$$\begin{aligned}
\mathcal{A}^{0} &\equiv -\frac{1}{3}R_{\mu\nu}u^{\mu}u^{\nu} + \frac{2}{3}D_{\mu}a^{\mu} - \frac{3}{5}\sigma^{\mu\nu}\sigma_{\mu\nu} + \frac{1}{3}\omega^{\mu\nu}\omega_{\mu\nu}\,,\\
\mathcal{A}^{e}_{\mu} &\equiv -\frac{2}{3}\theta a_{\mu} + a^{\nu}\sigma_{\mu\nu} + a^{\nu}\omega_{\mu\nu}\\
&\quad - \frac{1}{3}D_{\mu}\theta - \frac{2}{5}D_{\nu}\sigma^{\nu}_{\ \mu} - h^{\nu}_{\mu}\dot{a}_{\nu}\,,\\
\mathcal{A}^{ee}_{\mu\nu} &\equiv 3a_{\langle\mu}a_{\nu\rangle} - 2\sigma_{\alpha\mu}\omega^{\alpha}_{\ \nu} - \frac{9}{7}\sigma_{\alpha\langle\mu}\sigma^{\alpha}_{\ \nu\rangle} + \omega_{\alpha\langle\mu}\omega^{\alpha}_{\ \nu\rangle}\\
&\quad + 2D_{\langle\mu}a_{\nu\rangle} - u^{\rho}u^{\sigma}C_{\rho\mu\sigma\nu} - \frac{1}{2}h^{\alpha}_{\langle\mu}h^{\beta}_{\nu\rangle}R_{\alpha\beta}\,,\\
\mathcal{A}^{eee}_{\mu\nu\rho} &\equiv -D_{\langle\rho}\sigma_{\mu\nu\rangle} - 5a_{\langle\mu}\sigma_{\nu\rho\rangle}\,,\\
\mathcal{A}^{eeee}_{\mu\nu\rho\kappa} &\equiv 3\sigma_{\langle\mu\nu}\sigma_{\rho\kappa\rangle}\,,
\end{aligned} \tag{3.30}$$

where $C_{\alpha\mu\beta\nu}$ is the Weyl tensor. Once again we note that the expansion is exact and includes all non-vanishing terms for the multipole coefficients. It was first derived in [8], and we shall follow the reasoning in the paper to derive an important result with the help of this multipole expansion.

Using (3.23) and (3.29), we can write the redshift drift entirely in terms of the multipole expansion over e^{μ} using the kinematic quantities and their derivatives, and rewriting the integrand in (3.28) as

$$\Pi = \Pi^{0} + e^{\mu}\Pi^{e}_{\mu} + d^{\mu}\Pi^{d}_{\mu} + e^{\mu}e^{\nu}\Pi^{ee}_{\mu\nu} + e^{\mu}d^{\nu}\Pi^{ed}_{\mu\nu} + e^{\mu}e^{\nu}e^{\rho}\Pi^{eee}_{\mu\nu\rho} + e^{\mu}e^{\nu}e^{\rho}e^{\kappa}\Pi^{eeee}_{\mu\nu\rho\kappa}\,, \tag{3.31}$$

where

$$
\begin{aligned}
\Pi^0 &\equiv -\frac{1}{3}R_{\mu\nu}u^\mu u^\nu + \frac{1}{3}D_\mu a^\mu - \frac{1}{3}a^\mu a_\mu \\
&\quad - d^\mu d_\mu - \frac{3}{5}\sigma^{\mu\nu}\sigma_{\mu\nu} - \omega^{\mu\nu}\omega_{\mu\nu}\,, \\
\Pi^e_\mu &\equiv -\frac{1}{3}\theta a_\mu + \frac{7}{5}a_\nu\sigma^\nu_\mu - a^\nu\omega_{\mu\nu} - h^\nu_\mu \dot{a}_\nu\,, \\
\Pi^d_\mu &\equiv -2a_\mu\,, \\
\Pi^{ee}_{\mu\nu} &\equiv 2a_{\langle\mu}a_{\nu\rangle} - \frac{9}{7}\sigma_{\alpha\langle\mu}\sigma^\alpha_{\nu\rangle} - 3\omega_{\alpha\langle\mu}\omega^\alpha_{\nu\rangle} - 6\sigma_{\alpha\mu}\omega^\alpha_\nu \\
&\quad + D_{\langle\mu}a_{\nu\rangle} - u^\rho u^\sigma C_{\rho\mu\sigma\nu} - \frac{1}{2}h^\alpha_{\langle\mu}h^\beta_{\nu\rangle}R_{\alpha\beta}\,, \\
\Pi^{ed}_{\mu\nu} &\equiv 4(\sigma_{\mu\nu} - \omega_{\mu\nu})\,, \\
\Pi^{eee}_{\mu\nu\rho} &\equiv -4a_{\langle\mu}\sigma_{\nu\rho\rangle}\,, \\
\Pi^{eeee}_{\mu\nu\rho\kappa} &\equiv 3\sigma_{\langle\mu\nu}\sigma_{\rho\kappa\rangle}\,,
\end{aligned}
\tag{3.32}
$$

where we used $\dot{} \equiv u^\nu\nabla_\nu$. For a derivation of (3.30) and (3.32) the reader is referred to [8].

In the FLRW case, the only nonvanishing contribution comes from the monopole $-\frac{1}{3}R_{\mu\nu}u^\mu u^\nu = \ddot{a}/a$, such that the integral in (3.28) reduces to the usual expression (3.1).

One can make the physically motivated assumption that the dominant term in (3.31) is the monopole, such that higher order terms, explicitly dependant on the photon's direction, do not significantly modify the photon's spatial propagation. Although this is false in general, when considering physically well-motivated spacetimes describing the large-scale dynamics of the Universe, one expects that the kinematic properties of its energy content should not be strongly observer or direction dependent, since we observe a Universe that is close to statistically homogeneous and isotropic. Another physical interpretation of this assumption is that the kinematic evolution of the cosmic fluid happens at a time scale much slower than the photon's propagation to the observer time scale, which is also well-motivated from an observational perspective, based on the discussion in chapter 2. A more in-depth discussion of this hypothesis and its physical motivation can be found in the original papers [8, 95, 96].

An important application of the multipole expansion, explored first in the papers [91, 100], is a comparison between the redshift drift average and the average of the drift, which should not necessarily match in a locally inhomogeneous or on average inhomogeneous Universe, since the average redshift drift, due to the overall cosmic acceleration, should match the average of the drift of sources in the local Universe only in the case of statistically homogeneous models. Equation (3.26) shows that small fluctuations due to cosmic structures should not impact measurements of the drift, since perturbations average out over an ensemble of measurements. Thus comparison between the average of the drift and the drift of the average redshift can be used as a test for cosmic homogeneity.

In the case of a dominant monopole term, we have for the redshift drift

$$
\left.\frac{dz}{d\tau}\right|_{\mathcal{O}} = E_{\mathcal{S}}\int_{\lambda_{\mathcal{S}}}^{\lambda_{\mathcal{O}}} d\lambda\Pi^0, \tag{3.33}
$$

where we note that all terms in Π^0 are strictly negative with the exception of $-\frac{1}{3}(R_{\mu\nu}u^\mu u^\nu - D_\mu a^\mu + a_\mu a^\mu)$. Thus, in order for the redshift drift to have a positive value, one either has $R_{\mu\nu}u^\mu u^\nu < 0$ or $D_\mu a^\mu - a_\mu a^\mu > 0$. In the case where $D_\mu a^\mu - a_\mu a^\mu > 0$, the photon path along

the null geodesic would need to have a particular alignment with the observer's comoving 4-acceleration along the whole photon's trajectory, such that the integrated contribution would be net positive [8]. This alignment, although not impossible, is not physically motivated in general, and in Universe models with some degree of statistical isotropy should not be expected.

The case where $R_{\mu\nu}u^\mu u^\nu < 0$ violates the strong energy condition [98]. Thus, in order for the redshift drift to be positive under the dominant monopole assumption, unless there is a strict alignment between the photon path and the observer congruence 4-acceleration a^μ, one needs a violation of the strong energy condition. This generalizes the result found in FLRW cosmology, where a positive redshift drift indicates a cosmological constant Λ component in the Universe's energy content. We can summarize this result in the statement

$$\left.\frac{dz}{d\tau}\right|_{\mathcal{O}} > 0 \iff \text{Strong Energy Condition is violated.} \tag{3.34}$$

The hypotheses behind this conclusion, namely the dominant monopole assumption and the lack of alignment of the photon path with the observer's co-moving 4-acceleration, should be true for physical spacetimes describing the behavior of the observed Universe, and are true in spacetimes with no local homogeneity or isotropy, such as LTB and Bianchi I cosmologies [91, 101, 102].

This result is important in two ways: For one, it establishes theoretically that the redshift drift is a direct probe of violations of the standard energy content of the Universe, which we know to be true in the FLRW case; and secondly, it extends the idea to more general spacetimes and cosmological models, including cases where homogeneity and isotropy are not necessarily true at certain scales, being a probe into violations of the Strong Energy Condition in cosmological spacetimes. In particular, perturbations to the FLRW metric, satisfying large scale homogeneity and isotropy, cannot contribute significantly to the redshift drift signal. Even in inhomogeneous and anisotropic models, one cannot detect a positive value for the redshift drift due to cosmic structures or kinematics.

For a thorough discussion of this result, the reader is referred to the original paper [9].

3.3.2. Lemaître-Tolmann-Bondi and Bianchi I spacetimes

As an illustration of the results on extending the redshift drift definition and its cosmographic expansion to general spacetimes, we apply the formalism to two important cosmological models which are examples of locally inhomogeneous and anisotropic models.

The Lemaître-Tolman-Bondi metric is given by the line element

$$ds^2 = -dt^2 + \frac{a_\parallel^2(t,r)}{1-k(r)r^2}dr^2 + a_\perp^2(t,r)r^2\left(d\theta^2 + \sin^2(\theta)d\phi^2\right), \quad a_\parallel = \frac{\partial}{\partial r}(ra_\perp), \tag{3.35}$$

where $k(r)$ is the LTB curvature function, which depends on the spatial coordinates; and $a_\parallel$ and $a_\perp$ are the parallel and perpendicular scale factors, respectively. The dependency of $a_\parallel$ and $a_\perp$ on the radial coordinates makes explicit the inhomogeneity of the model, where radial distances are coordinate dependent. In the limit case where $a_\parallel = a_\perp$ and k is constant, the metric reduces to (2.2). Furthermore, in our model we assume that the energy content is given entirely by a dust component $p = 0$.

In the multipole expansion (3.31) the only nonvanishing terms are given by [91]

$$\begin{aligned}\Pi^0 &= -R_{\mu\nu}u^\mu u^\nu - d_\mu d^\mu - \frac{3}{5}\sigma^{\mu\nu}\sigma_{\mu\nu}\,,\\ \Pi^{ee}_{\mu\nu} &= -u^\rho u^\sigma C_{\rho\mu\sigma\nu},\\ \Pi^{ed}_{\mu\nu} &= 4\sigma_{\mu\nu}\,,\end{aligned} \tag{3.36}$$

The Ricci term in (3.36) is $-R_{\mu\nu}u^\mu u^\nu = -4\pi G\rho/3$, such that the multipole expansion reduces to the standard FLRW cosmology in the trivial case. The redshift drift can then be written as

$$\frac{dz}{d\tau}\Big|_{\mathcal{O}} = E_{\mathcal{S}}\int_{\tau_{\mathcal{S}}}^{\tau_{\mathcal{O}}} d\tau\left[-\frac{4\pi G}{3}\rho - d_\mu d^\mu - \frac{3}{5}\sigma_{\mu\nu}\sigma^{\mu\nu} + 4\sigma_{\mu\nu}e^\mu d^\nu - C_{\rho\mu\sigma\nu}u^\rho u^\sigma e^\mu e^\nu\right], \tag{3.37}$$

where the explicit coefficients for the Weyl and shear tensor can be found in [91].

In expression (3.37) it is clear that if the monopole term dominates and the drift flux along the propagation direction d^μ is small , the signal is strictly positive, and in the LTB case reduces to the FLRW result. The amplitude of the inhomogeneous shear and Weyl tensors depend on the metric functions in (3.35), such that for small deviations from the FLRW case, the dominant monopole approximation is valid.

In the works [91, 100], through simulations of the LTB model and n-body simulations based on an EdS background with a local inhomogeneity profile, the authors found results pointing to an average cancellation of inhomogeneity effects when observing the redshift drift from different sources, such that the average drift matches the drift of the average redshift. In this case, the fluctuations along the photon path due to the inhomogeneity of the model cancel out and the remaining contribution to the background acceleration is due to the Ricci focusing term in (3.37), dominates over the contribution from higher multipoles. Although further work in deriving the drift by simulating inhomogeneous cosmologies is needed, the results support the validity of the dominant monopole approximation in realistic inhomogeneous cosmological models.

In the case of anisotropic cosmologies, we choose the Bianchi I metric as an example, with line element given by

$$ds^2 = -dt^2 + \left(e^{2\beta_i(t)}\delta_{ij}dx^i dx^j\right), \quad \sum_{i=1}^{3}\beta_i = 1. \tag{3.38}$$

The different scale factors for each direction in the definition of the above metric are responsible for the anisotropic expansion of the cosmological model. With the above metric, the nonvanishing multipole coefficients (3.24) are the same ones as in the LTB case (3.36).

Denoting derivatives w.r.t. cosmic time with $\dot{}$, and defining an effective Hubble parameter H_i as the rate of expansion in a given direction x_i, we can write

$$\begin{aligned} H_i(t) &= 2\dot{\beta}_i(t)\,, & \theta &= \sum_{i=1} H_i(t)\\ \sigma_{ii} &= \frac{2}{3}\left(H_i - \frac{\theta}{3}\right), & \sigma_{\mu\nu}\sigma^{\mu\nu} &= \frac{1}{3}\sum_i\left(H_i - \frac{\theta}{3}\right)^2, \end{aligned} \tag{3.39}$$

where the non-diagonal and time components of the shear tensor vanish. The Weyl tensor involves second derivatives in cosmic time, so keeping to first order and assuming a source comoving with the observer, we get

$$\frac{dz}{d\tau}\Big|_{\mathcal{O}} = E_{\mathcal{S}} \int_{\tau_{\mathcal{S}}}^{\tau_{\mathcal{O}}} d\tau \left[-\frac{4\pi G}{3}\rho - \frac{1}{5}\sum_i \left(H_i - \frac{\theta}{3} \right)^2 \right], \tag{3.40}$$

showing that even in the idealized case where source and observer follow the same congruence, the effect of an anisotropic expansion could lead to a negative signal of the drift, since the second term in the right hand side of (3.40) is strictly negative. In such a case, measuring a positive value of the redshift drift can also constrain cosmic isotropy, and in particular the cosmic shear $\sigma_{\mu\nu}$, when averaged over the sky. This has been explored, for instance, in [102], where the average drift and the drift of the average redshift were compared as a test of cosmic isotropy.

Perturbations of Cosmological Redshift Drift

The forecasts and predictions for the contaminating effects in observations of the redshift drift, due to the peculiar motion of sources described in 3, are based on naive estimates for the fluctuations in the redshift drift signal. The peculiar velocity, potential and acceleration contributions to the total drift signal have been estimated using phenomenological and experiment-dependent simulations of the source's peculiar motion, such as in the analyses found in the papers [68] and [82], based on the same phenomenological assumptions first laid out in [61]. A first prediction on the contribution from cosmological structures was performed in [94], and an approach aimed at obtaining a full, general expression for the redshift drift using cosmological perturbation theory was performed in [93], although the authors made the assumption that sources are comoving with the observer, such that their peculiar velocity and acceleration vanish identically.

In order to model a measurement of the redshift drift including all contaminating effects and fluctuations in full generality, one should take into account all perturbative effects to the signal, including effects due to structures in the Universe, which photons pass through in their path from source to observer, as well as the scale dependency of the velocity and acceleration of sources. Working from first principles in perturbation theory and using gauge-invariant quantities one can also better understand the contribution from different perturbative effects to the total redshift drift, in an observer independent way, not relying on ad-hoc simplifications.

Furthermore, the power spectrum of the redshift drift fluctuations is a fundamental tool to connect the theoretical predictions for the redshift signal to observations from large scale surveys such as SKA, allowing one to to understand how the observed signal varies with scale and redshift. Through the derivation and numerical implementation of the redshift drift power spectrum in established Einstein-Boltzmann codes such as CLASS [40], creating pipelines for forecasts and statistical analysis of experiments becomes straightforward and allows easy integration with MCMC sampling and regression.

This chapter provides a full derivation of the general, gauge-invariant expression for the redshift drift in ΛCDM cosmology including fluctuations due to cosmic structures and the peculiar motion of sources, at first order in perturbation theory. Our work extends the first approaches found in [94, 93] to arbitrary sources, observers and gauges. We also derive the Power Spectrum of redshift drift fluctuations and obtain first predictions by modifying the Einstein-Boltzmann code CLASS and analyze its correlation with the relativistic galaxy number count.

We first obtain the gauge-invariant expression for the redshift drift in ΛCDM cosmology, using the cosmological perturbation theory laid out in chapter 2 and the general redshift drift definition and expansion described in chapter 3. Our approach is gauge-invariant and does not make assumptions on observer or source. We obtain a general expression for the redshift drift including all first order terms.

Secondly, we derive the theoretical angular power spectrum for the redshift drift fluctuations

and implement it in the Einstein-Boltzmann code CLASS by modifying its transfer function module. This allows us to better understand the contribution of different contaminating effects

Finally, we correlate the redshift drift fluctuation power spectrum and the galaxy number count power spectrum to explore the possibility of using the number count both as a enhancement in the detection of the redshift drift signal and as a complementary observation able to differentiate between the background signal and the fluctuations.

We finish the chapter by discussing how our results impact the literature and contextualize it with the previous results discussed in the last chapter. This chapter follows closely the paper [10], published by the author and collaborators in JCAP.

4.1. Gauge Invariant Redshift Drift

In a perturbed FLRW the observer's 4-velocity and the energy content of the Universe, which we assume to be a perturbed perfect fluid comoving with the observer, without loss of generality, is given by the expressions (2.27) and (2.29) respectively. In (2.63) we have the perturbed photon 4-vector in Newtonian gauge, which we now write in full generality using the metric (2.21), following the derivation found in [20]. The perturbations of the photon 4-vector are determined by integrating the geodesic equation $\nabla_k k = 0$ in the perturbed spacetime. One obtains

$$k^\mu = \bar{k}^\mu + \delta k^\mu \qquad \text{with} \qquad \bar{k}^\mu = \frac{1}{a^2}(1, \bar{n}^i) \qquad \text{and} \tag{4.1a}$$

$$\delta k^0 = \frac{1}{a^2}\delta n^0 = \frac{1}{a^2}\left\{\left[-2A - B_j\bar{n}^j\right]_{\mathcal{S}}^{\mathcal{O}} - \int_{\mathcal{S}}^{\mathcal{O}} d\lambda \, \left[\dot{H}_L - \dot{A} + \dot{H}_{Tab}\bar{n}^a\bar{n}^b - \dot{B}_a\bar{n}^a\right]\right\}, \tag{4.1b}$$

$$\delta k^i = \frac{1}{a^2}\delta n^i = \frac{1}{a^2}\left\{\left[-B^i + 2H_L\bar{n}^i + H_T^{ij}\bar{n}_j\right]_{\mathcal{S}}^{\mathcal{O}} - \int_{\mathcal{S}}^{\mathcal{O}} d\lambda \, \left[\partial^i(H_L - A) + \bar{n}^a\bar{n}^b\partial^i H_{Tab}\right]\right\}, \tag{4.1c}$$

where $\bar{n}^i$ is the unperturbed direction of the photon geodesic satisfying $\bar{n}_i\bar{n}^i = 1$. The integrals are performed along the unperturbed photon geodesic in the background spacetime from source to observer, and λ denotes the affine parameter along the null geodesic. The spacelike direction propagation vector e orthogonal to u from defined in (3.17) is then given by

$$e^\mu = u^\mu - \frac{1}{E}k^\mu = \frac{1}{a}\left(\bar{n}^i(B_i - v_i)\,,\; -\bar{n}^i - \delta n^i + v^i + \bar{n}^i\left(A + \bar{n}^j(B_j - v_j) + \delta n^0\right)\right), \tag{4.2}$$

and the full perturbed expression for the photon energy is given by

$$E = -k_\mu u^\mu = \frac{1}{a}\left[1 + A + \bar{n}^i(B_i - v_i) + \delta n^0\right]. \tag{4.3}$$

With the observer, stress-energy tensor and photon 4-vector perturbed quantities, we find the expression for the Hubble parameter in the perturbed FLRW spacetime using (3.18),

$$\begin{aligned}\mathfrak{H} &= \frac{\theta}{3} - e^\mu a_\mu + e^\mu e^\mu \sigma_{\mu\nu} \\ &= \frac{1}{a}\left[\mathcal{H}(1 - A) - \frac{\Delta v}{3} + \dot{H}_L + \bar{n}_i\partial^i\left(\dot{v} - \dot{B} - A + \mathcal{H}(-B + v)\right) + \bar{n}_i\bar{n}_j\partial_i\partial_j(\dot{H}_T - v) - \frac{1}{3}\Delta(\dot{H}_T - v)\right] \\ &= \frac{1}{a}\left[\mathcal{H}(1 - A) + \dot{\mathcal{R}} - \bar{n}^i\partial_i\left(\dot{V} + \mathcal{H}V - \Psi\right) - \bar{n}^i\bar{n}^j\partial_i\partial_j V\right],\end{aligned} \tag{4.4}$$

where we use the variable $\mathcal{R} = H_L - \frac{1}{3}\Delta H_T$, the spatial curvature perturbation of constant time hypersurfaces. It is clear that this expression is not gauge-invariant, since its background value is the Hubble parameter which is non-vanishing.

To obtain (3.14) we also need to calculate the differential of the energy along the photon geodesic propagation direction, given by $\nabla_e E = e^\mu \nabla_\mu E$, which we integrate along the photon path. By direct calculation, using (4.1) and (4.2) we obtain

$$\nabla_e E = -\frac{1}{a^2}\left[\bar{n}^i\partial_i(A+\delta n^0) + \bar{n}^i\bar{n}^j\partial_i(B_j - v_j) + \mathcal{H}\bar{n}^i(B_i - v_i)\right] . \tag{4.5}$$

We now express $\nabla_e E$ in terms of gauge-invariant variables. In order to arrive at such an expression, we first express the integrand of (4.1b) in terms of the Bardeen potentials using the relations given in Appendix A:

$$\dot{H}_L - \dot{A} + \dot{H}_{Tab}\bar{n}^a\bar{n}^b - \dot{B}_a\bar{n}^a = -\dot{\Phi} - \dot{\Psi} - \dddot{H}_T + \ddot{B} + \bar{n}^i\bar{n}^j\partial_i\partial_j\dot{H}_T + \bar{n}^i\partial_i\dot{B} \quad . \tag{4.6}$$

Next, we use the partial integration formula for a first order quantity f

$$\frac{df}{d\lambda} = \nabla_n f = \dot{f} + \bar{n}^i\partial_i f \quad \Rightarrow \quad \int_{\mathcal{S}}^{\mathcal{O}} d\lambda\, \bar{n}^i\partial_i f = f_o - f_s - \int_{\mathcal{S}}^{\mathcal{O}} d\lambda\, \dot{f} \quad , \tag{4.7}$$

in order to turn the spatial derivatives in $\bar{n}^i\partial_i\dot{B}$ and $\bar{n}^i\bar{n}^j\partial_i\partial_j\dot{H}_T$ into time derivatives, resulting in

$$\int_{\mathcal{S}}^{\mathcal{O}} d\lambda\, \left[\dot{H}_L - \dot{A} + \dot{H}_{Tab}\bar{n}^a\bar{n}^b - \dot{B}_a\bar{n}^a\right] = -\int_{\mathcal{S}}^{\mathcal{O}} d\lambda\,(\dot{\Phi}+\dot{\Psi}) + (\dot{B}_o - \dot{B}_s) + \bar{n}^i\partial_i(\dot{H}_T^o - \dot{H}_T^s) - (\ddot{H}_T^o - \ddot{H}_T^s) \quad . \tag{4.8}$$

In the next step, we evaluate

$$\delta n^0|_{\mathcal{S}}^{\mathcal{O}} = \left[-2A - B_j\bar{n}^j\right]_{\mathcal{S}}^{\mathcal{O}} - \int_{\mathcal{S}}^{\mathcal{O}} d\lambda\, \left[\dot{H}_L - \dot{A} + \dot{H}_{Tab}\bar{n}^a\bar{n}^b - \dot{B}_a\bar{n}^a\right] . \tag{4.9}$$

From here on, we neglect observer dependent terms, related to the monopole and dipole contributions similar to the CMB terms described in chapter 2. These terms give rise to an unmeasurable observer monopole, and an intrisic dipole contribution due to the peculiar motion of the observer. This contribution has been previously studied and constrained in [103], and can be separated from the cosmological signal. Neglecting the observer terms in δn^0 we obtain

$$\delta n^0 = -2A - \bar{n}^i\partial_i\sigma_t + \dot{\sigma}_t - \int_{\mathcal{S}}^{\mathcal{O}} d\lambda\,(\dot{\Phi} + \dot{\Psi}) \quad , \tag{4.10}$$

where we drop the source label $\mathcal{S}$, such that if not specified differently, all terms are to be evaluated at the source. Using again the relations given in Appendix A, we arrive at the following expression for $\nabla_e E$ in terms of gauge-invariant variables:

$$\nabla_e E = \frac{1}{a^2}\bar{n}^i\partial_i\left[\Psi - \mathcal{H}V - \bar{n}^j\partial_j V + \int_{\mathcal{S}}^{\mathcal{O}} d\lambda\,(\dot{\Phi} + \dot{\Psi})\right] \quad . \tag{4.11}$$

Not surprisingly, $\nabla_e E$ which vanishes on the background is a gauge invariant quantity due to the Stewart Walker lemma.

We note that the expression for the perturbed Hubble parameter (4.4) given above depends on the chosen time-slicing. So far, we evaluated all quantities at fixed time t and as such evaluated

them on hypersurfaces of constant time. However, constant time hypersurfaces are observationally not accessible; instead, we observe hypersurfaces of constant observed redshift z. Since time is related to the background redshift to first order through $t(\bar{z})$, and $z = \bar{z} + \delta z$, we have to convert the quantity $f(t)$ evaluated on constant time hypersurfaces to ones evaluated at constant redshift $f(z)$ via

$$f(t) \to f(t(\bar{z})) \equiv f(\bar{z}) = f(z - \delta z) \approx f(z) - \frac{d\bar{f}}{d\bar{z}}\,\delta z \tag{4.12}$$

to first order, where the $\bar{x}$ denotes a quantity evaluated at the background. Note that within linear perturbation theory the redshift correction term proportional to δz is only relevant for background quantities, because for first order terms, the correction would be of second order and therefore it can be neglected. As $\nabla_e E$ in the expression (4.11) for the redshift drift is already first order, its conversion gives no first order contribution and only $\mathfrak{h}$ has to be converted. According to (4.12)

$$\mathfrak{H}(t) \approx \mathfrak{H}(z) - \frac{d\bar{\mathfrak{H}}}{d\bar{z}}\,\delta z = \mathfrak{H}(z) + \left(\frac{\dot{\mathcal{H}}}{\mathcal{H}} - \mathcal{H}\right)\delta z \quad . \tag{4.13}$$

The redshift fluctuation δz was first calculated in the standard reference [37], where one can find a full derivation, and reads, neglecting observer monopole and dipole terms,

$$\delta z = -(1+z)\left[H_L + \frac{1}{3}H_T + n^i\partial_i V + \Phi + \Psi + \int_{\mathcal{S}}^{\mathcal{O}} d\lambda\,(\dot{\Phi} + \dot{\Psi})\right] . \tag{4.14}$$

Once again using gauge-invariant quantities and the relations found in Appendix A, $\mathfrak{H}(z)$ can be expressed in terms of gauge-invariant variables,

$$\begin{aligned}\mathfrak{H}(z) =& \frac{1}{a}\left\{\mathcal{H} - \dot{\Phi} - \bar{n}^i\partial_i\left(\dot{V} + 2\mathcal{H}V - \Psi\right) - \bar{n}^i\bar{n}^j\partial_i\partial_j V - \frac{\dot{\mathcal{H}}}{\mathcal{H}}\left(\Psi - \bar{n}^i\partial_i V\right) + \right.\\ &\left. + \left(\mathcal{H} - \frac{\dot{\mathcal{H}}}{\mathcal{H}}\right)\int_s^o d\lambda\,(\dot{\Phi} + \dot{\Psi})\right\} ,\end{aligned} \tag{4.15}$$

where again we neglect observer monopole and dipole terms. Finally, putting all the terms in (3.14) for the perturbed FLRW case together and neglecting observer monopole and dipole terms, we arrive at the following, manifestly gauge-invariant expression for the redshift drift as function of the observed redshift:

$$\frac{dz}{d\tau_o} = (1+z)\left[-\mathcal{H} + \dot{\Phi} + \bar{n}^i\partial_i(\dot{V} + \mathcal{H}V) + \frac{\dot{\mathcal{H}}}{\mathcal{H}}(\Psi - \bar{n}^i\partial_i V) + \left(\frac{\dot{\mathcal{H}} - \mathcal{H}^2}{\mathcal{H}} + \bar{n}^i\partial_i\right)\int_{\mathcal{S}}^{\mathcal{O}} d\lambda\left(\dot{\Phi} + \dot{\Psi}\right)\right] . \tag{4.16}$$

Note that the background terms of this expression don't coincide with (3.1), and both expressions differ by an observer monopole term $(1+z)\mathcal{H}|_{\mathcal{O}}$, but agree at the background level after the observer monopole term is neglected. Here $\frac{dz}{d\tau_o}$ is considered as a function the observed redshift z and the observed incoming direction of the photon $\mathbf{n}$.

It is worth commenting on the individual contributions. As discussed in the last section, the leading order contribution is given by the background Hubble parameter $-H_s = -(1+z)\mathcal{H}$ due to the isotropic and homogeneous expansion of the Universe, already obtained in the FLRW background expression (3.1) . The contributions proportional to $\bar{n}^i\partial_i V$ are Doppler terms arising from the source's peculiar velocity which affects the redshift, and $\bar{n}^i\partial_i\dot{V}$ is a peculiar acceleration

term. The terms involving the Bardeen potentials Φ, Ψ account for local fluctuations in the gravitational potential at the source position, whereas $\int_s^o d\lambda \left(\dot{\Phi}+\dot{\Psi}\right)$ is the integrated Sachs-Wolfe effect accounting for the time variations of the Bardeen potentials integrated along the line of sight.

In fact, we will use a slightly different expression in the next section, where the spatial derivative of the integrated Sachs-Wolfe effect is rewritten via the partial integration formula (4.7),

$$\bar{n}^i\partial_i\left[\int_s^o d\lambda\,(\dot{\Phi}+\dot{\Psi})\right] = -(\dot{\Phi}+\dot{\Psi}) - \int_s^o d\lambda\,(\ddot{\Phi}+\ddot{\Psi})\,. \tag{4.17}$$

Observer monopole terms are again neglected. This brings (4.16) to the form

$$\begin{aligned}\left.\frac{dz}{d\tau}\right|_{\mathcal{O}} = (1+z)\Bigg[&-\mathcal{H}-\dot{\Psi}+\bar{n}^i\partial_i(\dot{V}+\mathcal{H}V)+\frac{\dot{\mathcal{H}}}{\mathcal{H}}(\Psi-\bar{n}^i\partial_i V)\\ &+\frac{\dot{\mathcal{H}}-\mathcal{H}^2}{\mathcal{H}}\int_{\mathcal{S}}^{\mathcal{O}} d\lambda\left(\dot{\Phi}+\dot{\Psi}\right)-\int_{\mathcal{S}}^{\mathcal{O}} d\lambda\,(\ddot{\Phi}+\ddot{\Psi})\Bigg]\,.\end{aligned} \tag{4.18}$$

Even though this formula is a little more involved than 4.16, including two integrated terms, it will be shown to be useful as in the numerical analysis we shall neglect time derivatives of the Bardeen potentials which are known to be very small.

Expressions (4.16) and (4.18) generalize the expressions for the redshift drift including fluctuations found in the works [93, 82, 94], including all the fluctuations due to the peculiar motion of the source and structures in the Universe affecting the photon path. To show this, we pass to the Newtonian gauge and neglect peculiar motion terms, which are discarded in [93]. In this case our expression (4.16) becomes

$$\left.\frac{dz}{d\tau}\right|_{\mathcal{O}} = (1+z)\left[-\mathcal{H}+\dot{\Phi}+\frac{\dot{\mathcal{H}}}{\mathcal{H}}\Psi+\frac{\dot{\mathcal{H}}-\mathcal{H}^2}{\mathcal{H}}\int_{\mathcal{S}}^{\mathcal{O}} d\lambda\left(\dot{\Phi}+\dot{\Psi}\right)-\int_{\mathcal{S}}^{\mathcal{O}} d\lambda\,(\ddot{\Phi}+\ddot{\Psi})\right]\,. \tag{4.19}$$

By rewriting the term involving the ratio of the time derivative of the Hubble parameter in terms of the redshift and its fluctuation δz, and noting that in [93] the quantities are evaluated at constant time hypersurfaces and not constant redshift, and thus are related through (4.12), we obtain

$$\begin{aligned}\left.\frac{dz}{d\tau}\right|_{\mathcal{O}} &= -(1+z)\left[\mathcal{H}(1-\Psi)+\dot{\Psi}\right]-(1+z)\int_{\mathcal{S}}^{\mathcal{O}} d\lambda\left(\ddot{\Phi}+\ddot{\Psi}\right)-(1+z)\frac{\delta\mathcal{H}}{\delta z}\delta z\Big|_{\mathcal{S}}+(1+z)\frac{\delta\mathcal{H}}{\delta z}\delta z\Big|_{\mathcal{S}}\\ &= -(1+z)\left[\mathcal{H}(1-\Psi)+\dot{\Psi}\right]-(1+z)\int_{\mathcal{S}}^{\mathcal{O}} d\lambda\left(\ddot{\Phi}+\ddot{\Psi}\right),\end{aligned} \tag{4.20}$$

which is exactly expression (4.16) of [93] in conformal time without the observer monopole terms.

4.2. Redshift Drift Power Spectrum

As mentioned above, our next step is studying the angular power spectrum of redshift drift perturbations. In fact, we are interested in the spectra of the relative fluctuations with respect

to the background value, which characterize the contaminating effects of the redshift drift signal,

$$\begin{aligned}\delta\dot{z} &\equiv \frac{\frac{dz}{d\tau_o} - \frac{d\bar{z}}{d\bar{\tau}_o}}{\frac{d\bar{z}}{d\bar{\tau}_o}} \\ &= -\frac{1}{\mathcal{H}}\left[-\dot{\Psi} + \bar{n}^i\partial_i\dot{V} + \frac{\dot{\mathcal{H}}}{\mathcal{H}}\Psi + \left(\frac{\dot{\mathcal{H}} - \mathcal{H}^2}{\mathcal{H}}\right)\left(\int_{\mathcal{S}}^{\mathcal{O}} d\lambda\left(\dot{\Phi}+\dot{\Psi}\right) - \bar{n}^i\partial_i V\right) - \int_s^o d\lambda\left(\ddot{\Phi}+\ddot{\Psi}\right)\right],\end{aligned} \tag{4.21}$$

where $\frac{dz}{d\tau_o}$ is the redshift drift in the perturbed spacetime (4.18), and $\frac{d\bar{z}}{d\bar{\tau}_o} = -(1+z)\mathcal{H}$ the redshift drift in the background spacetime, neglecting the observer term, $H_0(1+z)$.

Because $\delta\dot{z}(\mathbf{n}, z)$ is a function of directions on the sphere, $\mathbf{n}$, we can decompose it into spherical harmonics, $Y_{\ell m}(\mathbf{n})$ in the manner described in (2.45),

$$\delta\dot{z}(\mathbf{n}, z) = \sum_{\ell,m}^{\infty} a_{\ell m}^{\delta\dot{z}}(z) Y_{\ell m}(\mathbf{n})\,, \tag{4.22}$$

where the expansion coefficients $a_{\ell m}^{\delta\dot{z}}$ are given, using equation (2.53) in real space,

$$a_{\ell m}^{\delta\dot{z}}(z) = \int d\Omega_{\mathbf{n}}\, \delta\dot{z}(\mathbf{n}, z) Y_{\ell m}^*(\mathbf{n})\,. \tag{4.23}$$

Using the Fourier decomposition (2.49), we are able to write the expansion coefficients (4.23) as

$$\begin{aligned} a_{\ell m}^{\Psi}(z_s) &= \frac{i^\ell}{2\pi^2}\int d^3k j_\ell(kr_s)\Psi(\mathbf{k}, t_s)Y_{\ell m}^*(\hat{\mathbf{k}}), & a_{\ell m}^{\dot{\Psi}}(z_s) &= \frac{i^\ell}{2\pi^2}\int d^3k j_\ell(kr_s)\dot{\Psi}(\mathbf{k}, t_s)Y_{\ell m}^*(\hat{\mathbf{k}}), \\ a_{\ell m}^{\mathbf{V}\cdot\mathbf{n}}(z_s) &= \frac{i^\ell}{2\pi^2}\int d^3k j_\ell'(kr_s)V(\mathbf{k}, t_s)Y_{\ell m}^*(\hat{\mathbf{k}}), & a_{\ell m}^{\dot{\mathbf{V}}\cdot\mathbf{n}}(z_s) &= \frac{i^\ell}{2\pi^2}\int d^3k j_\ell'(kr_s)\dot{V}(\mathbf{k}, t_s)Y_{\ell m}^*(\hat{\mathbf{k}}), \end{aligned} \tag{4.24}$$

where $\mathbf{V}\cdot\mathbf{n} = n^i\partial_i V$, and $'$ denotes derivation with respect to the argument.

Here we make use again of the assumption that the fields are Gaussian and can be obtained from the primordial spectrum through the transfer functions given in (2.74).

In practice, the transfer functions in (2.74) can be obtained in multiple ways: either numerically through Einstein-Boltzmann codes such as CLASS [104], assuming an analytical ansatz for the matter transfer function $T(k)$ such as the Eisenstein-Hu formula [105], or using one of the more recent algebraic expressions obtained through so called genetic algorithms [106]. We have checked that for our cosmological parameters, found in appendix C, the Eisenstein-Hu (EH) transfer function agrees within less than one percent with the numerical transfer function derived from the CLASS code, which is precise enough for the numerical results presented in this paper. However, for our final numerical plots we chose to modify the CLASS transfer function module originally called CLASSgal and described in detail in [41].

With a primordial spectrum given by (2.70), linked to the observed primordial spectra of the CMB through equations (2.71), we are finally able to write the power spectrum of the redshift drift fluctuations (4.16) at redshift z_s of the source, $C_\ell(z_s)$, following (2.58), as

$$C_\ell(z_s) = \frac{2A}{\pi}\int\frac{dk}{k}\left(\frac{k}{k_*}\right)^{n_S-1}|F_\ell(k, z_s)|^2, \tag{4.25}$$

where

$$F_\ell(k,z_s) = -\frac{1}{\mathcal{H}}\Bigg[j_\ell(kr_s)\left(-\dot{T}_\Psi + \frac{\dot{\mathcal{H}}}{\mathcal{H}}T_\Psi\right) + j'_\ell(kr_s)\left(\dot{T}_V - \frac{\dot{\mathcal{H}}-\mathcal{H}^2}{\mathcal{H}}T_V\right) + \frac{\dot{\mathcal{H}}-\mathcal{H}^2}{\mathcal{H}}\int_s^o d\lambda\, j_\ell(kr_s)\left(\dot{T}_\Phi + \dot{T}_\Psi\right) - \int_s^o d\lambda\, j_\ell(kr_s)\left(\ddot{T}_\Phi + \ddot{T}_\Psi\right)\Bigg] \quad . \tag{4.26}$$

In the following paragraphs, we use a modified version of CLASS in order to study the dependence of the redshift drift on redshift and angular scales, as well as its cross correlations with galaxy number count fluctuations. To that end, we apply a Gaussian window function in redshift of width $\Delta z = 0.01$ in all figures below. The numerical values for the cosmological background parameters underlying this analysis are based on the latest Planck results and are summarised in table C.1 in appendix C, in particular the amplitude A_S and spectral index n_S of the primordial power spectrum, as well as the Planck values for h, $z_{\rm eq}$, $k_{\rm eq}$, $\Omega_{\rm b}$ and $\Omega_{\rm cdm}$ which are needed for the transfer functions.

4.2.1. Power spectra at a single redshift and correlated at diffent redshifts

In Fig. 4.1 we plot the angular power spectrum as a function of redshift for some fixed multipoles, ℓ, neglecting the integrated terms in the second line of (4.26). We have checked that the integrated terms $\dot{T}_\Psi$ and $\ddot{T}_\Psi$ in (4.16) contribute less than 1% to the total power spectrum over the ℓ range of $2-300$, so we neglect them in the numerical evaluations. At redshifts $z \gtrsim 1$, the universe is matter dominated and the Bardeen potentials in (2.75) are nearly constant [20]. For low multipoles, $\ell \leq 10$, after an initial increase up to $z \simeq 0.05$, the redshift drift decays rapidly. For the higher multipoles, $\ell \geq 50$, after an initial growth the redshift drift nearly levels off.

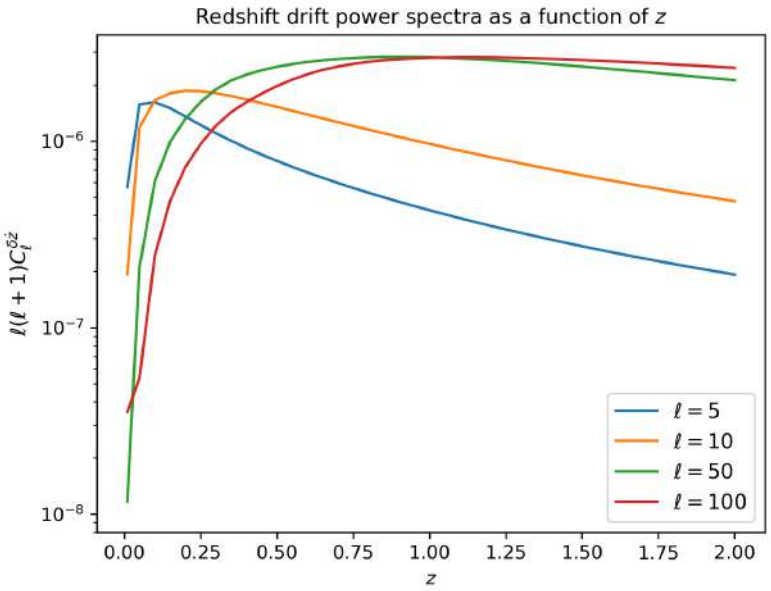

Figure 4.1.: Evolution of the perturbed redshift drift power spectra $C_\ell^{\delta\dot{z}}(z)$ as a function of redshift, for different multipoles ℓ.

We plot the full spectra for a set of redshifts and $\ell \leq 500$ in Fig. 4.2. Clearly, the perturbations are small, with amplitudes less than 10^{-3} on all scales. While the low redshift fluctuations dominate on large angular scales $\ell \lesssim 30$, the higher redshift spectra $z \geq 1$ peak at somewhat smaller angular scales, $\ell \simeq 100$.

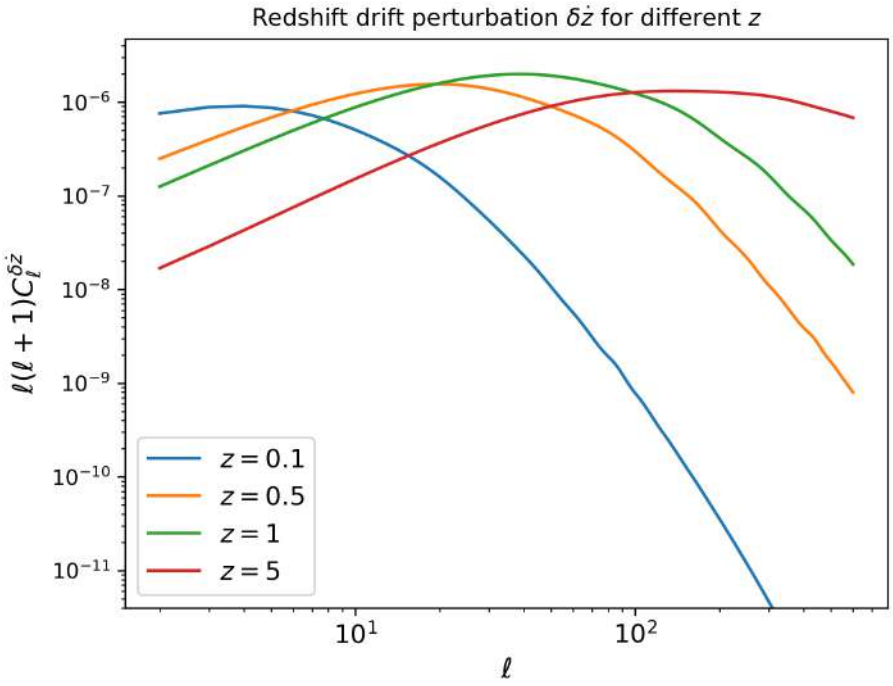

Figure 4.2.: Redshift drift perturbation power spectra for a given set of redshifts z_s and scales $\ell \leq 600$.

The dominating contribution from the peculiar velocity and acceleration terms, especially at large scales and over the redshift ranges smaller than unity highlights the importance of this term in the full gauge-invariant expression for the redshift drift (4.16), corroborating the contaminating effect estimates discussed previously and found in [82], and improving on works that neglect or discard the effect of peculiar acceleration and velocity of sources in their expression for the perturbed redshift drift [93, 100]. In Refs. [68] and [75] the authors discuss, based on the use of hydrodynamical simulations, possible astrophysical sources where the peculiar acceleration and velocity can be distinguished from the background redshift drift, aiming for an increase in the detectability of the signal. Fig. 4.3 indicates that the drift perturbations are dominated by the velocity terms at all proposed observational redshift ranges. Nevertheless, our results show that for the redshift drift signal from several sources averaged over an angular patch of a degree or more at $z = 1$ the background signal will be about 1000 times larger than the perturbations from peculiar velocities and acceleration, thus, linear perturbation theory can be trusted. Furthermore, the contribution from the potential and cross correlated terms are at least another order of magnitude smaller at all scales.

In Fig. 4.4 we show in detail the redshift dependence of each component. The V terms keep dominating at all scales, while the potential and velocity cross-correlation terms are somewhat larger at all scales for small redshifts. The dip in both of these contributions at around $z \approx 1$ comes from the pre-factor $\dot{\mathcal{H}}/\mathcal{H}$ for F_l^Ψ, see Table 4.1, which changes sign around this redshift.

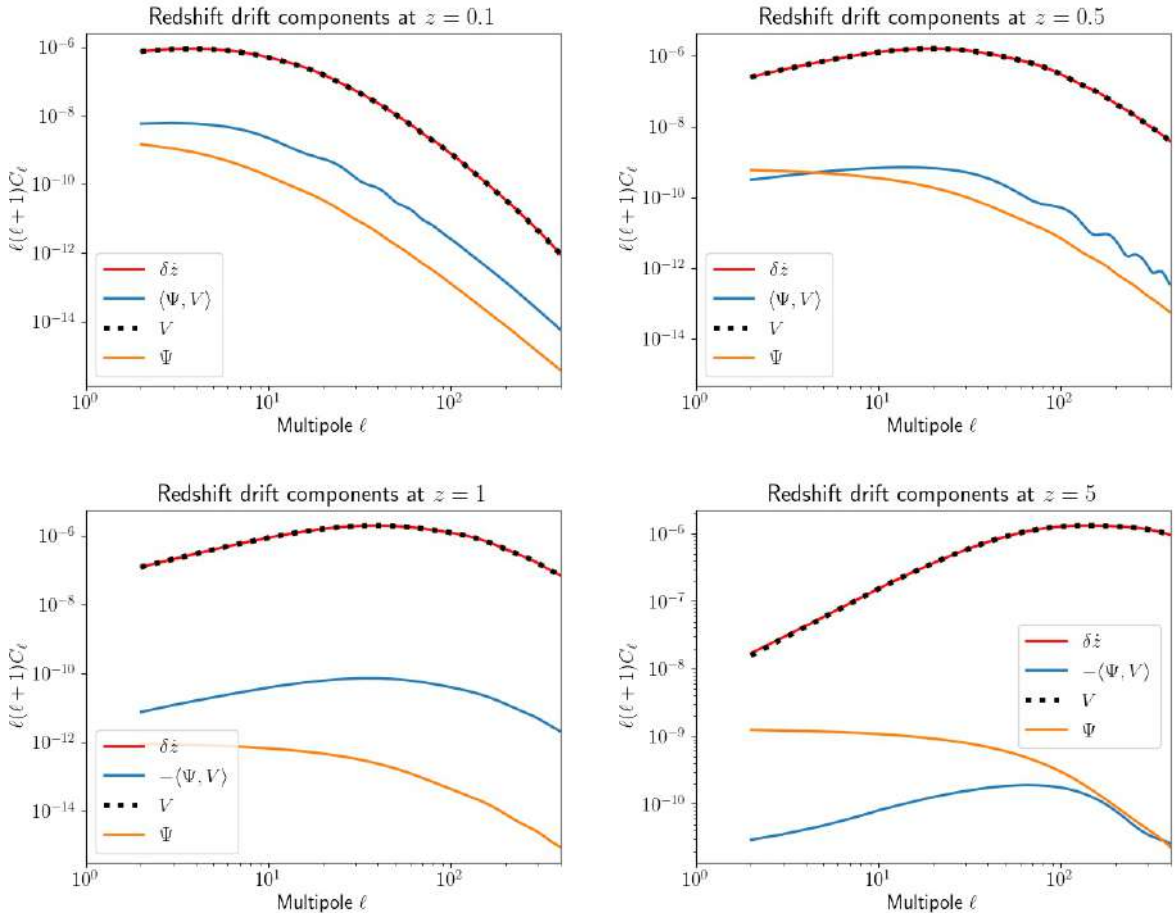

Figure 4.3.: Redshift drift and independent components angular power spectra at different redshifts as function of ℓ. The plot is in log-log scale and we use a Gaussian window function of width $\Delta z = 0.01$. The cross correlations $\langle\Psi|V\rangle$ are positive at lower redshifts ($z = 0.1, 0.5$), but turn negative at higher redshifts ($z = 1, 5$).

We have also calculated the correlation between the redshift drift spectra at different z by slightly altering (2.75) to integrate over the kernels $F_\ell(k, z)$ at different redshifts:

$$C_\ell^{\delta\dot{z}}(z_1, z_2) = \frac{2A}{\pi}\int \frac{dk}{k}\left(\frac{k}{k_*}\right)^{n_S-1} F_\ell(k, z_1)F_\ell(k, z_2), \tag{4.27}$$

while the kernels are kept the same as in the original expression.

The correlations are at most of the same order of magnitude of the power spectra measured at a single redshift signal, and in general several orders of magnitudes smaller. This small effect for non-diagonal correlations does not give any new information about the redshift dependence of the signal. In fact, the small correlations at different redshifts give support to the observational perspectives described for instance in [75, 82], where the authors enforce that measurements of the drift at different redshifts, for sources with similar spectra, should improve significantly the statistics of the measurement, particularly over the peculiar acceleration of the sources. As the correlation of perturbations from different redshifts can be safely neglected, the constraining power for the evolution of $\dot{z}$ will improve when more redshift bins are observed.

$F_\ell^V(z)$	$\frac{1}{\mathcal{H}}\left(-\dot{T}_V(k,t_s)+\frac{\mathcal{H}^2-\dot{\mathcal{H}}}{\mathcal{H}}T_V(k,t_s)\right)j_\ell'(kr_s)$
$F_\ell^\Psi(z)$	$\frac{1}{\mathcal{H}}\left(\dot{T}_\Psi(k,t_s)-\frac{\dot{\mathcal{H}}}{\mathcal{H}}T_\Psi(k,t_s)\right)j_\ell(kr_s)$
$F_\ell^V(z)\cdot F_\ell^\Psi(z)$	$\frac{1}{\mathcal{H}^2}\left(-\dot{T}_V(k,t_s)+\frac{\mathcal{H}^2-\dot{\mathcal{H}}}{\mathcal{H}}T_V(k,t_s)\right)\cdot\left(\dot{T}_\Psi(k,t_s)-\frac{\dot{\mathcal{H}}}{\mathcal{H}}T_\Psi(k,t_s)\right)j_\ell(kr_s)j_\ell'(kr_s)$

Table 4.1.: We label each component of the redshift drift power spectra in Fig. 4.3 and Fig. 4.4 according to the transfer functions inside each contribution to the total redshift drift, compare (4.26).

4.2.2. Cross-correlations with galaxy number counts

We also study the correlation between the redshift drift (2.75) and the theoretical relativistic number counts of galaxies at linear order. We again follow the standard treatment of [37], which is also manifestly gauge-invariant, for checking our predictions with forthcoming surveys and simulations. The relativistic galaxy number count fluctuation spectrum was introduced in (2.88), and

By denoting the redshift drift kernel (4.26) by $F_\ell^{\dot{z}}(k,z)$, the cross-correlation power spectrum is given by

$$C_\ell^{\delta\dot{z}N}(z)\equiv\frac{A}{\pi}\int\frac{dk}{k}\left(\frac{k}{k_*}\right)^{n_S-1}\left(F_\ell^{\delta\dot{z}}(k,z)F_\ell^N(k,z)\right). \tag{4.28}$$

We plot this cross correlation power spectrum for different redshifts in Fig. 4.5.

As we see in the figure, there is a similar behavior for all redshifts, with the absolute value of the amplitude increasing from large to intermediary scales and then flattening at smaller scales. For redshift values $z\lesssim 0.5$ however, the signals are anticorrelated for some ranges of ℓ: for $z=0.1$ the signal is strictly anticorrelated, while for $z=0.5$ the signal is anticorrelated for scales $\ell\lesssim 150$, where it changes sign. For higher values of ℓ the curves reach a maximum, respectively a minimum, at $\ell_{\max}(z)$ and have a slow decrease/increase up to highly nonlinear scales $\ell\approx 1000$, where we see a plateau between intermediate and small scales. This result is interesting because, as it has been argued in [68], that peculiar acceleration and velocities are the perturbations which are most difficult to distinguish from the cosmic background signal in future observational probes of redshift drift. Therefore, an observational probe that is correlated with the peculiar acceleration such as the number counts could provide a way to distinguish these effects from the true background signal. We notice that the maximum of the amplitude increases with redshift, such that for redshifts $z>0.5$ the curves reach it at $\ell_{\max}>100$. This behavior, and the anticorrelation for smaller redshifts, indicates that the $z\lesssim 0.5$ redshift range has a characteristic cross-correlation spectra which could possibly help to strenghten the detection of the $\delta\dot{z}$ signal through the correlation. The measured drift from sources at different redshifts in this redshift range can be correlated with the galaxy number count, and the change of sign observed in Fig. 4.5 for the same scale and different redshifts in this range could be a characteristic feature of the redshift drift signal, distinguishing it from the $\delta\dot{z}$ self-correlation power spectrum, which is strictly positive, see Fig. 4.2.

This redshift range has also been cited as promising in detecting the redshift drift precisely due to its small dependence on other cosmological probes [82]. Furthermore, the correlation amplitude is about three orders of magnitude higher than the amplitude of $\dot{z}$, as one can see by comparing Fig. 4.5 with Fig. 4.2.

Having different redshift ranges where the correlation is significant in the Λ-dominated and

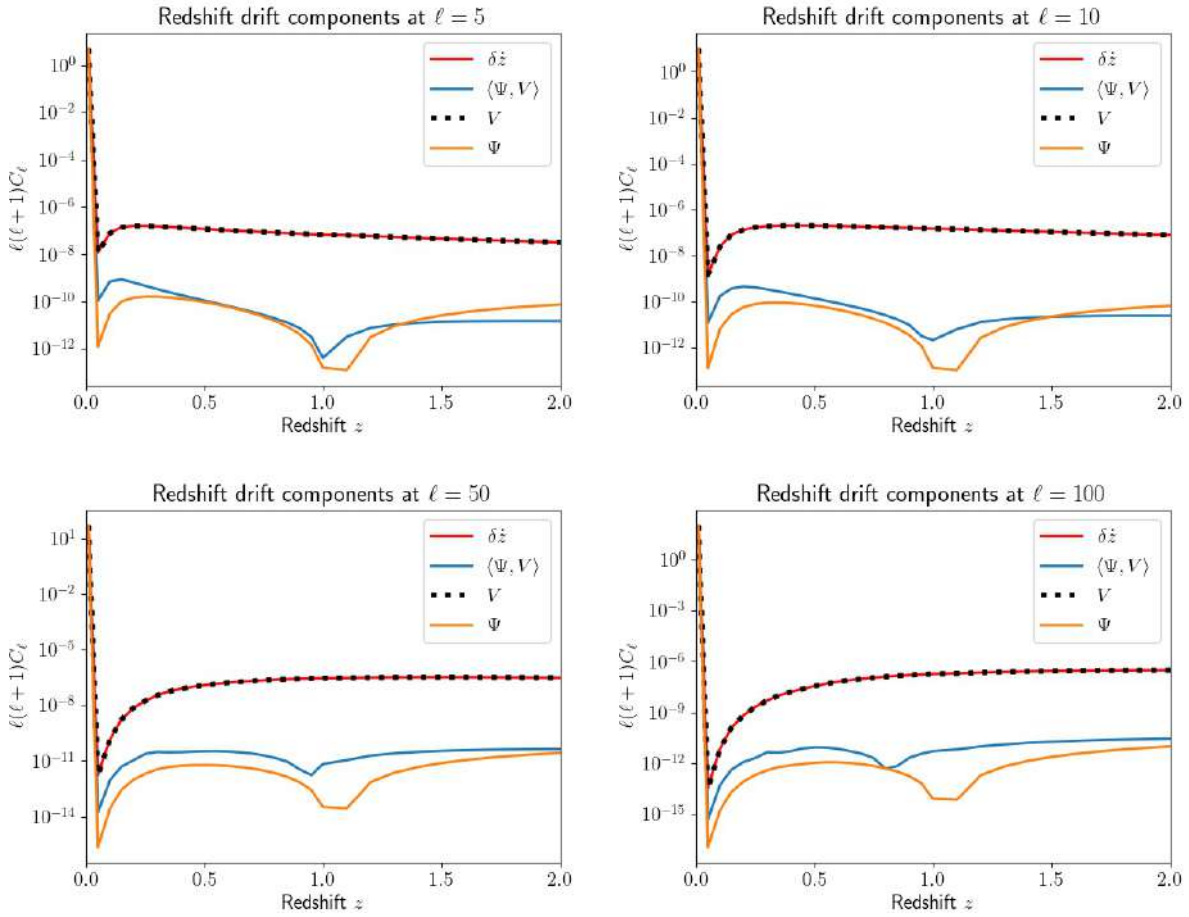

Figure 4.4.: Redshift drift and components power spectra as a function of redshift. We chose a set of ℓs to characterize the scale dependence found in Fig. 4.3.

matter-dominated eras as well as the change from anti-correlation to correlation in the transition epoch can provide additional constraints for the dark energy equation of state, as explored at the background level in [82]. The curves in Fig. 4.5 show that small scales provide the highest correlations for redshifts $z \gtrsim 0.5$, while at larger scales number count perturbations are more strongly correlated with fluctuations of the drift at lower redshifts, inside the Λ-dominated era. Furthermore, there is a change from anti-correlation to correlation as the redshift increases. This behavior may provide insight into the redshift dependence of the drift, and particularly how possible tracers of the effect should be chosen, as the sign and amplitude of the cross-correlation change, especially for smaller redshifts.

In all the cases discussed, the cross-correlation signal has a higher amplitude than the $\delta\dot{z}$ power spectra alone. On average this difference is about three orders of magnitude for all redshifts. This correlation may be useful to both strengthen the significance in the detection of the signal and to constrain the cosmological model through the redshift drift signal, such as in the case for the ISW effect [107].

The question whether this correlation signal can truly be measured in one of the proposed surveys, and if yes with which significance, however, is a more difficult question. This depends on the number density of observed sources and on the accuracy of the measurement of their redshift

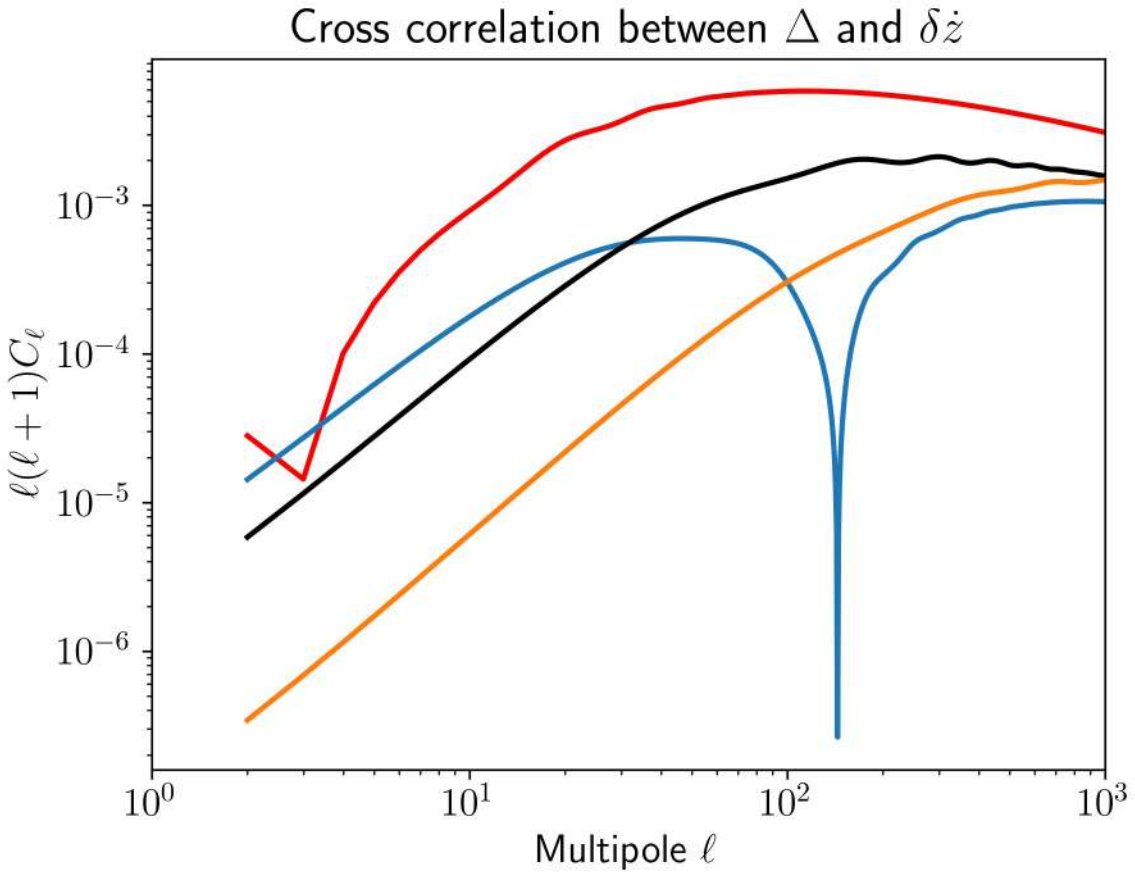

Figure 4.5.: The cross correlation $C_\ell^{\delta\dot{z}\Delta}$ of redshift drift $\delta\dot{z}$ and relativistic number count perturbations Δ as a function of ℓ for different values of redshift: $z = 0.1$ in red, $z = 0.5$ in blue, $z = 1$ in black, and $z = 5$ in yellow. The spectrum is negative for $z = 0.1$, and for $z = 0.5$ at low ℓ. For $z = 0.5$, a sign change from negative to positive happens around $\ell \approx 150$. All other spectra are positive.

drift. Nevertheless, correlating the signal with galaxy number counts is boosting it by about a factor $\sqrt{C^{\delta\dot{z}N}/C^{\delta\dot{z}}} \sim 100$. Furthermore, the cross-correlation of number counts and redshift drift does not suffer from shot noise and can provide a significant signal already with a lower number density of galaxies. A detailed calculation of the signal to noise of such a measurement for a given experiment goes beyond the present study, but forecasts with large-scale surveys such as SKA have been performed in [73, 65]

4.2.3. Summary and discussion

Our main results for the perturbed cosmic redshift drift, expressions (4.16) and (4.18), are manifestly gauge-invariant. They generalize previous expressions for the perturbed redshift drift, as found in e.g. [93, 68], and make it straightforward to derive constraints on this quantity from survey and simulation data. We expect the theoretical results to translate easily to numerical codes and simulations, as has been done in this paper through the use of CLASS.

We find that within linear perturbation theory redshift drift fluctuations are small, typically

of order 10^{-3} or smaller. Of course, a single redshift drift measurement might be strongly affected by peculiar acceleration of the source. However, averaging the measured redshift drift at fixed redshift over many widely separated directions, as proposed e.g. in [75], will yield a good measure of the background redshift drift, as in this situation the fluctuations of this mean are well-described by linear perturbation theory and the contaminating effects are all included in expression (4.16).

Nevertheless, planned measurements, e.g. with SKA2, will need $N \simeq 10^7$ galaxies in each redshift bin to reach their goal [80]. In these measurements, the authors assume that the signals from the galaxies are uncorrelated so that the total error is given by the shot noise term, $1/\sqrt{N}$. Our findings show that they have to add an effect from the correlations which is of a similar order of magnitude. More precisely, we obtain a variance from the correlations of

$$\sigma^2_{\delta z}(z) = \frac{1}{4\pi}\sum_{\ell}(2\ell+1)C_\ell(z)\,. \tag{4.29}$$

In Table 4.2 we give the values of $\sigma_{\delta z}(z)$ for some redshifts. Clearly, the correlation contribution

z	$\sigma_{\delta z}$	$1/\sqrt{N(z)}$
0.1	7×10^{-4}	1.8×10^{-4}
0.5	1×10^{-3}	3.2×10^{-4}
1	1.1×10^{-3}	1.8×10^{-3}
5	9.5×10^{-4}	?

Table 4.2.: The expected error from correlations for a full sky experiment of the redshift drift at $z = 0.1,\ 0.5,\ 1$ and 5. The expected numbers of galaxies for an SKA2 survey are taken from [80] (Fig. 2 lower panels). SKA2 only plans to measure redshift drift out to $z = 1$.

to the error is comparable with shot noise and has to be added. For the E-ELT the situation is different. They plan to measure the redshift drift much more precisely, i.e. with much smaller errors per measurement, but only for order ten lines of sight per redshift bin [74]. The shot noise contribution is then much larger, such that the correlation error is irrelevant.

The dominant contribution to first order perturbations comes from the peculiar velocity and acceleration of sources: this term is more than two orders of magnitude larger than the contribution from the gravitational potential for most redshifts, as it is seen in Fig. 4.3. Furthermore, the acceleration and potential terms are very weakly correlated. While the relevance of the peculiar acceleration and velocity of sources as perturbative effects on the cosmic redshift drift have been previously studied in the literature [68, 108], our results show for the first time the dominance of this term in comparison to other contributions to the perturbed redshift drift signal; moreover previous results have all relied on gauge-dependent derivations of the perturbed redshift drift. Here, the theoretical power spectra for the redshift drift perturbations were calculated for the first time and its numerical evaluation is presented in Fig. 4.2. The scale dependence of the effect has not been previously studied and the power spectrum prediction quantifies this, paving the way for further observational probes of the effect. We have also studied the evolution of the signal with redshift in Fig. 4.1.

Finally, we have also investigated the cross-correlation with galaxy number counts, and find significant correlations at all scales, which increases with ℓ and peaks at intermediary scales for smaller redshifts and small scales for high redshifts. In particular, for smaller redshifts $z \lesssim$

0.5, there is a change of sign from anti-correlated to correlated as the redshift increases. This correlation might help in the detection of the cosmic redshift drift fluctuations by strengthening the power spectra signal. Furthermore, the scale dependence of the cross-correlation power spectrum could point to possible astrophysical probes of the effect, such as explored in [75].

The results of this chapter lay the groundwork for the following pages, where we model a measurement of the redshift drift power spectrum (4.25) using n-body simulations in a ΛCDM cosmological model.

Redshift Drift fluctuations from n-body simulations

The results of chapter 4 clarify the main perturbative effects in a redshift drift measurement, as well as providing a theoretical estimate of the contaminating effects to test against future observations. Our implementation of the redshift drift fluctuations power spectrum in (4.25) using CLASS provides a basis for the validation of future observations of the power spectrum and different numerical implementations, such as using fully relativistic codes, as done for instance in [109], where the authors calculated the redshift drift fluctuation power spectrum from simulations using the Einstein Toolkit numerical relativity code, in an Einstein-de Sitter background.

In scenarios where direct observational data is limited or lacking, simulations and numerical implementations provide a controlled framework to test hypotheses and explore the effects of various cosmological parameters on a given effect or observable. In the context of modeling redshift drift observations, simulations using survey mock data are explored in [110], and numerical relativity simulations in the work mentioned above [109]. The use of n-body simulations to model observations of the redshift drift and its fluctuations was first explored in [91, 100], where the authors model cosmic inhomogeneities using a LTB metric, and calculate its impact on the average redshift drift measurement. The EdS background is a good approximation for the background metric for redshifts $z > 1$, such that the impact of the Λ term is not relevant to structure formation. Our implementation of the fluctuations power spectrum using CLASS in chapter 4 is the first in the literature in the context of ΛCDM cosmologies, and also the first obtained with the use of Einstein-Boltzmann codes.

There is a lack of direct modeling of the cosmic drift effect, its fluctuations and its power spectra through n-body simulations in the full perturbed ΛCDM setting, including peculiar velocity and acceleration effects, which will be of fundamental importance for validation and testing of future observational data, along with the previously mentioned simulations using full numerical relativity and mock data. n-body simulations are also able to probe non-linear scales usually not implemented in Einstein-Boltzmann codes, which allow comparison and testing of the validity of linear perturbation theory in modeling the effect. n-body simulations can also provide an estimate of the shot-noise involved in real surveys, as well as an estimate of the redshift drift fluctuation distribution field over the sky.

The `gadget4` n-body code [111] provides easy to implement fully non-linear, accurate, parallelizable code to simulate ΛCDM cosmologies through Newtonian simulations, including full structure formation up to non-linear scales. This allows us to process the simulation outputs into the distribution of fields in the sky, which in turn allows us to calculate, using the simulated data, the redshift drift fluctuations (4.18) and its power spectrum (4.25) from these fields. In this chapter, we shall use n-body simulations obtained from the `gadget4` code to derive the observed

power spectra of redshift drift fluctuations (4.25), obtain an estimation of its distribution over the sky and validate the results against the implementation in `CLASS`.

First we detail the main approximations and assumptions used to derive the power spectra from the simulation, based on the results obtained in the previous chapter.

Secondly, we describe our simulation setup and the implementation of the redshift drift fluctuations spectra numerically using the outputs from the simulations.

Finally, we compare our results to the implementation in the CLASS code. We end by discussing our results and contextualizing its impact on the literature and our work in the previous chapter.

This chapter follows closely an in preparation pre-print containing the results of this work which will soon be available online. Much of the text and results found here shall overlap with the final published paper [15].

5.1. Approximations and observed Power Spectra

Our numerical findings in chapter 4 show that the time dependent potential terms in equation (2.75) give a very small contribution to the overall redshift drift signal, 2 orders of magnitude smaller than the effects arising from the peculiar motion of source. We neglect these terms when implementing the power spectra numerically, such that the expression for the redshift drift fluctuation power spectra is given by

$$C_\ell^{\delta\dot{z}}(z_s) = \frac{2A}{\pi}\int \frac{dk}{k}\left(\frac{k}{k_*}\right)^{n_S-1}|F_\ell(k,z_s)|^2, \tag{5.1}$$

where the Kernel $F_\ell(k,z_S)$ is given by

$$F_\ell(k,z_s) \approx -\frac{1}{\mathcal{H}}\left[j_\ell(kr_s)\left(\dot{T}_\psi + \frac{\dot{\mathcal{H}}}{\mathcal{H}}T_\Psi\right) + j'_\ell(kr_s)\left(\dot{T}_V - \frac{\dot{\mathcal{H}}-\mathcal{H}^2}{\mathcal{H}}T_V\right)\right],$$

where once again the j_ℓ are the spherical bessel functions of order ℓ, and r_S is the comoving radial distance from the observer to the source.

In order to properly derive the theoretical prediction (4.25) using n-body simulations, the definition of the power spectrum of a field in the sky (2.52) needs to be slightly modified, such that one doesn't have a perfect map, as expected, between the observed and the theoretical power spectrum. In surveys and modeling through simulations, the observed power spectrum comes from an observed fraction of the sky at a given redshift slice Δz, particular to the capabilities of the survey and simulation. The observed power spectrum P^X_{obs} is then related to the theoretical power spectrum through a window function (2.90) that projects the full sky spectrum onto the observed region.

Newtonian n-body simulations have been shown to properly model relativistic inhomogeneous FLRW Universes at linear order, where in the longitudinal gauge the metric potentials (2.33) and the peculiar velocities (2.27) map directly to the Newtonian gravitational potential ψ and the particles' peculiar velocity vector v_i [112]. To obtain the Power Spectra at different redshifts from the `Gadget4` simulations, we follow this correspondence, formalized in the dictionary between relativistic and Newtonian cosmologies explored in [112].

The actual observed linear power spectrum P^X_{obs}, for a given 3D field X is its 2D sky-projected power spectrum at redshift z_0. Denoting the projected field by $\Delta(\mathbf{n}, z_0)$, we have

$$\Delta(\mathbf{n}, z_0) = \int_0^\infty dr W(r) X(r\mathbf{n}, \eta_0 - r), \tag{5.2}$$

where r is the comoving distance and $W(r)$ a window function, which encodes the projection of the field at redshift z_0 and comoving distance $\eta_0 = \int_0^{z_0} dz/H(z)$.

The dimensionful observed power spectrum of this field is then given by [24]

$$P^X_{\text{obs}}(k, z) = \frac{2\pi^2}{k^3} |\Delta(k, z)|^2, \tag{5.3}$$

where we implicitly performed a Fourier decomposition on $\Delta(k, z)$ and averaged over the sphere with unit vector $\mathbf{n}$.

The observed angular power spectrum at redshift z of the field X is related to its power spectrum through the expressions [24]

$$C^X_\ell(x) = \frac{2}{\pi} \int_0^\infty dk k^2 P^X_{\text{obs}}(k, z) W^2_{r,\ell}(k) = 4\pi \int_0^\infty \frac{dk}{k} \Delta^2(k, z) W^2_{r,\ell}(k), \tag{5.4a}$$

$$W_{r,\ell}(k) = \int_0^r d\bar{r} W(\bar{r}) j^{(i)}_\ell(k\bar{r}), \tag{5.4b}$$

where $W(\bar{r})$ is an arbitrary window function used to filter a certain range of redshifts or scaled, and $j^{(i)}_\ell$ is the i-th derivative of the spherical Bessel function j_ℓ, which appear in the Fourier transform of direction dependent fields $X(\mathbf{n})$.

By taking the field X to be the redshift drift fluctuation, the observed linear angular power spectrum of the redshift drift derived from an n-body simulation is given by

$$C^{\delta\dot{z}}_\ell(x) = 4\pi \int_0^\infty \frac{dk}{k} \Delta^2(k, z) W^2_{r,\ell}(k) \tag{5.5}$$

$$\Delta(k, z) = \mathcal{F}\left[-\frac{1}{\mathcal{H}} \left[-\dot{\psi} + \mathbf{n} \cdot \dot{\mathbf{v}} + \frac{\dot{\mathcal{H}}}{\mathcal{H}} \psi - \left(\frac{\dot{\mathcal{H}} - \mathcal{H}^2}{\mathcal{H}} \right) \mathbf{n} \cdot \mathbf{v} \right] \right], \tag{5.6}$$

where we used the mapping between the relativistic Bardeen potential Ψ and the Newtonian potential ψ, and between the relativistic 4-velocity v^μ of the observed and the peculiar velocity of particles $\mathbf{v} = (v_x, v_y, v_z)$. $\mathcal{F}$ denotes the 3D Fourier transform of the field, and $\mathbf{n}$ is the unit vector on the sphere.

We further simplify expression (5.5) by neglecting the potential terms, which are at least an order of magnitude smaller than the velocity terms, to arrive at the final expression for the angular redshift drift power spectrum, given by

$$C^{\delta\dot{z}}_\ell(x) = 4\pi \int_0^\infty \frac{dk}{k} \Delta^2(k, z) W^2_{r,\ell}(k), \quad W_{r,\ell}(k) = \int_0^r d\bar{r} W(\bar{r}) j'_\ell(k\bar{r}), \tag{5.7}$$

$$\Delta(k, z) = \mathcal{F}\left[-\frac{1}{\mathcal{H}} \left[\mathbf{n} \cdot \dot{\mathbf{v}} - \left(\frac{\dot{\mathcal{H}} - \mathcal{H}^2}{\mathcal{H}} \right) \mathbf{n} \cdot \mathbf{v} \right] \right]. \tag{5.8}$$

For scales $\ell \gg 1$ it is usual to adopt the Limber approximation, which we detail in appendix D.1. Using this approximation, (5.4a) can be further simplified to

$$C^X_\ell(x) = \frac{2}{\pi} \int_0^\infty \frac{dk}{k} \Delta^2(k, z) W^2_{r,\ell}(k) \approx \frac{1}{(\ell + 1/2)^3} \int d\bar{r} \bar{r} \Delta^2\left(\frac{\ell + 1/2}{\bar{r}}, z\right) W^2(\bar{r}). \tag{5.9}$$

For distance modes satisfying $\ell \gtrsim \ell_c = \bar{r}/\Delta\bar{r}$ the Limber approximation has been shown to be accurate to smaller than 1% accuracy levels in comparison to the fully integrated power spectra [24, 20]. We shall make use of this approximation as a consistency check when validating the simulations.

We furthermore use a top-hat window function, which filters modes outside of the slice we select from the simulation snapshot, with comoving size $\Delta\bar{r}$. Modes k such that $\ell \gtrsim \frac{k\Delta\bar{r}}{2\pi\bar{r}}$ are integrated out of the angular power spectra. The explicit form of this window function is given by

$$W_r(\bar{r}) = \begin{cases} 1/\Delta r & \text{for } r_1 < \bar{r} < r_2, \qquad \Delta r = r_2 - r_1 \\ 0 & \text{otherwise .} \end{cases} \tag{5.10}$$

One can also interpret the window function above as selecting fluctuations inside the redshift slice $\Delta z \approx H(z)\Delta r/c$ centered on the redshift z.

This window function, when inserted in equation (5.9) allows one to further simplify the observed angular power spectrum expression in the Limber approximation large scales. By selecting a small distance slice $\Delta\bar{r}$ of the observed cosmic region, we have

$$C_\ell^X(z) \approx \frac{1}{(\ell+1/2)^3}\int d\bar{r}\bar{r}\Delta^2(\frac{\ell+1/2}{\bar{r}},z)W^2(\bar{r}) \xrightarrow{\Delta\bar{r}/\bar{r}\ll 1} \frac{\ell_c}{(\ell+1/2)^3}\Delta^2(\frac{\ell+1/2}{\bar{r}},z). \tag{5.11}$$

Equation (5.11) allows simple implementation of the the theoretical power spectrum (5.4a), and although we use the `FFTlog` routine to calculate the integrals [113], at smaller scales the Limber approximation provides consistency check for the numerical power spectra.

We note that approximations (5.9) and (5.11) are valid for integrals containing no derivatives of the Bessel functions, such as for the potential terms in (5.1). In the final expression (5.7) the Limber approximation is not a good approximation due to the different oscillating behavior of the spherical Bessel function derivatives.

5.2. Power Spectra from n-body simulations

To model the observed linear Power Spectra of the redshift drift fluctuations (5.7) we perform a Newtonian n-body simulation using the `Gadget4` massively parallel code. Our simulation was run on a 1Gpc/h Box with 1024^3 particles and initial conditions were generated via the built-in NGEN-IC Initial Condition generator, generated at redshift $z = 49$, and the particle mass and softening ϵ_{soft} can be found in table C.2. We produced 3 snapshots at the redshifts $z = 0.5$, 1, 2, and used the cosmological parameters as found in appendix C. For the window function, we use a redshift slice of $\Delta z = 0.1$ and a top-hat window function, which corresponds to a comoving size of $0.1c/H(z)Mpc$ for the projected field in equation (5.4a)

We validate our simulations by deriving the matter Power Spectrum $P(k)$ and the galaxy number count angular power spectrum C_ℓ^N [37] from the snapshots, using the same pipeline as the redshift drift power spectrum and angular power spectrum, and compare it to the numerical spectra obtained from CLASS. We The validation can be found in appendix D. The complete list of cosmological parameters used in the simulation and Einstein-Boltzmann solvers can be found in appendix C.

The derivation of the power spectrum from the particle fields in the snapshots is done using the Pylians package for numerical simulation analysis in python [114]. We read the snapshots

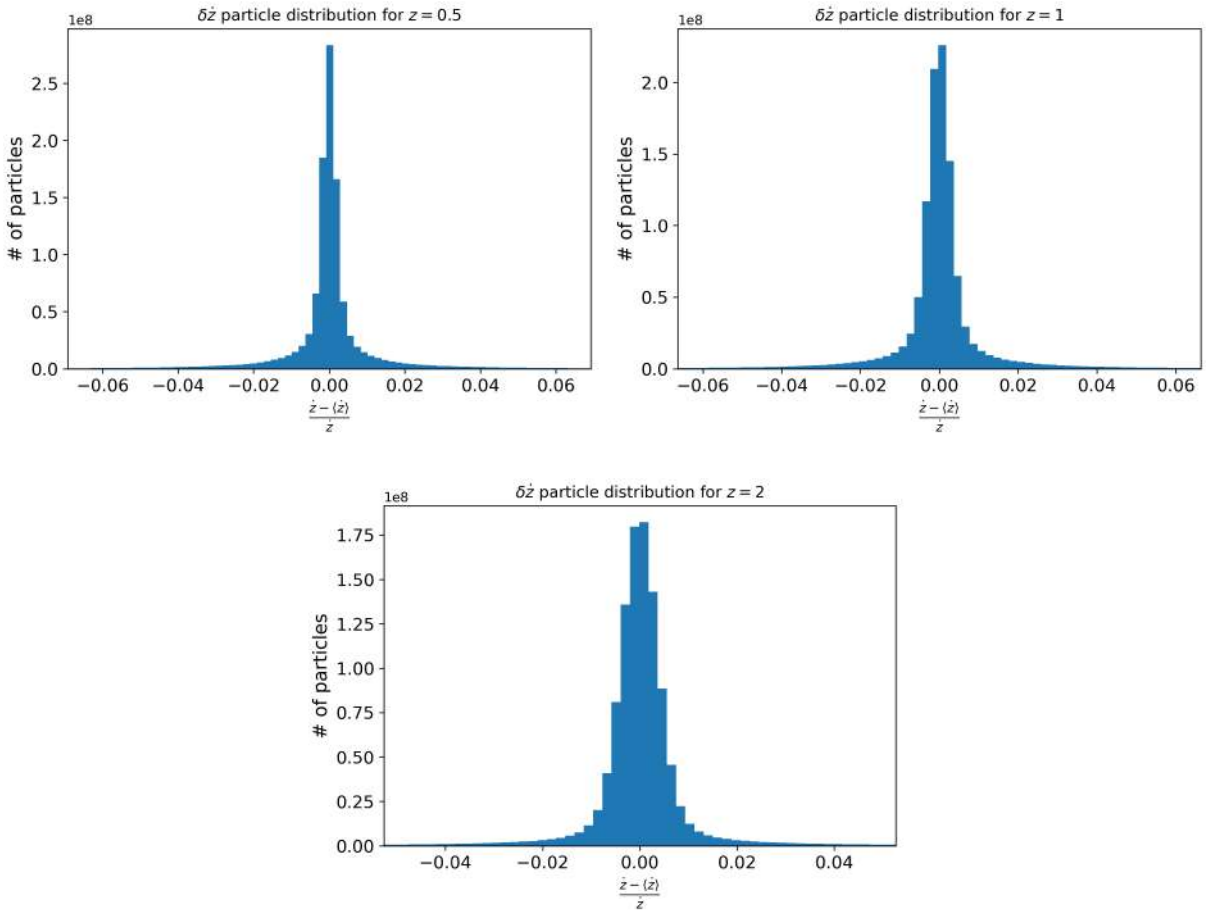

Figure 5.1.: Histogram for the redshift drift fluctuations in the simulation box for redshifts $z = 0.5$, 1, 2. The distribution is nearly gaussian with standard deviation $\sigma \approx 2 \cdot 10^{-2}$ for all redshifts.

in HDF5 format and use a triangular shaped cloud mass assignment scheme implementation in Pylians to obtain the fields. To generate a 3D array of the redshift drift field, we discard potential terms in (4.21) and use the same expression to derive the drift expression from the acceleration and velocity fields. We calculate the particle density field of each snapshot and divide the full redshift drift field by the particle density field, in order to obtain the redshift drift density field, where, for empty voxels, we assign a density of $\rho = 1$. The amount of empty voxels is less than 100 in a total of 2^{30} voxels, which do not affect the final statistics. We then subtract the average redshift drift in the snapshot from the redshift drift field and divide by the same average to obtain the redshift drift fluctuations (4.21). We plot the redshift drift fluctuation distribution histogram in figure 5.1 for the three redshifts analyzed, which provide a glimpse at the gaussianity and amplitude of the fluctuations.

In obtaining the power spectrum we make use of the flat-sky approximation, where one assumes the direction vector $\mathbf{n}$ on the sphere is approximated by a vector α, where α is a 2D coordinate vector in the plane perpendicular to the observer's reference direction. This is equivalent to choosing a reference axis z in the simulation box as being the observer direction, as well as assuming that the box size corresponds to a sizeable fraction of the celestial sphere. We further

detail this approximation in appendix D.1, while noticing that for big enough box sizes it provides an accurate estimate of the angular power spectrum [115]. The power spectrum is then calculated using the `Pk_library` from Pylians.

The 3D Fourier transforms of the velocity field and derivatives present in equation (5.7) are obtained using standard routines of the Pylians library, which calculates the dimensionful power spectrum (5.3) of the fields, and we numerically integrate equation (5.7) using the `FFTlog-and-beyond` python library for integrals containing Hessel and spherical Bessel functions and derivatives [113].

To avoid resolution effects due to a finite Box size, we restrict our spectra to modes $k \in [2k_{\text{fund}}, k_{\text{Nyq}}/2]$ and angular correlations with modes $\ell \in [\frac{2k_{\text{fund}}r(z)}{(1+z)}, \frac{k_{\text{Nyq}}r-1/2}{(1+z)}]$, above the fundamental frequency $k_{\text{fun}} = 2\pi/\text{Box Size}$ and below the Nyquist frequency $k_{\text{Nyq}} = N_{\text{particles}} \times k_{\text{fun}}$.

We plot the adimensional power spectra $|\Delta^2(k, z)|$ of the redshift drift and the vertical lines corresponding to modes inside the interval $[2k_{\text{fund}}, k_{\text{Nyq}}/2]$ in figure 5.2.

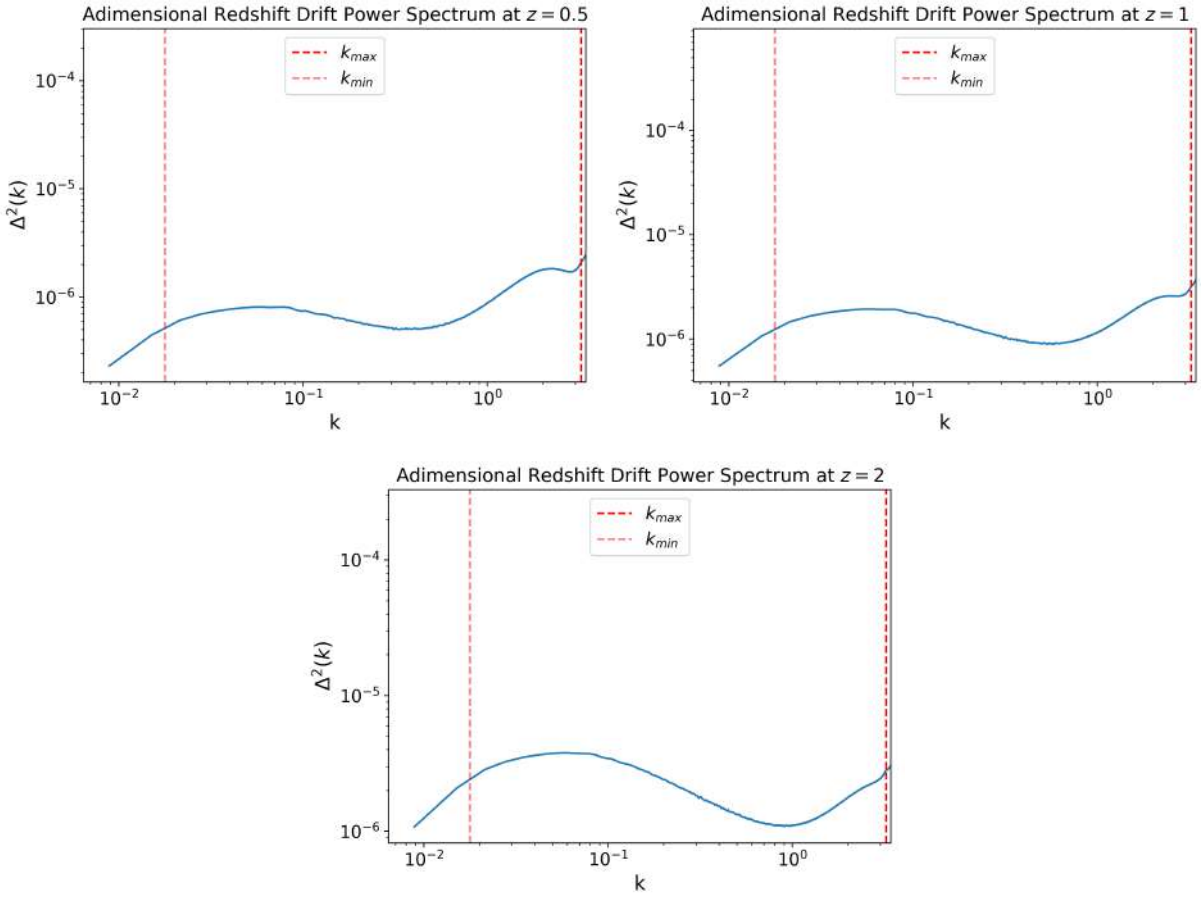

Figure 5.2.: Adimensional Redshift Drift power spectra $|\Delta^2(k)|$ for snapshots taken at redshifts $z = 1, 2, 3$. The minimum and maximum allowed modes k_{min} and k_{max} are given by $2k_{\text{fund}}$ and $k_{\text{Nyq}}/2$ respectively.

One can see an increase in the power spectra at higher modes for all redshifts due to resolution effects at smaller scales, close to the Nyquist frequency. The effect becomes more pronounced at smaller redshifts, as objects become more clustered and we may find voxels with a very small number of particles. As these effects are not physical, we cut off the power spectrum of the

fluctuations at these scales when integrating equation (5.7).

We see that the amplitude of the redshift drift fluctuations peak at $|\delta| \sim \sqrt{\Delta^2} \lesssim \mathcal{O}(10^{-2})$ for all redshifts $z \geq 1$, and are not smaller than 10^{-4}. This result is in agreement with the results found in section 2 of chapter 4 and around two orders of magnitude higher than the results found in [100], which also used a Newtonian simulation to obtain an estimate of the fluctuation amplitude. We note that the results in [100] are based on an Einstein-de Sitter background cosmology, such that some of the discrepancy can be attributed to the effect of both the background cosmology and structure formation in ΛCDM, which is known to be slower due to the late time acceleration.

5.2.1. Comparison with CLASS and discussion

To test our results against the CLASS Einstein-Boltzmann solver, we take into account the numerical and sampling errors arising in power spectra derived from n-body simulations, which are not unlike the observational errors that arise in cosmological surveys. The intrinsic cosmic variance error of angular correlations of fields in the sky, due to a smaller sample size for bigger fractions of the celestial sphere, is given by the variance of the angular spectrum C_ℓ, and one can write it as a function of the mode ℓ as [20]

$$\sigma_\ell = \sqrt{\frac{\langle (\bar{C}_\ell - C_\ell)^2 \rangle}{C_\ell^2}} = \sqrt{\frac{2}{2\ell + 1}}, \tag{5.12}$$

where $\bar{C}_\ell$ is the theoretically predicted C_ℓ and $\langle C_\ell \rangle$ the average over the sphere. This variance is intrinsic to the fact that we are sampling a finite amount of regions in the sky, fewer regions for larger scales. In the case of simulations this error is underestimated, due to the finite size of the simulation box representing only a fraction of the actual celestial sphere, and this discrepancy is more pronounced at the largest scales, since modes larger than the simulation box are not included in the calculation.

One also needs to take into account the shot noise due to finite resolution and a discrete sampling of a field modeled as a continuous distribution over the sky. Assuming the distribution of the fluctuations is gaussian, the noise can be approximated by poissonian noise, given by [116, 20]

$$SN = \frac{1}{n_S}, \qquad n_S \equiv \frac{N_g}{\Omega}, \tag{5.13}$$

where N_g is the number of galaxies in the measured redshift slice and Ω is the area of the sky covered by the box size at redshift z in steradians, given by $\Omega = \frac{(1+z)^2 H_0^2}{r(z)^2} Gpc^2$, $r(z)$ the comoving distance for our Box Size. For $N_{\text{particles}} = 1024^3$ and the cosmic parameters given in table C.1, the values of the shot noise and the intrinsic variance can be found in table 5.1. In our case, we take $N_g = N_{\text{particles}}$, which is unrealistic when compared to a large scale survey such as SKA, where the observed shot noise is predicted to be $SN \sim 10^{-7}$ [80], although such a resolution provides enough accuracy to probe smaller scales, beyond what was studied in chapter 4 using the CLASS code.

In table 5.1, along with the shot noise, we give an upper limit on the intrinsic variance of the angular correlations by redshift, given by (5.12) at the largest scales $\sigma_\ell \approx 2$ and the average order of magnitude of the spectra, seen in figure 5.3. It's clear that the shot noise has negligible contribution to the overall variance of the angular power spectrum, and the observation error can be modeled safely by including only the intrinsic cosmic variance of the spectra. We note again

that the variance error given in table 5.1 actually underestimates the variance error due to the finite box size.

Redshift	$\sigma_\ell(\ell = 2)$	SN
0.5	$\geq 4.4 \cdot 10^{-8}$	$1.18 \cdot 10^{-12}$
1	$\geq 4.4 \cdot 10^{-8}$	$1.55 \cdot 10^{-12}$
2	$\geq 4.4 \cdot 10^{-8}$	$2.53 \cdot 10^{-12}$

Table 5.1.: Intrinsic variance and shot noise for the analyzed redshifts.

The total variance in the angular power spectra obtained from the simulation snapshots is then given by the intrinsic variance plus the shot noise [20]

$$\delta C_\ell = \sqrt{\frac{2}{2\ell + 1}} \left(C_\ell + \frac{1}{n_S} \right). \tag{5.14}$$

The modified CLASS code used to generate the angular power spectrum $C_\ell^{\delta \dot{z}}$ works strictly within linear perturbation theory, such that nonlinear effects are not taken into account in the redshift drift power spectra. Since our simulations are fully Newtonian, deviations from linearity at smaller scales are present, and the slope of the angular spectrum is modified in relation to the linear spectra generated with CLASS. We normalize the spectra derived from the simulations based on (5.7) to the convention used in [41] to properly compare the amplitude of the n-body angular spectra to the amplitude predicted by CLASS. This convention can be found in appendix C for reference.

In figure 5.3 we plot both the spectra obtained from the simulations and the spectra generated using the CLASS implementation of the redshift drift fluctuations spectra. We find an agreement within an order of magnitude between both spectra at all scales, with a greater agreement at smaller scales.

Previous works on the amplitude and angular power spectrum of the redshift drift fluctuations, using both Newtonian n-body simulations [100] and fully relativistic simulations [109], found a difference of more than two orders of magnitude for the amplitude of the fluctuations in relation to the CLASS implementation found in section 2 of chapter 4. The general scaling of the curve found in the paper, of an increase at small scales $\ell \lesssim 10$ up to a peak at intermediary scales $\ell \approx 10^2$ and a monotonic decrease at scales $\ell \gtrsim 10^2$ matches the behavior of the curves in figure 5.3 and section 2 of chapter 4. Further simulations, using both relativistic and Newtonian codes and the same cosmological parameters and background, are needed in order to settle on the amplitude of the spectra and its scale dependency. Although the results seem to converge on the scaling behaviour of the fluctuations of the redshift drift, one needs an accurate estimate on the amplitude of the contaminating effects to use the simulation spectra against future observations.

From the plots in figure 5.3 one can see that the peak of the signal obtained from the simulations is slightly moved to the right in relation to the CLASS curve for $z = 2$, whereas it strictly decreases for other redshits; it also has a slightly different asymptote at small and large scales. The change in the maximum of the curves and the monotonic decrease can be attributed to the different numerical methods used to calculate the power spectra and the different implementation of the window function. Where the CLASS code calculates the the integral (5.7) through the transfer functions, our code uses the `FFTlog` routine to numerically select the redshift slice where we perform the integration, given the power spectrum. At large scales the change in the asymptote can be attributed to the mask selecting modes greater than the fundamental frequency, which

may filter relevant modes that fall inside the redshift slice used; at small scales the nonlinear behavior of structure formation should alter significantly the behavior in relation to the linear approximations implemented in the CLASS code, particularly for smaller z's where nonlinearities are more pronounced.

The order of magnitude agreement between our results and the results found in chapter 4 also support the approximations done in (5.1) and (5.7) to arrive at the final expression for the spectra. The non integrated potential terms, which are included in the analysis done in the previous chapter, can be safely neglected in relation to the dominant acceleration and velocity terms, at all scales, and the agreement within an order of magnitude shows that even if our results are taken as an order of magnitude estimation of the drift fluctuations, potential terms have no impact in the observations.

In the ΛCDM case, our work points to an effect of at most order 10^{-7} in relation to the background redshift drift for angular correlations, in agreement with both the results of chapter 4 and [91]. With respect to the order of magnitude and size of the effects, our work converges with the literature, where a precision of $\Delta\dot{z}/\dot{z} \sim 10^{-3}$ is needed in order to measure such fluctuations. Nevertheless, even in our idealized simulation setting, we were able to constrain the amplitude and scaling of the power spectrum of the drift fluctuations through observations of the cosmic velocity and acceleration fields, which together with the galaxy number count spectra, as discussed in section 2 of chapter 4 , could help in detecting a statistical significant signal of the drift by constraining contaminating effects due to the peculiar motion of sources.

5.3. Summary and discussion

In this chapter we derive the Redshift Drift Power Spectrum at different redshifts from an n-body simulation run using the `gadget4` code. To obtain the power spectrum from the simulation, we model it using the theoretical prediction from the previous chapter and numerically calculate it using the velocity and acceleration fields from the `gadget4` snapshots and power spectrum and FFT routines found in the Pylians and FFTlog-and-beyond python libraries. We validate our code and simulation using the Einstein-Boltzmann solver CLASS, and once validated, compare our results to the numerical predictions obtained using the same code as in chapter 4. Our work provides a methodology for modeling the redshift drift using n-body simulations and derive one and two point statistics from simulation data.

Our findings show an agreement with the numerical implementation of the redshift drift spectra using the CLASS code to within an order of magnitude, with a signal that increases from large to intermediary scales for all redshifts and peaks at scales $\sim \mathcal{O}(10^2)$, and strictly decreases afterwards, up to scales $\ell \sim 10^3$. Our results also show a peak of the signal at the same scales as the CLASS implementation and an overall agreement with the scale behavior found in chapter 4. Previous works using n-body simulations to model a measurement of the redshift drift and its fluctuations find a disagreement of more than 2 orders of magnitude the results of this thesis, although the authors assumed a different cosmological background and energy content. Further work assuming the same background cosmologies is needed in order to properly compare the results from different numerical simulations of the effect.

Our work agrees with previous literature in that measuring the fluctuations on the drift significantly impacts the observation of the background effect, in particular in measuring the velocity and acceleration fields distribution over the sky. Although of order 10^{-3} on the background drift, which is already small, it is within the capabilities of surveys such as SKA, as discussed in the last section of chapter 4 and [109].

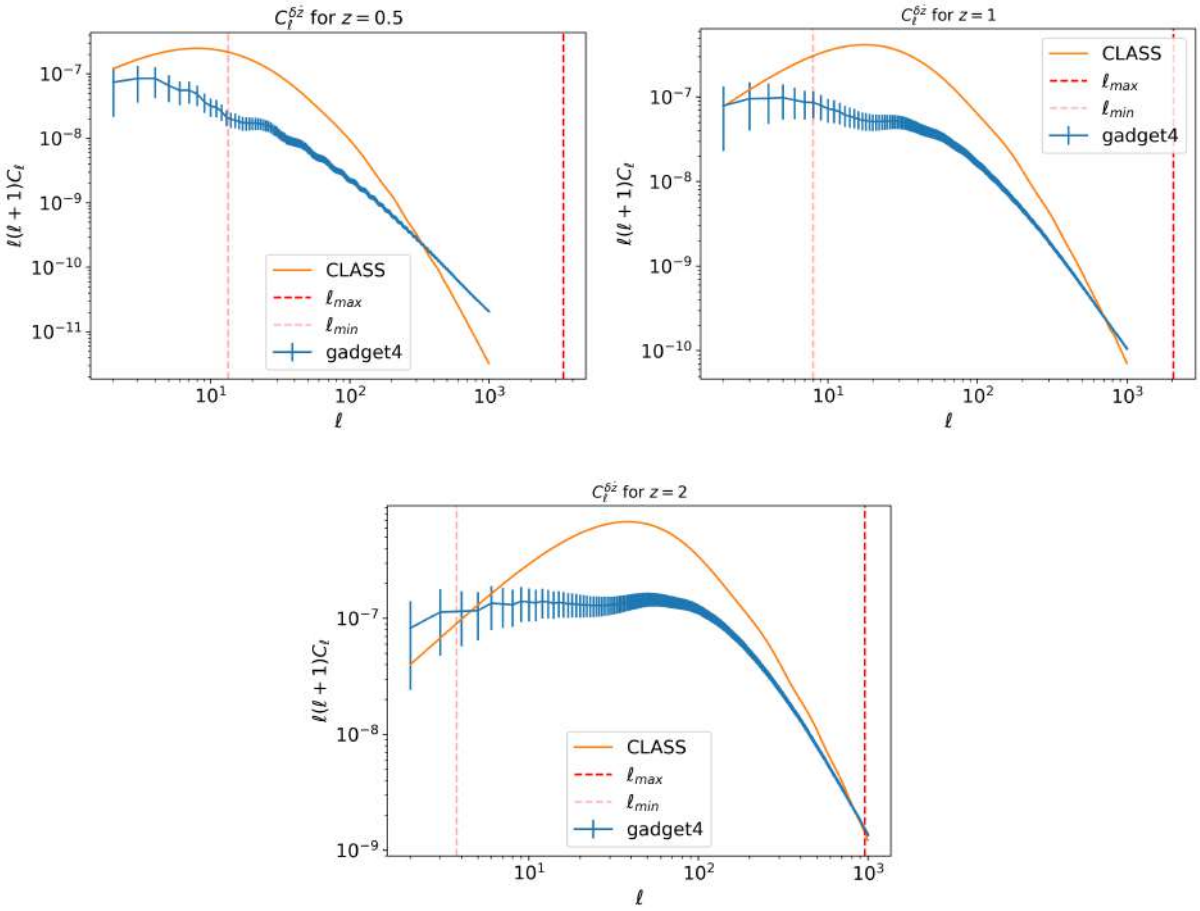

Figure 5.3.: Redshift drift fluctuations angular power spectra for redshifts $z = 0.5, 1, 2$. The light and bold dashed lines are the minimum and maximum scales respectively, with accuracy within the simulation interval $k \in [k_{\text{fund}}, k_{Nyq}/2]$. The orange line is the prediction for the angular power spectrum using the implementation in the CLASS cosmology code.

At last, our simulation assumes an idealized dark matter plus Λ only Universe, with structure formation and peculiar motion of sources with no baryonic effects or feedback, and a simulation box size of 1Gpc. The SKA radio telescope will have a sky coverage of 75% and probe redshifts $z \in [0, 0.5]$ in the radio, HI and 21cm regions, observing baryonic feedback in regimes previously unseen. Larger simulations, including baryonic and hydrodinamic effects in structure formation and the momentum fields are to be done in order to prepare for the upcoming observational challenge in measuring the drift with next generation surveys. Such a task is beyond the current computational capabilities of this work, and we leave it for future research.

Conclusions and Discussion

In this thesis we provided an introduction to the theoretical and observational aspects of the cosmic redshift drift and the Sandage-Loeb test in cosmology. We reviewed the main observational programmes to measure the effect and the current theoretical developments in the literature. More specifically, we detailed the current objective of performing the Sandage-Loeb test with SKA and ELT [73, 3] and current forecasts based on these surveys; and provided an introduction to the theoretical work done in extending the redshift drift definition to general spacetimes and the possibility of using it as a model independent probe of the late time cosmic acceleration paradigm, including possible violations of the strong energy condition [9, 96, 95, 101].

The objective of the thesis was to extend the previous work done on fluctuations of the redshift drift to include all of the perturbative effects, in order to properly make sense of the contaminating effects due to the peculiar motion of sources and growth of structure in the Universe. Previous work lacked a unified description and relied on ad-hoc calculations, which omitted part of the perturbative effects found in our main result, equations (4.18) (4.25). We also aimed at implementing our theoretical results in codes established in the cosmology literature, and providing a solid basis for future theoretical and observational research done on the redshift drift in ΛCDM cosmology and beyond, and a reference work for a full gauge-invariant treatment of perturbative effects on the redshift drift.

Based on these objectives, our main results in this thesis, based on the works [10, 15], are the derivation for the first time of a gauge-invariant expression for the full perturbed redshift drift in an perturbed FLRW cosmology, the expression for its power spectra as a function of redshift and its implementation in the Einstein-Boltzmann code CLASS, as well as an implementation and validation of these results using n-body simulations done with the `gadget4` code. We find that the main contributions to the redshift drift fluctuations come from the peculiar velocity and acceleration terms in equation (4.18), which are 2 orders of magnitude larger than the potential effects, which can be safely neglected in further works. We also correlated the redshift drift fluctuation signal and the galaxy number count signal to understand if the latter could help enhance the detection of the drift fluctuations and improve the possibility of detection. We found an increase of up to 100 in the amplitude of the angular power spectra of the signal when correlated with the galaxy distribution power spectra, and thus opened the possibility of using galaxy counts in surveys as a way of increasing the detection of the redshift drift fluctuations and help in constraining the background value.

We find an agreement within an order of magnitude between the implementations using the CLASS code and the spectra obtained from simulations using the `gadget4` code, and the scaling and redshift evolution of the curves for the angular power spectra match. The different routines used to calculate the window functions and the finite box effects in the simulations can account for some of the difference between the observed spectra, and further validation, with larger and

more involved simulations, is needed in order to settle on the amplitude of these fluctuations.

Our results show contaminating effects of order 10^{-3} from both the Einstein-Boltzmann code implementation and n-body simulations, as well as the same redshift and scaling behavior for the power spectra and the angular power spectra. Our results have a more than two orders of magnitude difference in relation to the results for the amplitude of the fluctuations found in the works [100, 109], although it must be noted that the background cosmology assumed in these works is that of an Einstein-de Sitter one, whereas we assume a ΛCDM model. Although a good approximation for cosmic eras with redshift $z \gtrsim 1$, the redshift range explored in these works is also different from the one studied here, focusing on $z \leq 0.5$. Thus, the differences between our results and these works could be due to a difference in background cosmology and structure formation, which has different dynamics in matter-only cosmologies.

6.1. Future Research

Our work opens up the possibility of using n-body simulations and Einstein-Boltzmann codes to model the future detection of the redshift drift with SKA and the ELT. Bigger simulations, including baryonic effects and using window functions based on the capabilities of the telescopes used in these surveys could provide accurate predictions for the spectra which future observations could use to model contaminating effects in measurements of the drift.

Furthermore, the possibility of using measurements of the redshift drift not only as tests of the late-time acceleration of the Universe, but of cosmic homogeneity and isotropy as well, is a current research topic. Important work has been done in understanding the behavior of the redshift drift and its average in LTB universes [91, 100, 109] using EdS backgrounds, with both n-body simulations and fully relativistic codes. The BEHOMO collaboration has recently released a set of snapshots of n-body simulations in ΛLTB cosmologies [117], inhomogeneous cosmological models including a cosmological constant. Performing measurements of the redshift drift in such simulations and constraining its contaminating effects could further establish the drift as an independent test of cosmic acceleration, and distinguishing between the backreaction hypothesis and the existence of a cosmological constant. This work along with [100] are the first in an important program to model the redshift drift in realistic cosmologies through simulations, beyond naive estimations.

Finally, the Sandage-Loeb test is not the only proposal to measure the redshift drift and observe real-time cosmology for the first time. Measuring the redshift difference due to the gravitational time delay in images of strongly lensed quasars could provide a measurement of the cosmic drift at the quasar's redshift [61, 118, 82, 119, 120]. Proposals for measurements of this instantaneous redshift difference from strong gravitational lensing observations using Euclid and the James Webb space telescope have been proposed, although extensive work on the theoretical modeling of contaminating effects due to lens models and line of sight effects, in the same way as done for the Sandage-Loeb test in this and other works, is needed in order to properly understand how gravitational lensing could probe real-time cosmology through the redshift drift. This is another path for exploring redshift theory and observation.

Gauge-Invariant Cosmological Perturbations

In this appendix we give the full expression for all gauge-invariant variables used throughout the text, and the transformation laws of the metric and tensor functions in a linear perturbed FLRW Universe. For a more detailed account of their derivation we refer to [20].

The main gauge-invariant quantities are the Bardeen potentials Φ and Ψ, the velocity perturbation V, and the gauge-invariant matter density perturbation D, given in terms of the perturbed quantities found in chapter 2 by

$$V = v - \dot{H}_T\,, \qquad D = \delta + 3(1+w)\mathcal{H}V, \tag{A.1}$$

$$\Psi = A - \mathcal{H}\sigma_t - \dot{\sigma}_t\,, \qquad \Phi = -\mathcal{R} + \mathcal{H}\sigma_t. \tag{A.2}$$

The scalar metric functions transform under gauge transformations parametrized by $\mathcal{L}_X = T\partial_t + L^i\partial_i$, such that under gauge-transformations they are given by

$$A \to A + \mathcal{H}T + \dot{T} \tag{A.3}$$

$$B \to B - \dot{L} + 3\nabla T \tag{A.4}$$

$$H_L \to H_L + \mathcal{H}T - \nabla L \tag{A.5}$$

$$H_T \to H_T + \nabla L \tag{A.6}$$

We also explicit these useful relation between the variables:

$$\mathcal{R} = H_L - \frac{1}{3}\Delta H_T \quad , \tag{A.7}$$

$$\sigma = -V = \dot{H}_T - v \quad , \tag{A.8}$$

$$\sigma_t = \dot{H}_T - B \quad , \tag{A.9}$$

$$V = v - B - \sigma_t \quad . \tag{A.10}$$

Note that while $\sigma = -V$ is gauge invariant, $\mathcal{R}$ and σ_t are not. The denote the spatial curvature and the shear on the $t =$ constant hypersurface and therefore depend on the chosen time-slicing.

Definitions and special functions

In this appendix we provide mathematical definitions for statistical quantities and variables mentioned throughout the text, as well as the definition of special functions. Rigorous definitions and theorems can be found e.g. in references [121, 20, 122, 36]

B.1. Statistical Definitions

B.1.1. Random variables and distributions

Given a random variable X, uniquely defined by its probability distribution function (PDF) $P(x)$ or its probability density $p(x)$ in the positive real numbers $\mathbb{R}^+$

$$P(X < x) \equiv \int_{-\infty}^{x} dx' p(x') \,, \qquad \int_{-\infty}^{\infty} dx' p(x') = 1. \tag{B.1}$$

one defines its average $\langle X \rangle$ and variance σ_x by

$$\langle X \rangle = \int_{-\infty}^{+\infty} dx x p(x) \tag{B.2a}$$

$$\sigma_X^2 = \langle (X - \langle X \rangle)^2 \rangle = \int_{-\infty}^{+\infty} dx (x - \langle X \rangle)^2 p(x). \tag{B.2b}$$

A random variable X given by the Gaussian distribution has probability density function, average and variance given by

$$\begin{aligned} p(x) &= \frac{1}{2\pi\sigma} e^{-\frac{1}{2}\left(\frac{x-\mu}{\sigma}\right)^2} \\ \langle X \rangle &= \mu, \\ \sigma_X^2 &= \sigma^2. \end{aligned} \tag{B.3}$$

In the Poisson distribution case, with parameter λ, a discrete random variable X has probability mass function, average and variance given by

$$p(k) = \frac{\lambda^k e^{-\lambda}}{k!}, \tag{B.4}$$

$$\langle X \rangle = \sigma_X = \lambda. \tag{B.5}$$

The Central Limit Theorem states that for samples $X_1, X_2, ..., X_n$ of a random variable X with average μ and positive finite variance σ, the distribution of the sample average minus the average $\langle X_n \rangle - \mu$ with normalized variance $\sigma/\sqrt{n}$, converges to the Gaussian distribution with mean 0 and variance 1, also called the Normal distribution.

We can write the statement as [121]

$$\sqrt{n}\left(\frac{\langle X_n \rangle - \mu}{\sigma}\right) \xrightarrow{p} \mathcal{N}(0,1), \tag{B.6}$$

meaning that the density distribution function p of the random variable $\sqrt{n}(\langle X_n \rangle - \mu)$ converges to the Normal distribution $\mathcal{N}(0,1)$ as $n \to \infty$.

The Central Limit Theorem allows one to approximate random distributions with finite variance and average as a Gaussian distribution for large enough sample sizes. An immediate corollary is that the Gaussian distribution approximates the Poisson distribution for large enough n.

B.1.2. Multivariate distributions and correlations

Given two random variables X, Y given by probability distribution functions with finite means μ_X, μ_Y and variances σ_X, σ_Y, we define their covariance $Cov(X,Y)$ and correlation $C(X,Y)$ as

$$Cov(X,Y) \equiv \langle (X - \mu_X)(Y - \mu_Y) \rangle = \langle XY \rangle - \mu_X \mu_Y \tag{B.7}$$

$$C(X,Y) \equiv \frac{Cov(X,Y)}{\sigma_X \sigma_Y} = \left\langle \frac{(X - \mu_X)}{\sigma_X} \frac{(Y - \mu_Y)}{\sigma_Y} \right\rangle. \tag{B.8}$$

We note that the correlation $C(X,Y)$ is padronized, such that it has image in the set $[-1,1]$ [121]. For a collection of n random variables $X_1, ..., X_n$, one can define the covariance matrix Σ, encoding information about the variables joint distribution, by

$$\Sigma = \begin{pmatrix} \sigma_{X_1} & \sigma_{X_1 X_2} & \cdots & \sigma_{X_n X_1} \\ \sigma_{X_1 X_2} & \sigma_{X_2} & \cdots & \sigma_{X_n X_2} \\ \cdots & \cdots & \cdots & \cdots \\ \sigma_{X_1 X_n} & \sigma_{X_2 X_n} & \cdots & \sigma_{X_n} \end{pmatrix} \tag{B.9}$$

An n-dimensional vector of random variables $\mathbf{X} = (X_1, X_2, ..., X_n)$ is then a vector in $\mathbb{R}^n$ where each coordinate is given by a random variable, or equivalently, with coordinates given by a collection of random variables.

For a given confidence interval $\Delta\chi^2$ of n measurements $\hat{X}_1, ..., \hat{X}_n$, modeled by a collection of n random variables $X_1, ..., X_n$, the Figure of Merit (FoM) is defined as

$$\text{FoM} \equiv \frac{1}{\det \Sigma \cdot \Delta\chi^2}, \tag{B.10}$$

where Σ is the covariance matrix of the collection. The figure of merit, in a sense, measures the significance of the uncertainties on the measured variables, using their joint measurement uncertainties and the confidence interval. Smaller uncertainties (in this case, variances and covariances) mean higher figures of merit, as do smaller confidence intervals. It is extensively used in

A n-dimensional vector of random variables $\mathbf{X}$ is called a multivariate gaussian random vector if its joint probability density $p : \mathbb{R}^n \mapsto \mathbb{R}$ is given by

$$p(\mathbf{X}) = \frac{1}{\sqrt{(2\pi)^n \det(\Sigma)}} \exp\left(-\frac{1}{2}\mathbf{X}^T\Sigma^{-1}\mathbf{X}\right). \tag{B.11}$$

This definition allows us to define a gaussian random field by assigning to each point $\mathbf{n}$ in a given space a gaussian random variable X via the map $F : S \to X : \mathbf{n} \mapsto X(\mathbf{n})$. In the case of cosmology, we usually take the space S to be the celestial sphere, with direction vector $\mathbf{n}$.

A random field is called gaussian then if for any two vectors $\mathbf{n}_1$ and $\mathbf{n}_2$, the fields $X(\mathbf{n}_1)$ and $X(\mathbf{n}_2)$ have joint probability distribution given by (B.11). The correlation function of such random fields involves a functional integral and we refer the reader to [20] for a derivation of the correlation function in the case of statistically homogeneous and isotropic fields, such as the ones studied in chapter 2.

B.2. Special Functions

In the text we make extensive use of two classes of special functions when dealing with the power spectra of fields: Legendre Polynomials and spherical Bessel functions. Here we provide a brief review of their definitions and relations, in particular to the spherical harmonic expansion of fields on the sphere.

The Legendre polynomials are the set characteristic solutions $P_\ell(x)$ of the Legendre differential equation

$$\frac{d}{dx}\left[(1-x)^2\frac{df}{dx}\right] + \ell(\ell+1)f = 0, \tag{B.12}$$

where $\ell \in \mathbb{N}$, for each ℓ. Legendre polynomials satisfy the Rodrigues formula, where they can be obtained by the simple expression

$$P_\ell(x) = \frac{1}{2^\ell \ell!}\frac{d^\ell}{dx^\ell}(x^2-1)^\ell. \tag{B.13}$$

The Legendre polynomials form a complete orthogonal set of polynomials, satisfying the orthogonality relation

$$\int_{-1}^{1} P_\ell(x)P_m(x)dx = \begin{cases} 0, & \text{if} \ell \neq m \\ \frac{2}{2\ell+1}, & \text{if} \ell = m. \end{cases} \tag{B.14}$$

The Bessel functions of the first kind are a set of functions that form a solution space to the Bessel ordinary differential equation

$$\frac{d^2f}{d^2x} + \frac{1}{x}\frac{df}{dx} + \left(1 - \frac{m^2}{x^2}\right), \tag{B.15}$$

where $m \in \mathbb{R}$, and the solution is written

$$f(x) = c_1 J_m(x) + c_2 J_{-m}(x), \tag{B.16}$$

where c_1, $c_2 \in \mathbb{R}$. The Bessel functions of the first kind satisfy the recurrence relations

$$J_{m+1}(x) + J_{m-1}(x) = \frac{2m}{x} J_m(x), \tag{B.17}$$

$$J_{m+1}(x) - J_{m-1}(x) = -2\frac{dJ_m(x)}{dx}, \tag{B.18}$$

and, given $m \in \mathbb{Z}$, satisfy the formula

$$J_m(x) = x^m \left(-\frac{1}{x}\frac{d}{dx}\right)^m J_0(x). \tag{B.19}$$

Again for integer m, the following relation for vectors $\mathbf{k}$ and $\mathbf{x}$, with $\mathbf{k} \cdot \mathbf{x} = kx\sin(\theta)$ is extensively used:

$$e^{i\mathbf{k}\cdot\mathbf{x}} = \sum_{m=-\infty}^{\infty} e^{im\theta} J_m(kx). \tag{B.20}$$

The spherical harmonics of order $_{\ell m}$ are the fundamental solutions of the spherical part $Y(\theta, \phi$ of the EDP

$$(\Delta + \ell(\ell+1))\,[R(r)Y(\theta,\phi)] = 0, \tag{B.21}$$

where the Laplacian operator Δ is given in spherical coordinates. The solutions can be given explicitly by

$$Y_{\ell m}(\theta,\phi) = \sqrt{\frac{2\ell+1}{2\pi}\frac{(\ell-m)!}{(\ell+m)!}} P_\ell^m(\cos\theta) e^{im\phi}, \tag{B.22}$$

where we note the relation with expansion (B.20) in the above expression.

The spherical Bessel functions are solutions to the Bessel equation (B.15) with half integer coefficients $m = \ell + 1/2$, such that solutions are of the form

$$y(x) = C_1 \frac{J_{\ell+1/2}(x)}{x^{1/2}} + C_2 \frac{J_{-\ell-1/2}(x)}{x^{1/2}}. \tag{B.23}$$

The spherical Bessel functions are then defined, with normalization factor $\sqrt{2/\pi}$

$$j_\ell(x) = \sqrt{\pi/2x} J_{\ell+1/2}(x), \tag{B.24}$$

for $\ell \in \mathbb{Z}$. In the $\ell = 0$ case we have $j_0(x) = \sin(x)/x$, and we obtain the simple formula , as in the Bessel case,

$j_\ell(x) = x^\ell \left(-\frac{1}{x}\frac{d}{dx}\right)^\ell \left(\frac{\sin(x)}{x}\right)$.

Constants, Numerical Values and Conversion Factors

In this appendix we provide tables with the numerical values and parameters used throughout the text, mainly in the numerical implementation of the redshift drift power spectrum and n-body simulations.

As the `gadget4` code works with internal code units, one needs to convert from internal units to physical units and then map these fields to the physical fields found in equation (4.25) through the conversion factors. We list the conversion factors and units used throughout the paper in the following table, and refer the reader to the `gadget4` documentation at https://wwwmpa.mpa-garching.mpg.de/gadget4/#documentation for a comprehensive list of the conversion factors.

Furthermore, the CLASS code outputs the angular power spectra of fields X using the convention

$$\frac{\ell(\ell+1)}{2\pi}C_\ell^{XX} = \left(\frac{\ell(\ell+1)}{2\pi}\right) 4\pi \int \frac{dk}{k} |\Delta_\ell^2(k,z)|, \tag{C.1}$$

where $|\Delta^2(k,z)$ is given by the $|F_\ell|^2$ in expression (5.1).

Parameter	Value	Units
Ω_b	0.022383	h^{-2}
Ω_{CDM}	0.12011	h^{-2}
h	0.7	$10^{-2}\text{km}/s/Mpc$
A_S	$2.100549 \cdot 10^{-9}$	-
n_S	0.9660499	-
z_{eq}	3387	-
k_{eq}	0.010339	$h/\text{M}pc$

Table C.1.: Planck 2018 data release best fit values for ΛCDM.

Parameter	Value	Units
$N_{\text{particles}}$	1024^3	-
m_{part}	10^{10}	$\text{M}_\odot$
Box Size	$1 \cdot 10^3$	Mpc
Grid Size	1024	-
ϵ_{soft}	0.024	h$/Mpc$
Ω_b	0.022383	h^{-2}
Ω_{CDM}	0.12011	h^{-2}
h	0.687	$10^{-2}\, km/s/Mpc$
n_S	1	-
z_{eq}	3387	-
k_{eq}	0.010339	$h/$Mpc
σ_8	0.8	-
Δz	0.05	-

Table C.2.: Parameters used to generate the n-body simulation and numerical spectra through Einstein-Boltzmann solvers.

Simulation field [`gadget4` units]	Physical field [physical units]	Conversion factor
$h\,[10^{-2}\,\text{km}/s/Mpc]$	$H\,[\text{km}/s/Mpc]$	10^{-2}
$\mathbf{v}\,[cm/s]$	$\mathbf{v}\,[\text{km}/s]$	$10^{-5} \cdot a^{1/2}$
$\mathbf{a}\,[\text{km}^2/s^2/(Mpc/h)]$	$\dot{\mathbf{v}} + H\mathbf{v}\,[\text{km}/s^2/Mpc]$	$h \cdot (\text{km}/s)^{-1}$

Table C.3.: Fields given in simulation units and physical units, and conversion factor from simulation to physical units.

n-body simulation validation and approximations for Power Spectra

D.1. Approximations

D.1.1. Limber

The Limber approximation makes use of the fact that the spherical Bessel functions $j_\ell(x)$ peak around $x = (\ell(\ell+1))^{1/2} \approx \ell+1/2$ [123]. For large ℓ, this peak is even more pronounced, such that one may take $j_\ell(x) \xrightarrow{\ell\gg1} \sqrt{\frac{\pi}{(\ell+1/2)}}\delta(x-\ell-1/2)$, such that, for a function $f(k) = \int dx' f(x') j_\ell(kx')$, we have

$$\int_0^\infty dk f(k) = \int_0^\infty \int dk dx' f(x') j_\ell(kx') \approx \int_0^\infty dk f(\ell + \frac{1}{2}). \tag{D.1}$$

This approximation has been used extensively on scales $\ell \gtrsim \mathcal{O}(10)$ for cosmological angular correlations, including in CLASS [41].

D.1.2. Flat sky

In the flat-sky approximation we assume that we are observing a small enough area of the sky such that the curvature of the celestial sphere can be neglected. More precisely, we substitute the spherical coordinates over the whole celestial sphere by

$$\mathbf{n} = r(z)(\theta, \phi) \longrightarrow \mathbf{e_z} = r(z)(x, y), \tag{D.2}$$

where $\mathbf{e_z}$ is the unitary vector in a given coordinate in the simulation box, assumed to be the observer or survey reference direction, and (x, y) are 2D coordinates in the plane perpendicular to $\mathbf{e_z}$. For small scales, this approximation is very accurate, as smaller areas of the sky are less affected by curvature effects. In this approximation, the modes ℓ are conjugate to the coordinates $\alpha = (x, y)$, such that they are related by a 2D Fourier transform. In [115] the authors show that the accuracy for self correlations and modes $\ell > 2$ at a given redshift is within 0.3% of the numerical accuracy of the CLASS code for galaxy number counts, well beyond the needed accuracy for the derived Power Spectra in our work.

D.2. Validation

We validate our simulations against the Einstein-Boltzmann solver at both linear and nonlinear level using the `halofit` routine implemented in CLASS. To do so, we derive the matter power

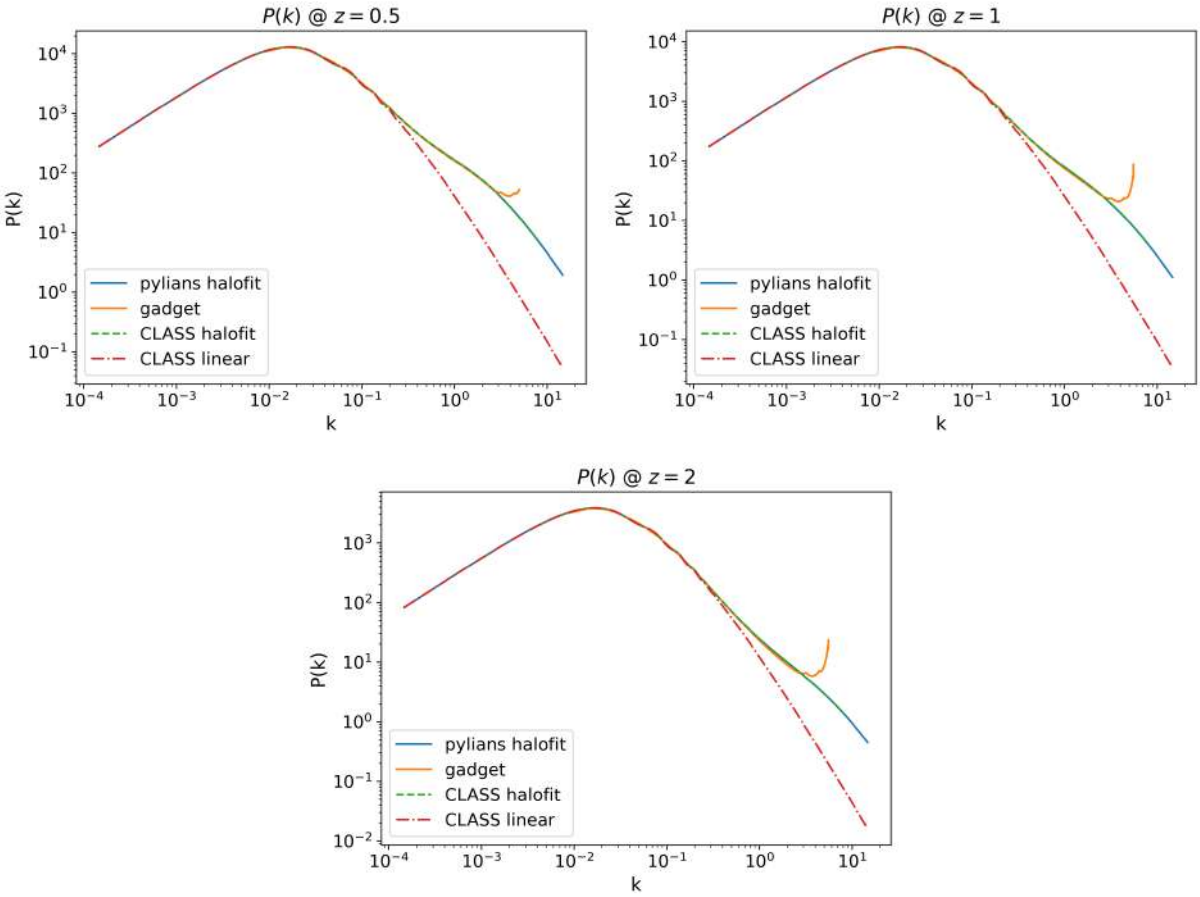

Figure D.1.: Matter power spectra for redshifts $z = 0.5\,, 1,\, 2$. In the figures we compare three routines agains the power spectra obtained from the `gadget4` simulations: using the halofit routine found in pylians, using the halofit routine found in CLASS and using the linear matter power spectrum from CLASS, which is given as input for the halofit in the pylians routine.

spectra from the simulation using the same prescription as used for the redshift drift power spectrum in chapter 5, with snapshots at redshifts $z = 0.5,\, 1\,, 2$, calculate the matter power spectrum using the halofit routine found in the `pylians` library, and test them against the linear and nonlinear matter power spectra derived from CLASS. We plot the results in figure D.1. The curves obtained from the simulations match the expected behavior.

To validate the routines we use to calculate the angular power spectra (5.7) using the `FFTlog-and-beyond` python library and the CLASS implementation, we also test the angular power spectrum of density counts against the linear and nonlinear galaxy number count angular power spectrum from CLASS, by using the same window function and redshift slice. We also plot the Limber approximation as a consistency check for the angular power spectra derived from gadget. The results are shown in figure D.2. The curves all match the expected behavior at linear and nonlinear scales.

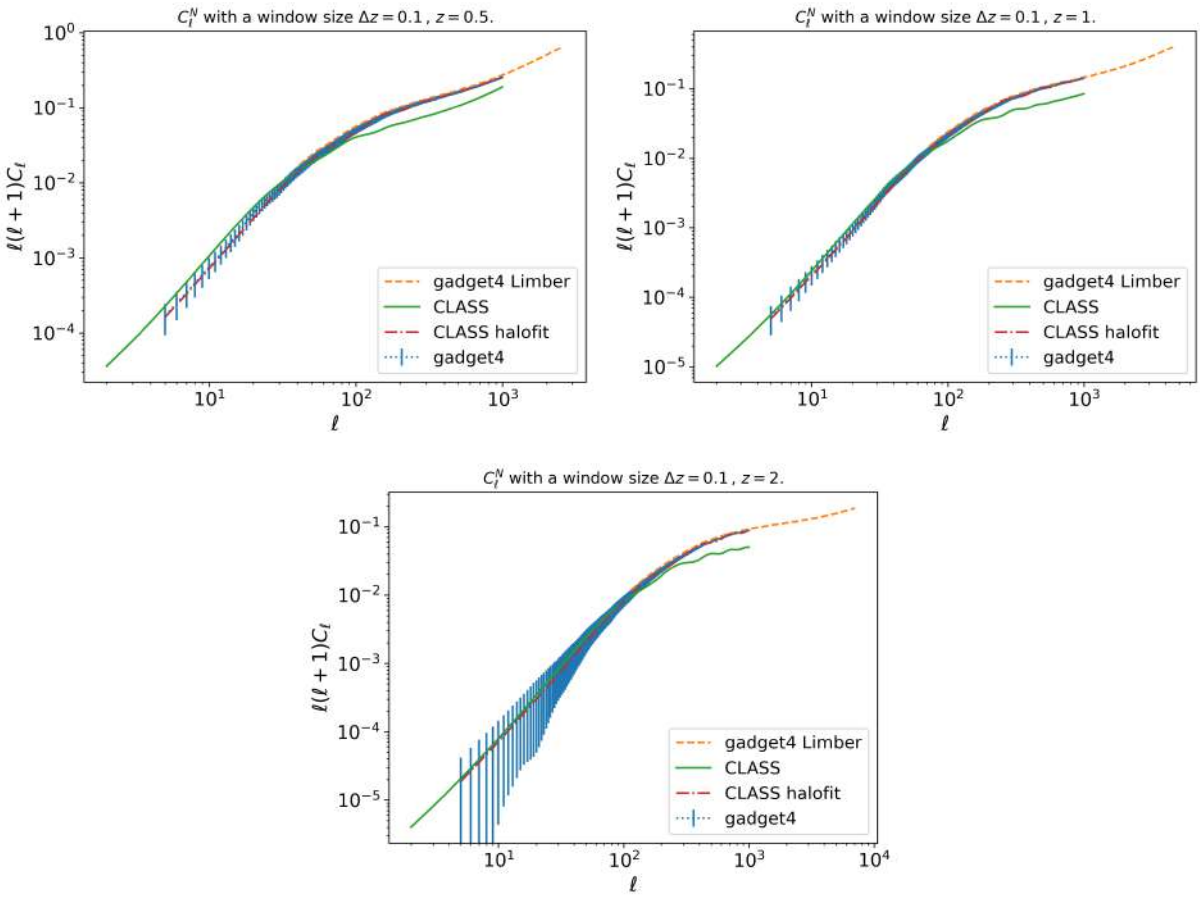

Figure D.2.: Angular power spectrum of matter for redshifts $z = 0.5\,, 1,\ 2$. The power spectra are calculated in three different ways: using the CLASS code linear and halofit routines, and using the `FFTlog` routine to obtain the angular spectra from the matter power spectrum. We also include the Limber approximation.

Bibliography

[1] A. R. Sandage. *Cosmology: A search for two numbers.* Physics Today **23** 34 (1970). URL: https://doi.org/10.1063/1.3021960 arXiv:https://pubs.aip.org/physicstoday/article-pdf/23/2/34/8272064/34_1_online.pdf. Cited on page 1.

[2] L. Amendola et al. *Cosmology and Fundamental Physics with the Euclid Satellite.* Living Reviews in Relativity **21** (2016). arXiv: 1606.00180 Publisher: Springer. URL: http://arxiv.org/abs/1606.00180. Cited on page 1.

[3] C. J. A. P. Martins et al. *Cosmology and fundamental physics with the ELT-ANDES spectrograph* 2024. URL: https://arxiv.org/abs/2311.16274 arXiv:2311.16274. Cited on pages 1, 2, 34, and 77.

[4] A. Weltman et al. *Fundamental physics with the Square Kilometre Array.* Publications of the Astronomical Society of Australia **37** (2020). URL: http://dx.doi.org/10.1017/pasa.2019.42. Cited on page 1.

[5] G. Agazie et al. *The NANOGrav 15 yr Data Set: Evidence for a Gravitational-wave Background.* The Astrophysical Journal Letters **951** L8 (2023). URL: http://dx.doi.org/10.3847/2041-8213/acdac6. Cited on page 1.

[6] A. Sandage. *The Change of Redshift and Apparent Luminosity.* The Astrophysical Journal **136** (1962). Cited on pages 1 and 31.

[7] G. C. McVittie. *Appendix to The Change of Redshift and Apparent Luminosity of Galaxies due to the Deceleration of Selected Expanding Universes.* Astrophysical Journal **136** 334 (1962). Cited on pages 1 and 31.

[8] A. Heinesen. *Multipole decomposition of the general luminosity distance Hubble law — a new framework for observational cosmology.* Journal of Cosmology and Astroparticle Physics **2021** 008 (2021). URL: http://dx.doi.org/10.1088/1475-7516/2021/05/008. Cited on pages 2, 43, 48, 49, and 50.

[9] A. Heinesen. *Redshift drift as a model independent probe of dark energy.* Physical Review D (2021). arXiv: 2102.03774. URL: http://arxiv.org/abs/2102.03774. Cited on pages 2, 32, 43, 50, and 77.

[10] P. **Bessa**, R. Durrer, and D. Stock. *Perturbations of cosmological redshift drift.* JCAP **11** 093 (2023). arXiv:2306.13911. Cited on pages 2, 34, 35, 36, 46, 54, and 77.

[11] P. **Bessa**, M. Campista, and A. Bernui. *Observational constraints on Starobinsky $f(R)$ cosmology from cosmic expansion and structure growth data.* Eur. Phys. J. C **82** 506 (2022). arXiv:2112.00822. Cited on page 2.

[12] P. **Bessa** and O. F. Piattella. *Gravitational lensing in a universe with matter and a cosmological constant*. Phys. Rev. D **106** 123513 (2022). arXiv:2209.04063. Cited on page 2.

[13] P. **Bessa**. *Strong gravitational lensing in Horndeski theory of gravity*. Phys. Rev. D **108** 024062 (2023). arXiv:2304.08141. Cited on page 2.

[14] P. **Bessa** and T. Ottoni. *Um Primeiro passo em direção à modificação da gravidade: Teorias Escalar-Tensoriais e f(R)*. Cadernos de Astronomia **3** 128 (2022). (in Portuguese). Cited on page 2.

[15] P. **Bessa**, V. Marra, and T. Castro. *Redshift Drift fluctuations from n-body simulations*. IN PREPARATION). Cited on pages 2, 68, and 77.

[16] H. Stephani, D. Kramer, M. MacCallum, C. Hoenselaers, and E. Herlt. *Cambridge monographs on mathematical physics: Exact solutions of Einstein's field equations*. Cambridge University Press Cambridge, England 2 edition 2003. Cited on page 3.

[17] J. N. Islam. *An introduction to mathematical cosmology*. Cambridge University Press Cambridge, England 1992. Cited on page 4.

[18] E. Hubble. *A relation between distance and radial velocity among extra-galactic nebulae*. Proceedings of the National Academy of Sciences **15** 168–173 (1929). URL: http://dx.doi.org/10.1073/pnas.15.3.168. Cited on page 6.

[19] J.-P. Luminet. *Editorial note to: Georges Lemaître, A homogeneous universe of constant mass and increasing radius accounting for the radial velocity of extra-galactic nebulae*. General Relativity and Gravitation **45** 1619–1633 (2013). URL: http://dx.doi.org/10.1007/s10714-013-1547-4. Cited on page 6.

[20] R. Durrer. *The Cosmic Microwave Background*. Cambridge University Press 2 edition 2020. Cited on pages 7, 9, 12, 13, 14, 16, 17, 18, 19, 20, 21, 22, 23, 24, 25, 26, 27, 29, 40, 41, 45, 54, 59, 70, 73, 74, 79, 80, and 82.

[21] R. A. Alpher, H. Bethe, and G. Gamow. *The Origin of Chemical Elements*. Phys. Rev. **73** 803 (1948). URL: https://link.aps.org/doi/10.1103/PhysRev.73.803. Cited on page 7.

[22] A. A. Penzias and R. W. Wilson. *A Measurement of Excess Antenna Temperature at 4080 Mc/s*. Astrophysical Journal **142** 419 (1965). Cited on page 7.

[23] R. H. Dicke, P. J. E. Peebles, P. G. Roll, and D. T. Wilkinson. *Cosmic Black-Body Radiation*. Astrophysical Journal **142** 414 (1965). Cited on page 8.

[24] S. Dodelson and F. Schmidt. *Modern Cosmology*. Elsevier 2021. Cited on pages 9, 10, 12, 17, 18, 24, 25, 27, 29, 36, 40, 41, 69, and 70.

[25] P. J. E. Peebles. *Large-scale background temperature and mass fluctuations due to scale-invariant primeval perturbations*. Astrophysical Journal letters **263** L1 (1982). Cited on page 9.

[26] S. Perlmutter et al. *Discovery of a Supernova Explosion at Half the Age of the Universe and its Cosmological Implications*. Nature **391** (1997). URL: https://www.osti.gov/biblio/974166. Cited on page 9.

[27] B. Chaboyer, P. Demarque, P. J. Kernan, and L. M. Krauss. *The Age of Globular Clusters in Light ofHipparcos: Resolving the Age Problem?* The Astrophysical Journal **494** 96–110 (1998). URL: http://dx.doi.org/10.1086/305201. Cited on page 9.

[28] A. G. Riess et al. *Observational Evidence from Supernovae for an Accelerating Universe and a Cosmological Constant.* The Astrophysical Journal **116** 1009 (1998). arXiv:astro-ph/9805201. Cited on pages 9 and 33.

[29] B. P. Schmidt et al. *The High-Z Supernova Search: Measuring Cosmic Deceleration and Global Curvature of the Universe Using Type Ia Supernovae.* The Astrophysical Journal **507** 46–63 (1998). URL: http://dx.doi.org/10.1086/306308. Cited on page 9.

[30] J. M. Stewart, M. Walker, and P. R. S. L. A. *Perturbations of space-times in general relativity.* Proceedings of the Royal Society of London. A. Mathematical and Physical Sciences **341** 49 (1974). Cited on page 11.

[31] G. F. R. Ellis and M. Bruni. *Covariant and gauge-invariant approach to cosmological density fluctuations.* Phys. Rev. D **40** 1804 (1989). URL: https://link.aps.org/doi/10.1103/PhysRevD.40.1804. Cited on pages 12 and 13.

[32] J. M. Stewart. *Perturbations of Friedmann-Robertson-Walker cosmological models.* Classical and Quantum Gravity **7** 1169–1180 (1990). URL: http://dx.doi.org/10.1088/0264-9381/7/7/013. Cited on page 12.

[33] R. Durrer. *Gauge Invariant Cosmological Perturbation Theory.* Proceedings of the 16th Workshop on General Relativity and Gravitation in Japan, JGRG 2006 (1993). arXiv: astro-ph/9311041. URL: http://arxiv.org/abs/astro-ph/9311041. Cited on pages 12, 13, and 16.

[34] Planck Collaboration. *Planck 2018 results. VI. Cosmological parameters.* aap **641** A6 (2020). arXiv:1807.06209. Cited on pages 13, 20, 21, 23, 24, 27, and 32.

[35] C.-P. Ma and E. Bertschinger. *Cosmological Perturbation Theory in the Synchronous and Conformal Newtonian Gauges.* The Astrophysical Journal **455** 7 (1995). URL: http://dx.doi.org/10.1086/176550. Cited on pages 15 and 16.

[36] *NIST Digital Library of Mathematical Functions.* https://dlmf.nist.gov/, Release 1.2.0 of 2024-03-15. F. W. J. Olver, A. B. Olde Daalhuis, D. W. Lozier, B. I. Schneider, R. F. Boisvert, C. W. Clark, B. R. Miller, B. V. Saunders, H. S. Cohl, and M. A. McClain, eds. URL: https://dlmf.nist.gov/. Cited on pages 17 and 80.

[37] C. Bonvin and R. Durrer. *What galaxy surveys really measure.* Physical Review D - Particles, Fields, Gravitation and Cosmology **84** (2011). arXiv: 1105.5280v3. URL: http://arxiv.org/abs/1105.5280. Cited on pages 19, 23, 27, 56, 62, and 70.

[38] R. K. Sachs and A. M. Wolfe. *Perturbations of a Cosmological Model and Angular Variations of the Microwave Background.* APJ **147** 73 (1967). Cited on pages 20 and 22.

[39] A. Lewis and A. Challinor. *CAMB: Code for Anisotropies in the Microwave Background.* Astrophysics Source Code Library, record ascl:1102.026 2011. Cited on page 20.

[40] J. Lesgourgues. *The Cosmic Linear Anisotropy Solving System (CLASS) I: Overview.* arXiv e-prints page arXiv:1104.2932 (2011). arXiv:1104.2932. Cited on pages 20, 23, and 53.

[41] E. Di Dio, F. Montanari, J. Lesgourgues, and R. Durrer. *The CLASSgal code for Relativistic Cosmological Large Scale Structure*. Journal of Cosmology and Astroparticle Physics **2013** 044 (2013). arXiv:1307.1459 [astro-ph]. URL: http://arxiv.org/abs/1307.1459. Cited on pages 20, 23, 58, 74, and 86.

[42] G. F. Smoot. *COBE observations and results*. In *Conference on 3K cosmology*. ASCE 1999. URL: http://dx.doi.org/10.1063/1.59326. Cited on page 22.

[43] P. Collaboration. *Planck2015 results: XXI. The integrated Sachs-Wolfe effect*. Astronomy &; Astrophysics **594** A21 (2016). URL: http://dx.doi.org/10.1051/0004-6361/201525831. Cited on pages 22 and 27.

[44] V. Mukhanov. *Physical Foundations of Cosmology*. Cambridge University Press 2005. URL: http://dx.doi.org/10.1017/CBO9780511790553. Cited on pages 22 and 23.

[45] D. J. Eisenstein and W. Hu. *Baryonic Features in the Matter Transfer Function*. ApJ **496** 605 (1998). arXiv:astro-ph/9709112. Cited on page 23.

[46] S. e. a. Alam. *Completed SDSS-IV extended Baryon Oscillation Spectroscopic Survey: Cosmological implications from two decades of spectroscopic surveys at the Apache Point Observatory*. Physical Review D **103** 083533 (2021). arXiv:2007.08991. Cited on page 27.

[47] A. e. a. Semenaite. *Cosmological implications of the full shape of anisotropic clustering measurements in BOSS and eBOSS*. MNRAS **512** 5657 (2022). arXiv:2111.03156. Cited on page 27.

[48] Planck Collaboration. *Planck2018 results: I. Overview and the cosmological legacy of Planck*. Astronomy & Astrophysics **641** A1 (2020). URL: http://dx.doi.org/10.1051/0004-6361/201833880. Cited on pages 27 and 28.

[49] A. Challinor and A. Lewis. *Linear power spectrum of observed source number counts*. Physical Review D **84** (2011). URL: http://dx.doi.org/10.1103/PhysRevD.84.043516. Cited on page 27.

[50] A. G. Riess and L. Breuval. *The Local Value of H_0* 2024. arXiv:2308.10954. Cited on pages 29, 33, and 34.

[51] E. e. a. Abdalla. *Cosmology intertwined: A review of the particle physics, astrophysics, and cosmology associated with the cosmological tensions and anomalies*. Journal of High Energy Astrophysics **34** 49 (2022). arXiv:2203.06142. Cited on pages 29 and 34.

[52] M. Douspis, L. Salvati, and N. Aghanim. *On the tension between Large Scale Structures and Cosmic Microwave Background* 2019. arXiv:1901.05289. Cited on page 29.

[53] E. Di Valentino, O. Mena, S. Pan, L. Visinelli, W. Yang, A. Melchiorri, D. F. Mota, A. G. Riess, and J. Silk. *In the realm of the Hubble tension—a review of solutions*. Classical and Quantum Gravity **38** 153001 (2021). URL: http://dx.doi.org/10.1088/1361-6382/ac086d. Cited on pages 29 and 34.

[54] S. Weinberg. *The Cosmological Constant Problems (Talk given at Dark Matter 2000, February, 2000)* 2000. arXiv:astro-ph/0005265. Cited on page 29.

[55] S. Weinberg. *The Cosmological Constant Problem*. Rev. Mod. Phys. **61** 1 (1989). Cited on page 30.

[56] S. Schander and T. Thiemann. *Backreaction in Cosmology*. Frontiers in Astronomy and Space Sciences **8** (2021). URL: http://dx.doi.org/10.3389/fspas.2021.692198. Cited on page 30.

[57] P. Kumar Aluri, P. Cea, P. Chingangbam, M.-C. Chu, R. G. Clowes, D. Hutsemékers, J. P. Kochappan, A. M. Lopez, L. Liu, N. C. M. Martens, C. J. A. P. Martins, K. Migkas, E. Ó Colgáin, P. Pranav, L. Shamir, A. K. Singal, M. M. Sheikh-Jabbari, J. Wagner, S.-J. Wang, D. L. Wiltshire, S. Yeung, L. Yin, and W. Zhao. *Is the observable Universe consistent with the cosmological principle?* Classical and Quantum Gravity **40** 094001 (2023). URL: http://dx.doi.org/10.1088/1361-6382/acbefc. Cited on page 30.

[58] T. Clifton, P. G. Ferreira, A. Padilla, and C. Skordis. *Modified gravity and cosmology*. Physics Reports **513** 1–189 (2012). URL: http://dx.doi.org/10.1016/j.physrep.2012.01.001. Cited on pages 30 and 42.

[59] C. Martins, S. Cristiani, G. Cupani, V. D'Odorico, R. G. Santos, A. Leite, C. Marques, D. Milaković, P. Molaro, M. T. Murphy, N. Nunes, T. M. Schmidt, V. Adibekyan, Y. Alibert, P. Di Marcantonio, J. G. Hernández, D. Mégevand, E. Palle, F. Pepe, N. Santos, S. Sousa, A. Sozzetti, A. S. Mascareño, and M. Z. Osorio. *Fundamental physics with ESPRESSO: Constraints on Bekenstein and dark energy models from astrophysical and local probes*. Physical Review D **105** (2022). URL: http://dx.doi.org/10.1103/PhysRevD.105.123507. Cited on pages 30, 37, 39, 41, and 42.

[60] R. L. et al. *Euclid Definition Study Report* 2011. arXiv:1110.3193. Cited on page 30.

[61] A. Loeb. *Direct Measurement of Cosmological Parameters from the Cosmic Deceleration of Extragalactic Objects*. The Astrophysical Journal **499** L111 (1998). arXiv: astro-ph/9802122. Cited on pages 31, 34, 35, 36, 53, and 78.

[62] M. Visser. *Cosmography: Cosmology without the Einstein equations*. General Relativity and Gravitation **37** 1541–1548 (2005). URL: http://dx.doi.org/10.1007/s10714-005-0134-8. Cited on page 32.

[63] A. R. Neben and M. S. Turner. *BEYONDH0ANDq0: COSMOLOGY IS NO LONGER JUST TWO NUMBERS*. The Astrophysical Journal **769** 133 (2013). URL: http://dx.doi.org/10.1088/0004-637X/769/2/133. Cited on page 33.

[64] K. Lake. *Comment on the time evolution of the cosmological redshift*. The Astrophysical Journal **247** 17 (1981). Cited on page 34.

[65] C. M. J. Marques, C. J. A. P. Martins, and B. G. López. *Watching the Universe's acceleration era with the SKAO*. Mon. Not. Roy. Astron. Soc. **527** 9918 (2023). arXiv:2312.09702. Cited on pages 34, 37, 39, 40, 41, and 64.

[66] J. Esteves, C. J. A. P. Martins, B. G. Pereira, and C. S. Alves. *Cosmological impact of redshift drift measurements*. MNRAS **000** 1 (2021). arXiv: 2108.10739v1. Cited on pages 34, 37, and 40.

[67] K. Bolejko, C. Wang, and G. F. Lewis. *Direct detection of the cosmic expansion: the redshift drift and the flux drift.* 2019). arXiv: 1907.04495. URL: http://arxiv.org/abs/1907.04495. Cited on pages 34 and 37.

[68] J. Liske, A. Grazian, E. Vanzella, M. Dessauges, M. Viel, L. Pasquini, M. Haehnelt, S. Cristiani, F. Pepe, G. Avila, P. Bonifacio, F. Bouchy, H. Dekker, B. Delabre, S. D'Odorico, V. D'Odorico, S. Levshakov, C. Lovis, M. Mayor, P. Molaro, L. Moscardini, M. T. Murphy, D. Queloz, P. Shaver, S. Udry, T. Wiklind, and S. Zucker. *Cosmic dynamics in the era of Extremely Large Telescopes.* Monthly Notices of the Royal Astronomical Society **386** 1192 (2008). arXiv: 0802.1532. Cited on pages 34, 35, 36, 37, 38, 53, 60, 62, 64, and 65.

[69] V. Junkkarinen, R. D. Cohen, T. A. Barlow, and F. Hamann. *HST UV and Keck HIRES Spectra of BAL Quasars* 2001. arXiv:astro-ph/0106546. Cited on page 35.

[70] V. Springel. *The cosmological simulation code gadget-2.* Monthly Notices of the Royal Astronomical Society **364** 1105–1134 (2005). URL: http://dx.doi.org/10.1111/j.1365-2966.2005.09655.x. Cited on page 36.

[71] C. Dong, A. Gonzalez, S. Eikenberry, S. Jeram, M. Likamonsavad, J. Liske, D. Stelter, and A. Townsend. *Forecasting cosmic acceleration measurements using the Lyman-α forest.* Monthly Notices of the Royal Astronomical Society **514** 5493 (2022). URL: https://doi.org/10.1093/mnras/stac1702. Cited on pages 37 and 40.

[72] M. Martinelli, S. Pandolfi, C. J. A. P. Martins, and P. E. Vielzeuf. *Probing dark energy with redshift drift.* Physical Review D **86** (2012). URL: http://dx.doi.org/10.1103/PhysRevD.86.123001. Cited on page 37.

[73] C. M. J. Marques, C. J. a. P. Martins, and C. S. Alves. *Fundamental cosmology from ANDES precision spectroscopy* 2023. URL: https://arxiv.org/abs/2305.01446v1. Cited on pages 37, 40, 41, 43, 64, and 77.

[74] S. Cristiani, K. Boutsia, G. Calderone, G. Cupani, V. D'Odorico, F. Fontanot, A. Grazian, F. Guarneri, C. Martins, L. Pasquini, M. Porru, and E. Vanzella. *Spectrographs and Spectroscopists for the Sandage Test* 2023. arXiv:2302.04365 [astro-ph]. URL: http://arxiv.org/abs/2302.04365. Cited on pages 37, 42, and 65.

[75] R. Cooke. *The ACCELERATION programme: I. Cosmology with the redshift drift* 2019. URL: https://arxiv.org/abs/1912.04983v1. Cited on pages 37, 40, 42, 60, 61, 65, and 66.

[76] S. Chakrabarti, A. H. Gonzalez, S. Eikenberry, D. Erskine, M. Ishak, A. Kim, E. Linder, A. Nomerotski, M. Pierce, A. Slosar, P. Stankus, and Y.-D. Tsai. *Snowmass2021-White Paper Real-time Cosmology with High Precision Spectroscopy and Astrometry (CF1) Dark Matter: Particle Like (CF2) Dark Matter: Wavelike (CF3) Dark Matter: Cosmic Probes (CF4) Dark Energy and Cosmic Acceleration: The Modern Universe (CF5) Dark Energy and Cosmic Acceleration: Cosmic Dawn and Before (CF6) Dark Energy and Cosmic Acceleration: Complementarity of Probes and New Facilities (CF7) Cosmic Probes of Fundamental Physics (Other) [Please specify frontier/topical group].* 2022). arXiv: 2203.05924v1. URL: https://arxiv.org/abs/2203.05924. Cited on page 37.

[77] H.-R. Yu, T.-J. Zhang, and U.-L. Pen. *Method for Direct Measurement of Cosmic Acceleration by 21-cm Absorption Systems.* Physical Review Letters **113** (2014). URL: http://dx.doi.org/10.1103/PhysRevLett.113.041303. Cited on pages 37 and 40.

[78] F. Combes. *Science with SKA* 2021. arXiv:2107.03915. Cited on pages 37 and 39.

[79] R. Braun, T. Bourke, J. A. Green, E. Keane, and J. Wagg. *Advancing Astrophysics with the Square Kilometre Array.* In *Advancing Astrophysics with the Square Kilometre Array (AASKA14)* page 174 2015. Cited on pages 37 and 39.

[80] H. R. Klöckner, D. Obreschkow, C. Martins, A. Raccanelli, D. Champion, A. Roy, A. Lobanov, J. Wagner, and R. Keller. *Real time cosmology - A direct measure of the expansion rate of the Universe* 2015. arXiv:1501.03822. Cited on pages 39, 40, 65, and 73.

[81] C. S. Alves, A. C. O. Leite, C. J. A. P. Martins, J. G. B. Matos, and T. A. Silva. *Forecasts of redshift drift constraints on cosmological parameters.* MNRAS **488** 3607 (2019). URL: https://academic.oup.com/mnras/article/488/3/3607/5531778. Cited on pages 40, 41, and 42.

[82] A. G. Kim, E. V. Linder, J. Edelstein, and D. Erskine. *Giving cosmic redshift drift a whirl.* Astroparticle Physics **62** 195 (2015). arXiv: 1402.6614 Publisher: Elsevier. Cited on pages 40, 42, 53, 57, 60, 61, 62, 63, and 78.

[83] J. Darling. *Toward a Direct Measurement of the Cosmic Acceleration.* Astrophysical Jornal Letters **761** L26 (2012). arXiv:1211.4585. Cited on page 40.

[84] E. V. Linder. *Exploring the Expansion History of the Universe.* Physical Review Letters **90** (2003). URL: http://dx.doi.org/10.1103/PhysRevLett.90.091301. Cited on page 40.

[85] R. J. Scherrer. *Mapping the Chevallier-Polarski-Linder parametrization onto physical dark energy Models.* Physical Review D **92** (2015). URL: http://dx.doi.org/10.1103/PhysRevD.92.043001. Cited on page 40.

[86] T. Buchert et al. *Is there proof that backreaction of inhomogeneities is irrelevant in cosmology?* Class. Quant. Grav. **32** 215021 (2015). arXiv:1505.07800. Cited on page 42.

[87] W. Valkenburg, V. Marra, and C. Clarkson. *Testing the Copernican principle by constraining spatial homogeneity.* Mon. Not. Roy. Astron. Soc. **438** L6 (2014). arXiv:1209.4078. Cited on page 42.

[88] K. Bolejko and M. Korzyński. *Inhomogeneous cosmology and backreaction: Current status and future prospects.* International Journal of Modern Physics D **26** 1730011 (2017). URL: http://dx.doi.org/10.1142/S0218271817300117. Cited on page 42.

[89] J.-P. Uzan, C. Clarkson, and G. F. R. Ellis. *Time Drift of Cosmological Redshifts as a Test of the Copernican Principle.* Phys. Rev. Lett. **100** 191303 (2008). URL: https://link.aps.org/doi/10.1103/PhysRevLett.100.191303. Cited on page 42.

[90] R. Codur and C. Marinoni. *Redshift drift in radially inhomogeneous Lemaître-Tolman-Bondi spacetimes.* Phys. Rev. D **104** 123531 (2021). arXiv:2107.04868. Cited on page 42.

[91] S. M. Koksbang and A. Heinesen. *Redshift drift in a universe with structure: Lemaître-Tolman-Bondi structures with arbitrary angle of entry of light.* Phys. Rev. D **106** 043501 (2022). arXiv:2205.11907. Cited on pages 42, 43, 49, 50, 51, 67, 75, and 78.

[92] S. M. Koksbang. *Searching for Signals of Inhomogeneity Using Multiple Probes of the Cosmic Expansion Rate $H(z)$*. Phys. Rev. Lett. **126** 231101 (2021). URL: https://link.aps.org/doi/10.1103/PhysRevLett.126.231101. Cited on page 42.

[93] O. H. Marcori, C. Pitrou, J.-P. Uzan, and T. S. Pereira. *Direction and redshift drifts for general observers and their applications in cosmology*. Physical Review D **98** (2018). URL: http://dx.doi.org/10.1103/PhysRevD.98.023517. Cited on pages 43, 53, 57, 60, and 64.

[94] J.-P. Uzan, F. Bernardeau, and Y. Mellier. *Time drift of cosmological redshifts and its variance*. Physical Review D **77** (2008). URL: http://dx.doi.org/10.1103/PhysRevD.77.021301. Cited on pages 43, 53, and 57.

[95] A. Heinesen. *Redshift drift cosmography for model-independent cosmological inference*. Phys. Rev. D **104** 123527 (2021). arXiv:2107.08674. Cited on pages 43, 49, and 77.

[96] A. Heinesen. *Multipole decomposition of redshift drift – model independent mapping of the expansion history of the Universe*. Physical Review D (2020). arXiv: 2011.10048. URL: http://arxiv.org/abs/2011.10048. Cited on pages 44, 46, 47, 48, 49, and 77.

[97] M. Korzyński and J. Kopiński. *Optical drift effects in general relativity*. Journal of Cosmology and Astroparticle Physics **2018** 012 (2018). URL: http://dx.doi.org/10.1088/1475-7516/2018/03/012. Cited on pages 44 and 45.

[98] S. W. Hawking and G. Ellis. *The large scale structure of space-time*. Cambridge monographs on mathematical physics. Cambridge University Press Cambridge, England 1973. Cited on pages 44 and 50.

[99] V. Perlick. *Gravitational Lensing from a Spacetime Perspective*. Living Reviews in Relativity **7** (2004). URL: http://dx.doi.org/10.12942/lrr-2004-9. Cited on page 44.

[100] S. M. Koksbang. *Redshift drift in a universe with structure. II. Light rays propagated through a Newtonian n-body simulation*. Physical Review D **107** (2023). URL: http://dx.doi.org/10.1103/PhysRevD.107.063544. Cited on pages 49, 51, 60, 67, 73, 74, and 78.

[101] S. M. Koksbang. *Another look at redshift drift and the backreaction conjecture*. JCAP **10** 036 (2019). arXiv:1909.13489. Cited on pages 50 and 77.

[102] S. M. Koksbang. *Observations in statistically homogeneous, locally inhomogeneous cosmological toy models without FLRW backgrounds*. Monthly Notices of the Royal Astronomical Society: Letters **498** L135 (2020). URL: https://doi.org/10.1093/mnrasl/slaa146 arXiv:https://academic.oup.com/mnrasl/article-pdf/498/1/L135/56984194/mnrasl_498_1_l135.pdf. Cited on pages 50 and 52.

[103] T. Inoue, E. Komatsu, W. Aoki, T. Chiba, T. Misawa, and T. Usuda. *The effect of our local motion on the Sandage–Loeb test of the cosmic expansion*. Publ. Astron. Soc. Jap. **72** 131 (2020). arXiv:1911.01467. Cited on page 55.

[104] D. Blas, J. Lesgourgues, and T. Tram. *The Cosmic Linear Anisotropy Solving System (CLASS). Part II: Approximation schemes*. Journal of Cosmology and Astroparticle Physics **2011** 034 (2011). URL: https://doi.org/10.1088%2F1475-7516%2F2011%2F07%2F034. Cited on page 58.

[105] D. J. Eisenstein and W. Hu. *Baryonic Features in the Matter Transfer Function*. The Astrophysical Journal **496** 605 (1998). URL: https://doi.org/10.1086%2F305424. Cited on page 58.

[106] J. B. Orjuela-Quintana, S. Nesseris, and W. Cardona. *Using machine learning to compress the matter transfer function $T(k)$*. Physical Review D **107** (2023). URL: https://doi.org/10.1103%2Fphysrevd.107.083520. Cited on page 58.

[107] A. J. Nishizawa. *The integrated Sachs-Wolfe effect and the Rees-Sciama effect*. Progress of Theoretical and Experimental Physics **2014** 6B110 (2014). URL: https://doi.org/10.1093%2Fptep%2Fptu062. Cited on page 63.

[108] C. Quercellini, L. Amendola, A. Balbi, P. Cabella, and M. Quartin. *Real-time Cosmology*. Physics Reports **521** 95 (2010). arXiv: 1011.2646. URL: http://arxiv.org/abs/1011.2646. Cited on page 65.

[109] S. M. Koksbang, A. Heinesen, and H. J. Macpherson. *Redshift drift in a universe with structure III: Numerical relativity* 2024. URL: https://arxiv.org/abs/2404.06242 arXiv:2404.06242. Cited on pages 67, 74, 75, and 78.

[110] B. A. R. Rocha and C. J. A. P. Martins. *Redshift drift cosmography with ELT and SKAO measurements*. Monthly Notices of the Royal Astronomical Society **518** 2853–2869 (2022). URL: http://dx.doi.org/10.1093/mnras/stac3240. Cited on page 67.

[111] V. Springel, R. Pakmor, O. Zier, and M. Reinecke. *Simulating cosmic structure formation with the gadget-4 code*. Mon. Not. Roy. Astron. Soc. **506** 2871 (2021). arXiv:2010.03567. Cited on page 67.

[112] S. R. Green and R. M. Wald. *Newtonian and Relativistic Cosmologies*. Phys. Rev. D **85** 063512 (2012). arXiv:1111.2997. Cited on page 68.

[113] X. Fang, E. Krause, T. Eifler, and N. MacCrann. *Beyond Limber: efficient computation of angular power spectra for galaxy clustering and weak lensing*. Journal of Cosmology and Astroparticle Physics **2020** 010–010 (2020). URL: http://dx.doi.org/10.1088/1475-7516/2020/05/010. Cited on pages 70 and 72.

[114] F. Villaescusa-Navarro. *Pylians: Python libraries for the analysis of numerical simulations*. Astrophysics Source Code Library, record ascl:1811.008 2018. arXiv:1811.008. Cited on page 70.

[115] W. L. Matthewson and R. Durrer. *The Flat Sky Approximation to Galaxy Number Counts*. JCAP **02** 027 (2021). arXiv:2006.13525. Cited on pages 72 and 86.

[116] J. D. Cohn. *Power spectrum and correlation function errors: Poisson vs. Gaussian shot noise*. New Astron. **11** 226 (2006). arXiv:astro-ph/0503285. Cited on page 73.

[117] V. Marra, T. Castro, D. Camarena, S. Borgani, and A. Ragagnin. *The BEHOMO project: Λ Lemaître-Tolman-Bondi N-body simulations*. Astronomy &; Astrophysics **664** A179 (2022). URL: http://dx.doi.org/10.1051/0004-6361/202243539. Cited on page 78.

[118] O. F. Piattella and L. Giani. *Redshift drift of gravitational lensing*. Physical Review D **95** (2017). URL: http://dx.doi.org/10.1103/PhysRevD.95.101301. Cited on page 78.

[119] C. Wang, K. Bolejko, and G. F. Lewis. *The Redshift Difference in Gravitational Lensed Systems: A Novel Probe of Cosmology* 2023. URL: https://arxiv.org/abs/2308.07529 arXiv:2308.07529. Cited on page 78.

[120] C. Wang, K. Bolejko, and G. F. Lewis. *The Instantaneous Redshift Difference of Gravitationally Lensed Images: Theory and Observational Prospects*. The Astrophysical Journal **940** 16 (2022). URL: http://dx.doi.org/10.3847/1538-4357/ac98aa. Cited on page 78.

[121] B. R. James. *Probabilidade: Um curso em nível intermediário*. IMPA Rio de Janeiro, Brasil 5 edition 2023. Cited on pages 80 and 81.

[122] E. Butkov. *Mathematical Physics*. Pearson Upper Saddle River, NJ 1968. Cited on page 80.

[123] M. LoVerde and N. Afshordi. *Extended Limber Approximation*. Phys. Rev. D **78** 123506 (2008). arXiv:0809.5112. Cited on page 86.